NORTH ATLANTIC TREATY ORGANIZATION

SCIENCE AND TECHNOLOGY ORGANIZATION

AC/323(SET-207)TP/863

www.sto.nato.int

STO TECHNICAL REPORT **TR-SET-207**

Advanced Situation-Specific Modeling, Sensing and Vulnerability Mitigation Using Passive Radar Technology

(Atténuation de la vulnérabilité, modélisation et détection sophistiquées propres à une situation particulière, utilisant la technologie du radar passif)

Final Report of NATO SET-207.

Published March 2019

NORTH ATLANTIC TREATY ORGANIZATION

SCIENCE AND TECHNOLOGY ORGANIZATION

AC/323(SET-207)TP/863

www.sto.nato.int

STO TECHNICAL REPORT **TR-SET-207**

Advanced Situation-Specific Modeling, Sensing and Vulnerability Mitigation Using Passive Radar Technology

(Atténuation de la vulnérabilité, modélisation et détection sophistiquées propres à une situation particulière, utilisant la technologie du radar passif)

Final Report of NATO SET-207.

The NATO Science and Technology Organization

Science & Technology (S&T) in the NATO context is defined as the selective and rigorous generation and application of state-of-the-art, validated knowledge for defence and security purposes. S&T activities embrace scientific research, technology development, transition, application and field-testing, experimentation and a range of related scientific activities that include systems engineering, operational research and analysis, synthesis, integration and validation of knowledge derived through the scientific method.

In NATO, S&T is addressed using different business models, namely a collaborative business model where NATO provides a forum where NATO Nations and partner Nations elect to use their national resources to define, conduct and promote cooperative research and information exchange, and secondly an in-house delivery business model where S&T activities are conducted in a NATO dedicated executive body, having its own personnel, capabilities and infrastructure.

The mission of the NATO Science & Technology Organization (STO) is to help position the Nations' and NATO's S&T investments as a strategic enabler of the knowledge and technology advantage for the defence and security posture of NATO Nations and partner Nations, by conducting and promoting S&T activities that augment and leverage the capabilities and programmes of the Alliance, of the NATO Nations and the partner Nations, in support of NATO's objectives, and contributing to NATO's ability to enable and influence security and defence related capability development and threat mitigation in NATO Nations and partner Nations, in accordance with NATO policies.

The total spectrum of this collaborative effort is addressed by six Technical Panels who manage a wide range of scientific research activities, a Group specialising in modelling and simulation, plus a Committee dedicated to supporting the information management needs of the organization.

- AVT Applied Vehicle Technology Panel
- HFM Human Factors and Medicine Panel
- IST Information Systems Technology Panel
- NMSG NATO Modelling and Simulation Group
- SAS System Analysis and Studies Panel
- SCI Systems Concepts and Integration Panel
- SET Sensors and Electronics Technology Panel

These Panels and Group are the power-house of the collaborative model and are made up of national representatives as well as recognised world-class scientists, engineers and information specialists. In addition to providing critical technical oversight, they also provide a communication link to military users and other NATO bodies.

The scientific and technological work is carried out by Technical Teams, created under one or more of these eight bodies, for specific research activities which have a defined duration. These research activities can take a variety of forms, including Task Groups, Workshops, Symposia, Specialists' Meetings, Lecture Series and Technical Courses.

The content of this publication has been reproduced directly from material supplied by STO or the authors.

Published March 2019

ISBN 978-92-837-2187-1

Table of Contents

List of Figures

List of Tables

List of Acronyms

ADC	Analogue to Digital Converter
ADS	Automatic Dependent Surveillance
AIS	Automatic Identification System
APM	Advanced Propagation Model
ATM	Air Traffic Management
BEM	Bistatic Equivalent Monostatic
BSAR	Bistatic Synthetic Aperture Radar
CAF	Cross Ambiguity Function
CFAR	Constant False Alarm Rate
CLT	Central Limit Theorem
DAB	Digital Audio Broadcast
DOA	Direction Of Arrival
DPI	Direct Path Interference
DSI	Direct Signal Interference (DSI and DPI are used interchangeably)
DTED	Digital Terrain Elevation Data
DVB-T	Digitial Video Broadcast-Terrestrial
ERP	Effective Radiated Power
FM	Frequency Modulation
GPS	Global Positioning System
HPBW	Half Power Beam Width
IoO	Illuminator of Opportunity
IRF	Impulse Response Function
ITU	International Telephone Union
LNA	Low Noise Amplifier
LOS	Line Of Sight
MPT	Mission Planning Tool
MSA	Maritime Situational Awareness
PaRaDe	Passive Radar Demonstrator
PBR	Passive Bistatic Radar
PSD	Power Spectral Density
PSLR	Peak-to-Side Lobe Ratio
PSR	Primary Surveillance Radar
RCS	Radar Cross Section
RF	Radio Frequency
RMSE	Root Mean Square Error
SDR	Software Defined Radio
SGP	Simplified General Perturbation
SSR	Secondary Surveillance Radar

UCL	University College London
UCT	University of Cape Town
UHF	Ultra High Frequency (NATO B and C bands)
ULA	Uniform Linear Array
VHF	Very High Frequency (NATO A-band)
WAM	Wide-Area Multilateration
WUT	Warsaw University of Technology

Terms of Reference

I. BACKGROUND AND JUSTIFICATION (RELEVANCE TO NATO)

SET-108 demonstrated the relevance and extent of understanding of passive sensors for air surveillance applications. SET-164 has made a valuable contribution to addressing the critical unknown of bistatic clutter and has demonstrated the capability of passive radar in Maritime Situational Awareness (MSA) roles. The work of SET-164 has, however, shown the limitations of existing land-clutter models and indicated that VHF bistatic radar performance is strongly dependent on the propagation over the surface, to the extent that further study will be needed to find models which are suitable for general modelling of passive radars.

The objective of this new SET is to extend the valuable lessons learned from SET-164 by developing and validating a robust and inclusive model for passive radar. A robust model-based approach to radar design and procurement is in accord with the approach desired by the more sophisticated military sensor research and planning agencies. The proposed model will consist of: a comprehensive prediction of propagation effects and a characterisation of bistatic clutter, (both of which SET-164 has shown require more development), target modelling, characterisation of RFI, and development of agile mitigation techniques for clutter and interference.

One benefit of bistatic radars, particularly at VHF/UHF, is their ability to use forward-scatter techniques to detect low observable targets. As the forward-scatter behaviour is only achieved over a limited set of directions, networking between multiple transmitter/receiver pairs is required to obtain complete coverage. For systems using omni-directional (broadcast) transmitters the poor angular accuracy which is obtainable from low-cost receivers means that practical systems will have to use multilateration, again between multiple transmitter/receiver pairs, to obtain adequate positional accuracy. Both of these considerations mean that the radar deployment will have to consist of a collection of sensors. The topic of passive radar sensor integration needs to be studied, adhering to the aforementioned methods, to accurately determine sensor performance and to enhance siting for strategic advantage in a net-centric domain. The group will research a robust infrastructure of sensors, which as well as exploiting spatial diversity and improving resolution will also yield greater detection ranges and exploit frequency and temporal diversity over what is obtainable by an individual sensor. Aspects of Dynamic Spectrum Access (DSA) and system covertness for network resilience will have to be researched to ensure the survivability and efficient operation of the network, even if individual nodes have been destroyed.

Countries are increasingly investing resources into border surveillance. UHF/VHF radar, due to its operating frequency has foliage penetration capabilities and would potentially make a viable border surveillance sensor, which could also complement battle-field surveillance radar. However, it would probably not be possible to obtain a transmission license for an active radar at these frequencies, so a Passive Bistatic Radar (PBR) would be the only way of exploiting such a capability. Since border surveillance radars typically recognise people by their Doppler signatures, this aspect will have to be studied. The effects of motion-induced interference on radar performance will also have to be mitigated for solutions that require the PBR receiver to be mounted on moving/ unstable platforms. There is also increased interest in the use of satellite illuminators for border and perimeter surveillance, and for Maritime Situational Awareness. The clear benefit to NATO is an increased expertise in border surveillance and control and MSA, and an in-depth feasibility study of the suitability of passive radar for these, and similar, applications.

II. OBJECTIVE(S)

The objective of this SET is to extend the valuable lessons learned from SET-164. To achieve this, we aim to develop and validate a robust and inclusive model for passive radar. A robust model-based approach to sensor specification is in accord with the aspirations of advanced military sensor research and planning agencies. Sensor networking will be investigated. The role of passive radar for border surveillance and MSA applications will also be investigated. Motion compensation and alternative illuminating sources will be analysed. The activity supports national and NATO acquisition programmes and further provides analysis in support of long-term R&D requirements planning.

III. RESOURCES

a) Membership:

- **Recommended lead nation:** NATO C3 Agency (Dr. Paul E. Howland).
- **Skills required:** one or more of: expertise in radar systems, statistical modelling, emerging sensor, platform and communications technologies, future operational requirements.

b) National and/or NATO resources needed:

- Resources to support attendance at three one-week meetings per year, for three years.
- Resources to support data and system analysis outside of meetings (recommendation of at least 3 months per year).

c) Bistatic VHF/UHF radar data collection capabilities (by at least one nation) and willingness to release I/Q level data to the group.

SET-207 Membership List

CHAIR

Dr. Daniel O'HAGAN
Fraunhofer FHR
GERMANY
Email: daniel.ohagan@fhr.fraunhofer.de

MEMBERS

Maj. Emre AYDEMIR
Turkish Air Force Command
TURKEY
Email: M.AYDEMIR@HHO.EDU.TR

Mr. William Chauncey BAROTT
Embry–Riddle Aeronautical University
UNITED STATES
Email: barottw@erau.edu

Dr. Alan D. BERNARD
MIT Lincoln Laboratory
UNITED STATES
Email: bernard@ll.mit.edu

Dr. Amerigo CAPRIA
CNIT (National Interuniversity Consortium for Telecommunications)
ITALY
Email: amerigo.capria@cnit.it

Mr. Per-Olov FROLIND
FOI Swedish Defence Agency
SWEDEN
Email: per-olov.frolind@foi.se

Dr. Maria Sabrina GRECO
University of Pisa
ITALY
Email: m.greco@iet.unipi.it

Prof. Hugh GRIFFITHS
University College London
UNITED KINGDOM
Email: h.griffiths@ee.ucl.ac.uk

Mr. Ari J. JOKI
Air Surveillance Systems, Joint Systems Centre
FINLAND
Email: ari.joki@mil.fi

Capt. Virginie KUBICA
Royal Military Academy
BELGIUM
Email: vkubica@elec.rma.ac.be

Dr. Mateusz Piotr MALANOWSKI
Warsaw University of Technology
POLAND
Email: m.malanowski@elka.pw.edu.pl

Prof. Dr. Ir. Xavier NEYT
Royal Military Academy
BELGIUM
Email: Xavier.Neyt@rma.ac.be

Dr. James PALMER
DSTO
AUSTRALIA
Email: James.Palmer@dsto.defence.gov.au

Dr. Radek PLSEK
ERA a.s.
CZECH REPUBLIC
Email: r.plsek@era.aero

LtCol. Jacques RAOUT
EMAA/BCEROG
FRANCE
Email: jacques.raout@air.defense.gouv.fr

Dr. Christof SCHÜPBACH
Federal Department of Defence
SWITZERLAND
Email: Christof.Schuepbach@armasuisse.ch
Dr. Clayton STEWART
University College London
UNITED KINDGOM
Email: c.stewart@ee.ucl.ac.uk

Dr. Pietro STINCO
University of Pisa
ITALY
Email: pietro.stinco@for.unipi.it

Mr. Martin UMMENHOFER
Fraunhofer FHR
GERMANY
Email: martin.ummenhofer@fhr.fraunhofer.de

Dr. Andrew Gerald STOVE
University of Birmingham
UNITED KINGDOM
Email: andystove@compuserve.com

Dr. Pascal Cornelius ZIEGLER
RUAG
SWITZERLAND
Email: pascal.ziegler@ruag.com

PANEL/GROUP MENTOR

Prof. Dr. Joachim H.G. ENDER
Fraunhofer FHR
GERMANY
Email: joachim.ender@fhr.fraunhofer.de

Advanced Situation-Specific Modeling, Sensing and Vulnerability Mitigation Using Passive Radar Technology

(STO-TR-SET-207)

Executive Summary

The objective of SET-207 was to extend the valuable lessons learned from SET-164 by developing and validating a robust and inclusive model for passive radar. A robust model-based approach to radar design and procurement is in accord with the approach desired by the more sophisticated military sensor research and planning agencies.

In particular, SET-207 undertook three propagation measurement campaigns. One trial was performed in Florida, USA, the second in Switzerland and the third in South Africa. The three trial regions were significantly different in topology and climate and the analysis and associated models contribute greater insight into passive radar performance. The individual studies focus on propagation effects in VHF and UHF as a function of multipath and climatic conditions.

Several conclusions can be drawn from the measurements and models that appear in this report:

- FM based Passive Radar receivers that are positioned close to the ground (elevated less than 10 meters) and reasonably far from the reference transmitter (baseline longer than 20 km) will most likely be within the first multipath null and will suffer from multipath losses.
- The depth of the multipath null depends (amongst other factors) on the electromagnetic properties of the reflecting surface. Changes in conductivity and permittivity due to changing soil conditions can have significant effects on the reflection coefficient.

Freely available terrain data is not accurate enough to predict bistatic low grazing angle multipath losses to an acceptable degree of confidence.

Chapter 2 will show that there is no conclusive evidence that precipitation or other weather phenemona have a significant effect on the received power.

In Chapter 3 the characteristics of tropospheric radio propagation were studied given its importance to passive radar. Errors in its prediction will ultimately affect the anticipated detection statistics of the radar, which could have consequences on network planning and overall performance. Similarly, variations in the link losses will cause SINR variations, through the influence on the direct path, interferer, echo, and clutter signals. This work has explored methods of both modelling and measuring these effects.

Atténuation de la vulnérabilité, modélisation et détection sophistiquées propres à une situation particulière, utilisant la technologie du radar passif

(STO-TR-SET-207)

Synthèse

L'objectif du SET-207 était de prolonger les précieux enseignements du SET-164 en développant et en validant un modèle robuste et inclusif de radar passif. Une approche de conception et d'achat des radars robuste et basée sur un modèle est en accord avec l'approche souhaitée par les agences de recherche et de planification des capteurs militaires plus sophistiqués.

Le SET-207 a notamment entrepris trois campagnes de mesure de la propagation. Un essai a été réalisé en Floride, aux Etats-Unis, un autre en Suisse et le dernier en Afrique du Sud. Les trois régions d'essai présentaient une topologie et un climat très différents. L'analyse et les modèles associés apportent donc une plus grande connaissance des performances des radars passifs. Les études se concentrent sur les effets de propagation dans les bandes VHF et UHF en fonction des trajets multiples et des conditions climatiques.

Les relevés et les modèles apparaissant dans le présent rapport permettent de tirer plusieurs conclusions.

- Les récepteurs des radars passifs en bande FM qui se trouvent près du sol (à une hauteur de moins de 10 mètres) et raisonnablement loin de l'émetteur de référence (base de radionavigation supérieure à 20 km) se situeront très probablement dans le premier creux de propagation par trajets multiples et pâtiront de pertes de signal.
- La profondeur du creux de propagation par trajets multiples dépend (entre autres facteurs) des propriétés électromagnétiques de la surface réfléchissante. Les changements de conductivité et de permittivité dus aux changements d'état du sol peuvent avoir des effets importants sur le coefficient de réflexion.

Les données de terrain librement accessibles ne sont pas suffisamment précises pour prédire avec un degré de confiance acceptable les pertes par trajets multiples à un faible angle d'incidence en mode bistatique.

Le chapitre 2 montre qu'il n'existe aucune preuve concluante que les précipitations ou autres phénomènes météorologiques aient des effets significatifs sur la puissance reçue.

Le chapitre 3 étudie les caractéristiques de la propagation radioélectrique troposphérique, étant donné son importance pour le radar passif. Les erreurs relatives à sa prédiction nuisent en fin de compte aux statistiques de détection anticipée du radar, ce qui pourrait avoir des conséquences sur la planification des réseaux et sur les performances globales. De même, les variations de perte de la liaison entraînent des variations du SINR, par le biais de l'influence sur le trajet direct, le brouilleur, l'écho et les interférences radar. Le présent rapport explore à la fois des méthodes de modélisation et de mesure de ces effets.

Chapter 1 – PROPAGATION STUDY

This report presents details and results from a propagation study conducted by Prof. Daniel O'Hagan at the University of Cape Town, South Africa. The aim of the investigation is to measure and quantify various propagation effects in the commercial FM radio band, in the context of FM based passive bistatic radar.

1.1 SCOPE

Propagation of EM waves through the environment can be an immensely complex process. While individual phenomena, like refraction, diffraction, atmospheric attenuation, etc. are quite well understood, there is still a large discrepancy between simulated predictions, theoretical calculations, and measured signals under certain circumstances.

1.2 EXPERIMENTAL SETUP

Several transmitter locations were considered for this study, with Beaufort West being selected as the final candidate. The transmitter for this town, which is located in the Greater Karoo region of the Western Cape, South Africa, presents several advantages:

- There are two national roads that run away from the transmitter in a relatively straight radial direction.
- Human settlements, and therefore also FM transmitters, are spaced far apart in this region of the country. Signal propagation can be measured for long distances without interference from neighbouring stations.

1.2.1 Physical Geometry

Figure 1-1 shows the physical geometry around the Beaufort West transmitter. The transmitter itself is situated on a mountain approximately 1800 m above mean sea level, while the measurement area ranges in elevation from 500 m to 800 m. Two routes were used for measuring signal power levels: the N1, which runs in a south-westerly direction, and the N12, which runs almost due south. The intersection of these two roads, at -32.376383 22.526943, was used as the starting point for measurements.

Figure 1-1: Google Earth Illustration of the Physical Geometry.

1.2.2 Measurement Setup

A mobile measurement unit was created by mounting several antennas on a service vehicle, which was then driven along the N1 and N12 roads at 60 km/h. Measurement equipment was used to record signals on a continuous basis. The measurement equipment consisted of:

- A ComRad passive radar receiver (designed by Peralex), which recorded raw IQ data from three input channels.
- A SkyI-7000 spectrum monitoring receiver (designed by GEW), which continuously scanned the entire FM band from 88 MHz to 108 MHz, recording power levels of any detected FM radio stations.
- A smartphone-based GPS recorder.

The ComRad receiver allows for the simultaneous recording of three RF input channels, which would normally be used to process one reference and two surveillance channels when operating as a passive radar receiver. During this measurement trial it was used to coherently record signals from two vertically polarized antennas, as well as one horizontally polarized antenna, for one FM radio station. The vertically polarized antennas were placed at different heights, as seen in Figure 1-2.

Figure 1-2: Photo of the Mobile Measurement Unit.

The SkyI-7000 is a calibrated, wideband, spectrum monitoring device produced by GEW with very sophisticated functionality. It was employed as a secondary measurement device, to corroborate data collected with ComRad.

1.2.3 AREPS Simulation

Several simulations were executed using the Advanced Refractive Effects Prediction System. While this does not take multipath into account, it does give an indication of signal losses due to other terrain effects.

1.3 PROPAGATION MEASUREMENTS

This section will present results from the measurement trail. A measurement in this context refers to the continuously recoded data of a single trip along one of the two routes. Five trips were made: two along the N12 and three along the N1. Each measurement recoded seven data streams: three ComRad channels and four SkyI stations. All ComRad recordings are of the same FM radio station, 93.9 MHz, while the SkyI detected only the four licensed radio stations (90.7 MHz, 93.9 MHz, 100.7 MHz, 104.3 MHz).

1.3.1 N1 Results

Three measurements were taken along the N1, as detailed in Table 1-1 and illustrated in Figure 1-3 and Figure 1-4.

Table 1-1: N1 Measurement Details.

Measurement 1 – Driving away from transmitter			
Date:	1 July 2017		
Start Time:	16:50	**End Time:**	17:55
Start Location:	-32.376383, 22.526943	**End Location:**	-32.784417, 21.972970
Measurement 2 – Driving towards transmitter			
Date:	1 July 2017		
Start Time:	18:32	**End Time:**	19:40
Start Location:	-32.784417, 21.972970	**End Location:**	-32.376383, 22.526943
Measurement 3 – Driving away from transmitter			
Date:	2 July 2017		
Start Time:	07:50	**End Time:**	09:00
Start Location:	-32.376383, 22.526943	**End Location:**	-32.784417, 21.972970

1.3.2 N12 Results

Two measurements were taken along the N12, as detailed in Table 1-2 and illustrated in Figure 1-5.

Table 1-2: N12 Measurement Details.

Measurement 1 – Driving away from transmitter			
Date:	1 July 2017		
Start Time:	09:26	**End Time:**	11:09
Start Location:	-32.376383, 22.526943	**End Location:**	-33.242292, 22.545763
Measurement 2 – Driving towards transmitter			
Date:	1 July 2017		
Start Time:	12:03	**End Time:**	13:39
Start Location:	-33.242292, 22.545763	**End Location:**	-32.376383, 22.526943

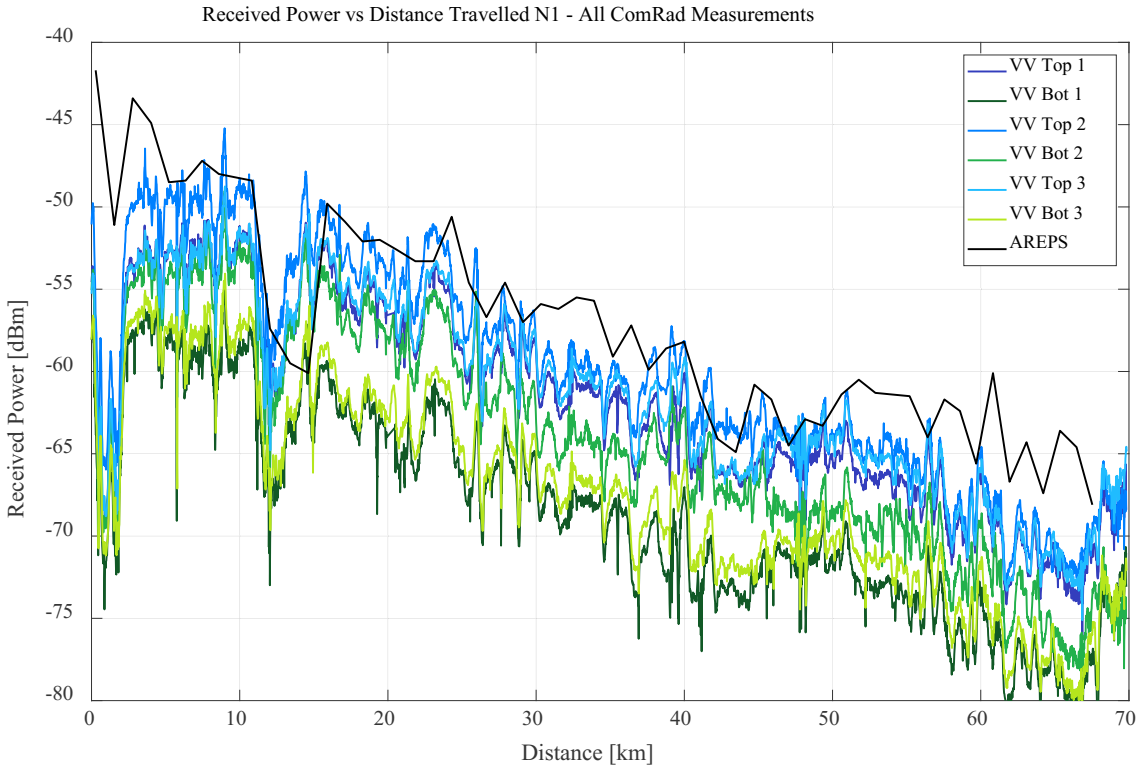

Figure 1-3: All ComRad Measurements Along the N1.

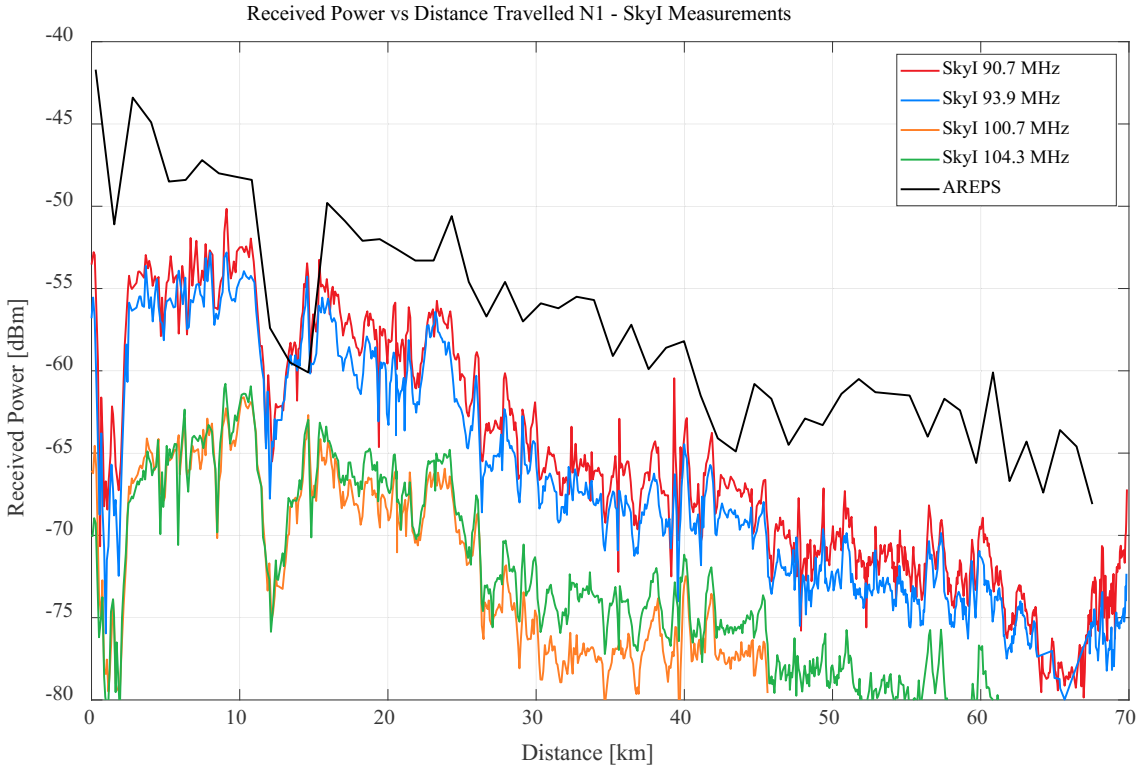

Figure 1-4: All SkyI Measurements Along the N1.

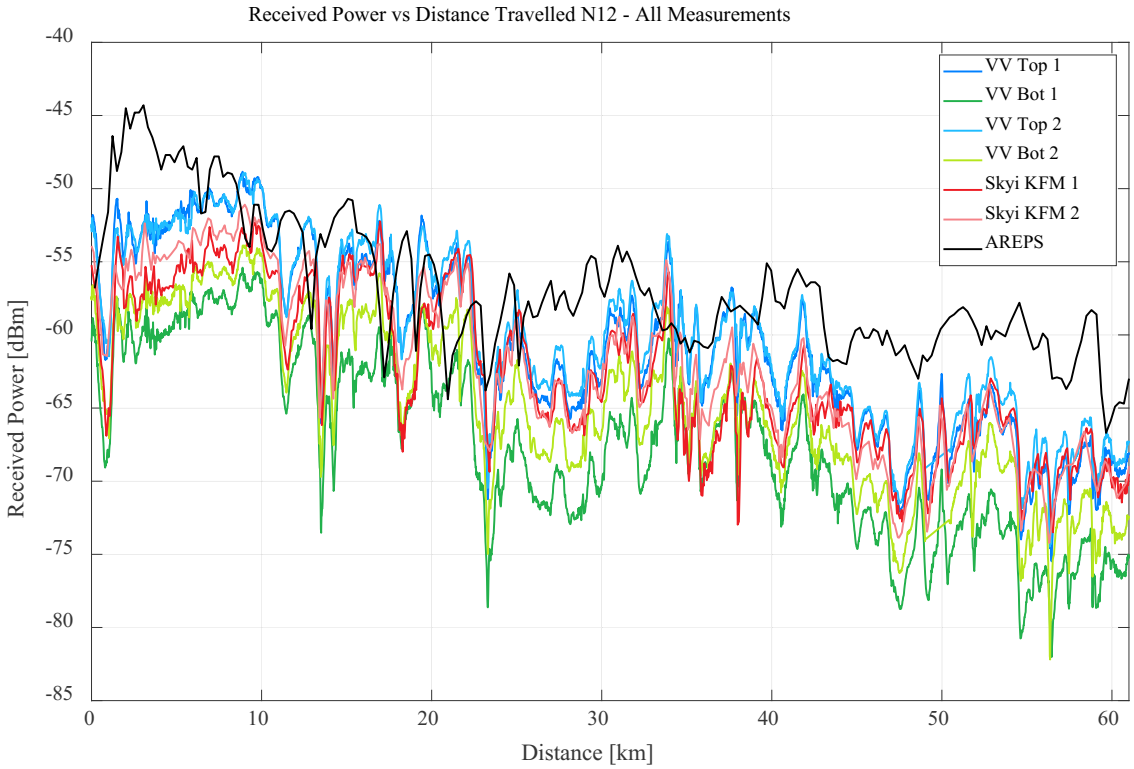

Figure 1-5: All ComRad Measurements Taken Along the N12.

1.3.3 Multipath Observations

Figure 1-6 and Figure 1-7 show the difference in received power between the two vertically polarized channels (ComRad measurement). The difference in received power remains almost constant, with receding measurements at about 7 dB, while approaching measurements are approximately 4 to 5 dB. This corresponds to a scenario where the receiver is in a multipath null, an increase in antenna height will move away from that null and result in increased receive power.

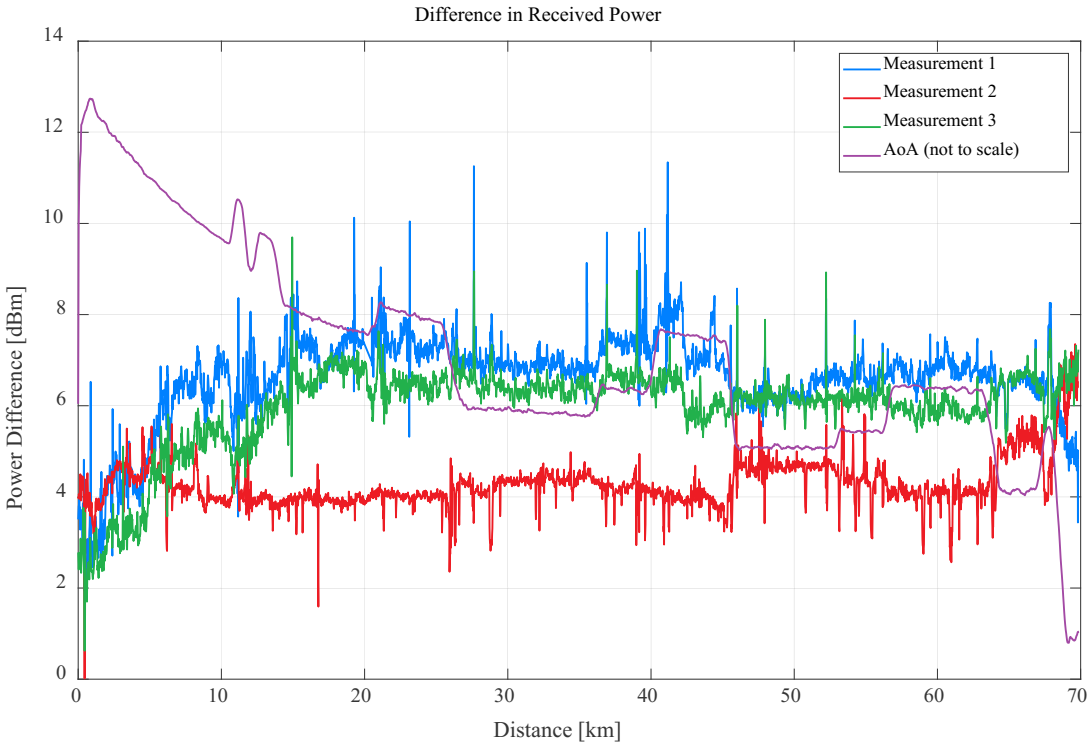

Figure 1-6: Difference in Received Power Levels Between the Upper V-pol and Lower V-pol Antennas, as Measured Along the N1. The angle-of-arrival of the incoming signal is also shown, with some correlation clearly visible.

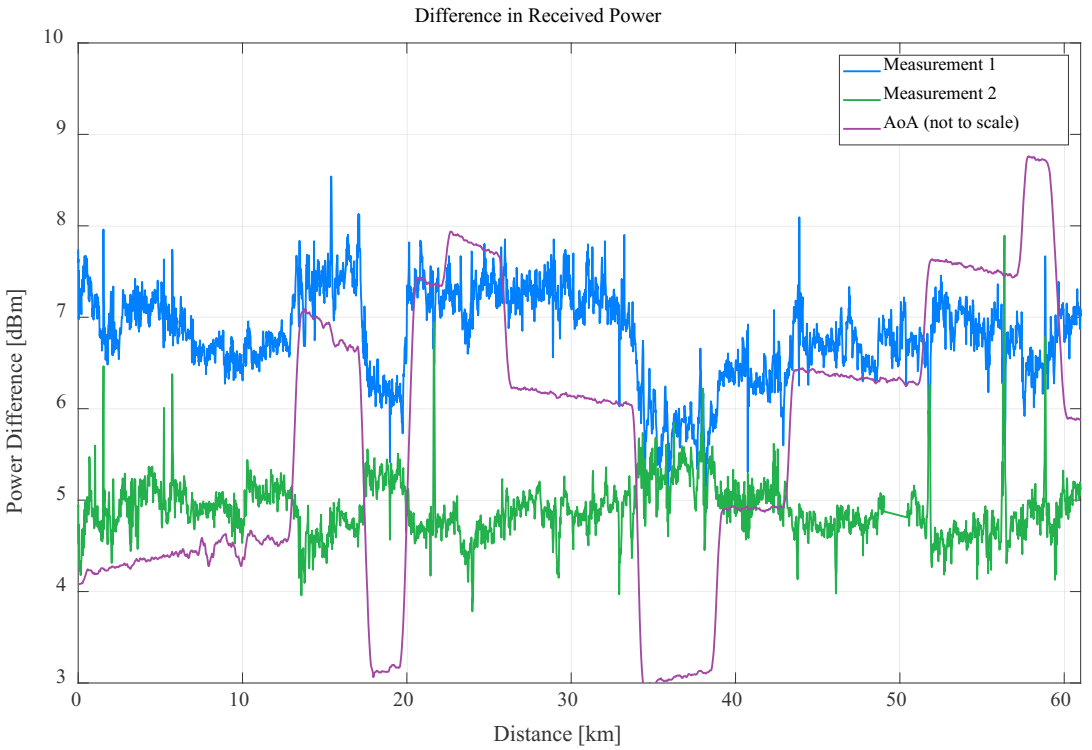

Figure 1-7: Difference in Received Power Levels Between the Upper V-pol and Lower V-pol Antennas, as Measured Along the N12.

1.4 MULTIPATH MODEL

1.4.1 Reflection of EM Waves

Stratton discusses in detail how an electromagnetic plane wave is refracted and reflected at the boundary of two isotropic media [1]. This is illustrated in Figure 1-8.

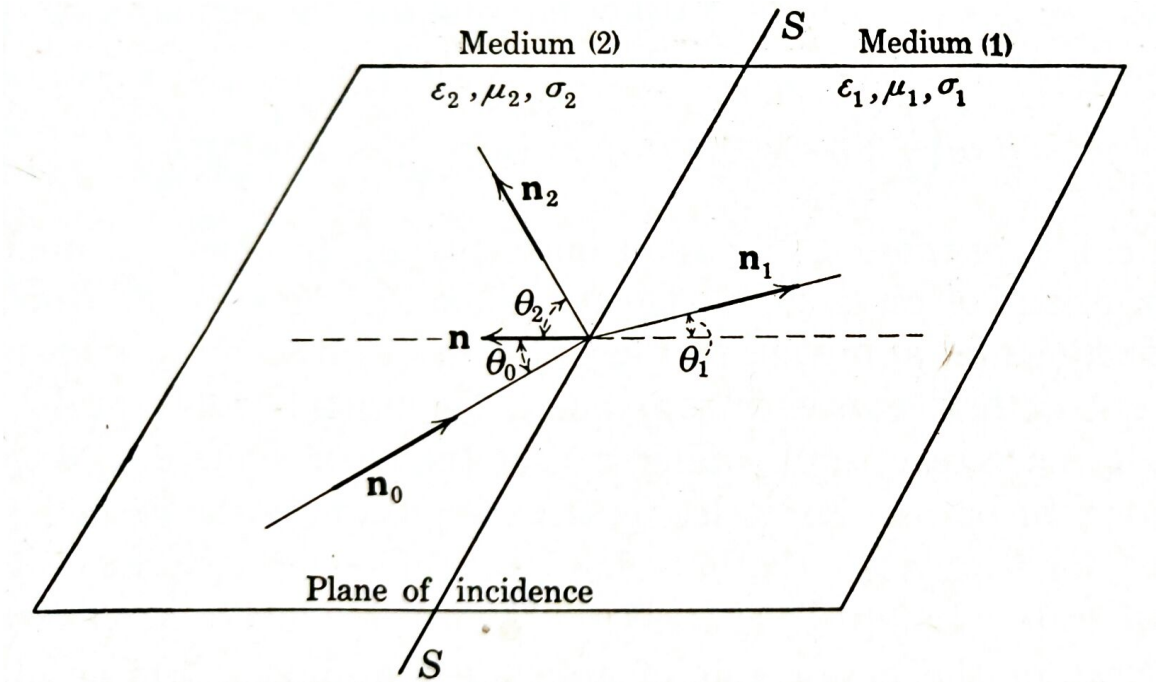

Figure 1-8: Diagram of the Incident, Refracted, and Reflected EM Plane Wave when Encountering a Flat Boundary Between Two Isotropic Media (taken from Ref. [1]).

The incident wave is given by:

$$\mathrm{E_i} = \mathrm{E_0} e^{ik_2 \mathrm{n_0} \cdot \mathrm{r} - i\omega t} \tag{1-1}$$

$$\mathrm{H_i} = \frac{k_2}{\omega \mu_2} \mathrm{n_0} \times \mathrm{E_i} \tag{1-2}$$

where **r** is the position vector and $\mathbf{E_0}$ is the complex amplitude of the incident wave. In the case where $\mathbf{E_0}$ is in the plane of incidence, which would correspond to vertical polarization if *S* is a horizontal ground plane, the reflected wave can be expressed as:

$$\mathrm{H_r} = \frac{\mu_2 k_1^2 \cos\theta_0 - \mu_1 k_2 \sqrt{k_1^2 - k_2^2 \sin^2\theta_0}}{\mu_2 k_1^2 \cos\theta_0 + \mu_1 k_2 \sqrt{k_1^2 - k_2^2 \sin^2\theta_0}} \mathrm{H_0} \tag{1-3}$$

$$\mathrm{E_r} = -\frac{\omega \mu_2}{k_2} \mathrm{n_2} \times \mathrm{H_r} \tag{1-4}$$

The reflected E-field is therefore a rotated, scaled, phase-shifted version of the incident E-field. This can be expressed as a complex reflection coefficient:

$$\Gamma_V = \frac{\mu_2 k_1^2 \cos\theta_0 - \mu_1 k_2 \sqrt{k_1^2 - k_2^2 \sin^2\theta_0}}{\mu_2 k_1^2 \cos\theta_0 + \mu_1 k_2 \sqrt{k_1^2 - k_2^2 \sin^2\theta_0}} \tag{1-5}$$

$$k_1 = \alpha_1 + i\beta_1$$

$$\alpha_1 = \omega \sqrt{\frac{\mu_1 \epsilon_1}{2}\left(\sqrt{1 + \frac{\sigma_1^2}{\epsilon_1^2 \omega^2}} + 1\right)}$$

$$\beta_1 = \omega \sqrt{\frac{\mu_1 \epsilon_1}{2}\left(\sqrt{1 + \frac{\sigma_1^2}{\epsilon_1^2 \omega^2}} - 1\right)}$$

The reflection coefficient is a complex function of frequency, incidence angle, and material properties. The graphs in Figure 1-9 and Figure 1-10 plot the magnitude and phase of Γ_V for a particular set of material properties (typical dry soil).

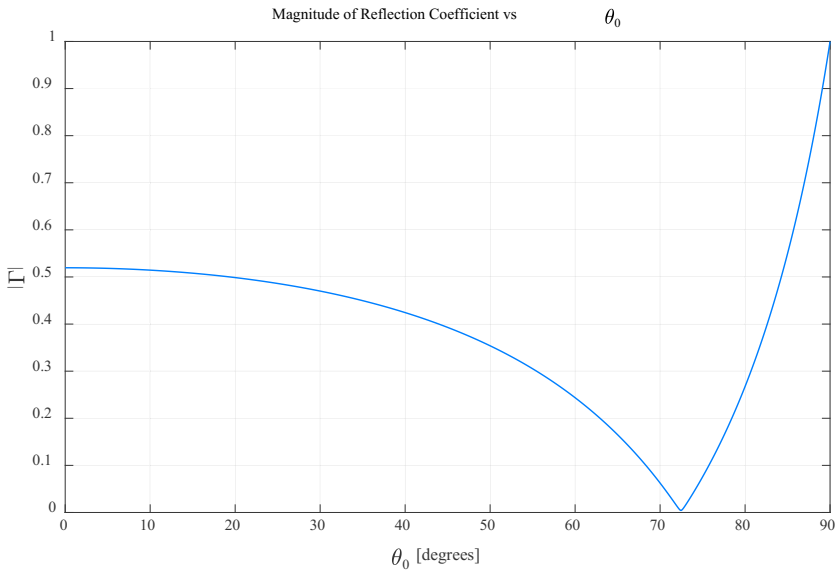

Figure 1-9: Magnitude of Reflection Coefficient at 93.3 MHz for Dry Soil.

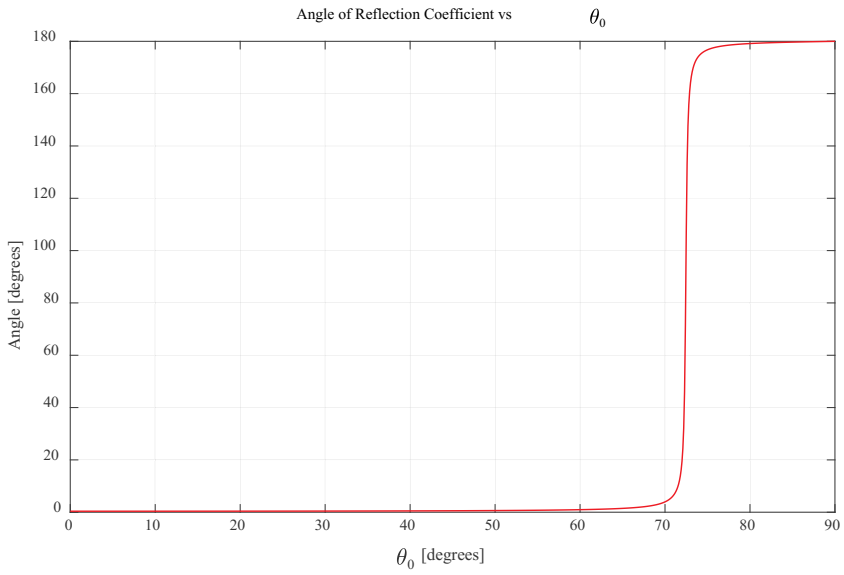

Figure 1-10: Phase of Reflection Coefficient at 93.3 MHz for Dry Soil.

1.4.2 Specular Multipath

Consider the Tx-Rx geometry in Figure 1-11. There are two paths that a signal can follow, resulting in two differently scaled, time-delayed copies of the transmit signal reaching the receiver:

$$f_{Tx}(t) = A\cos(2\pi f_0 t) \tag{1-6}$$

$$f_{Rx}(t) = A_d f_{Tx}(t - t_d) + A_r \Gamma_r f_{Tx}(t - t_r) \tag{1-7}$$

The time delays t_d and t_r correspond to the time it takes the transmit signal to travel along paths D_d and D_r respectively.

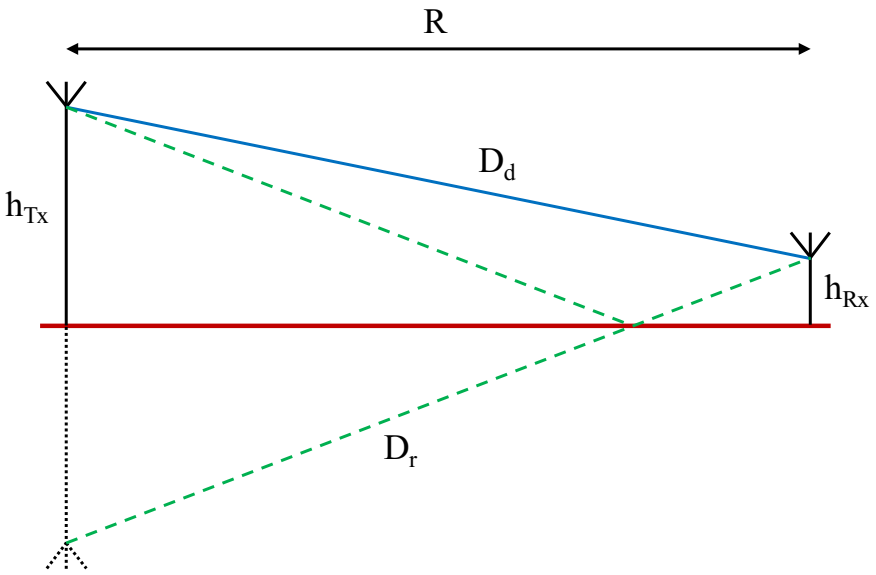

Figure 1-11: Simple Tx-Rx Geometry.

Assuming the change in amplitude due to propagation loss is approximately equal along the direct and reflect paths, i.e. $A_d = A_r$:

$$f_{Rx}(t) = A_d\left[\cos\left(2\pi f_0(t - t_d)\right)\right.$$

$$\left.+\Gamma\cos\left(2\pi f_0\left(t - (t_d + t_\Delta)\right) + \Phi_\Gamma\right)\right] \quad (1\text{-}8)$$

$$= A_d M\cos(2\pi f_0(t - t_d) + \Phi_M) \quad (1\text{-}9)$$

The presence of specular multipath will change the amplitude of a received signal by a factor M and shift the phase by Φ_M, as compared to the direct path. These factors can be expressed as follows:

$$M = \sqrt{1 + 2\Gamma\cos(-2\pi f_0 t_\Delta + \Phi_\Gamma) + \Gamma^2} \quad (1\text{-}10)$$

$$\Phi_M = \arctan\left(\frac{\Gamma\sin(-2\pi f_0 t_\Delta + \Phi_\Gamma)}{1 + \Gamma\cos(-2\pi f_0 t_\Delta + \Phi_\Gamma)}\right) \quad (1\text{-}11)$$

It can be shown that for low grazing angles and a reflecting medium that is at least somewhat conductive, the complex reflection coefficient tends towards -1 at VHF. An approximate expression for the difference in path lengths can be found using Taylor series:

$$D_\Delta \approx \frac{2h_{Tx}h_{Rx}}{R} \quad (1\text{-}12)$$

Figure 1-12 shows how D_Δ changes over the course of a measurement. The free space wavelength at 100 MHz is approximately 3 m, which means the phase-shift due to different physical path lengths is very small. The mobile measurement unit was therefore operating fairly close to a multipath null. Figure 1-13 shows the required receiver height to create a D_Δ of half a wavelength (which would be required to cancel the 180° phase shift due to a reflection coefficient of nearly -1).

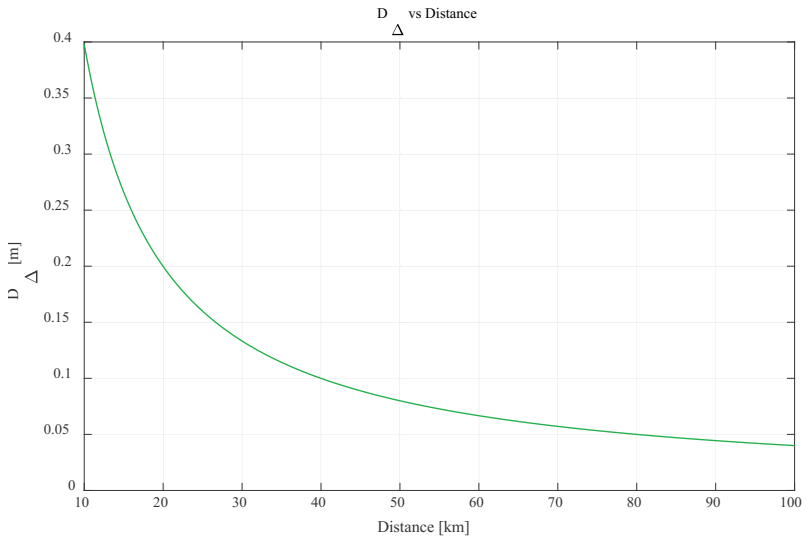

Figure 1-12: Ddelta as a Function of Distance from the Transmitter.

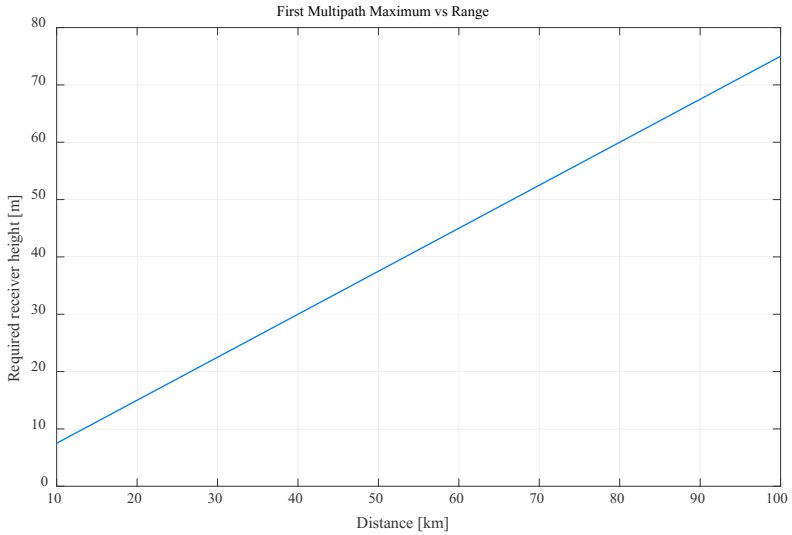

Figure 1-13: First Multipath Maximum as a Function of Distance from the Transmitter.

1.4.3 Surface Roughness

Surface roughness determines how much of the incident signal is reflected in a specular fashion (smooth surface like a mirror), and how much is reflected in a diffuse manner. The Raleigh Roughness Criterion can be used as an approximate measure of surface roughness [2]:

$$\Delta h \sin\theta < \frac{\lambda}{8} \tag{1-13}$$

1.4.4 Proposed Multipath Models

The first set of results is from a basic multipath model, which assumes the following:

- Reflection is from a single point.
- Soil properties remain constant for all reflection points and correspond to those of dry soil.
- The routes along which measurements were taken are approximately straight and move radially away from the transmitter, so that grazing angle and direct/reflect paths can be solved using measured elevation, latitude, and longitude data.

Figure 1-14 and Figure 1-15 show the predicted multipath losses. Lower grazing angles result in increased loss, which is expected.

An "Enhanced" model was also created in an attempt to account for the correlation between Angle-of-Arrival and the difference in received power between the top and bottom V-pol channels. An additional difference in height was introduced by multiplying the AoA with a suitable scaling factor. The results of this model are shown in Figure 1-16 and Figure 1-17. While these models appear to give a more accurate prediction of multipath loss, they are based on guesses at best.

The last model used terrain data from the United States Geological Survey, or USGS. The highest resolution data that is freely available for the region is divided into 1 × 1 second arcs, which is approximately 30 × 30 meters. The full geometry was solved for each measurement point, after which a similar method was used to calculate multipath loss as with the basic model. The results from this model is shown in Figure 1-18 and Figure 1-19.

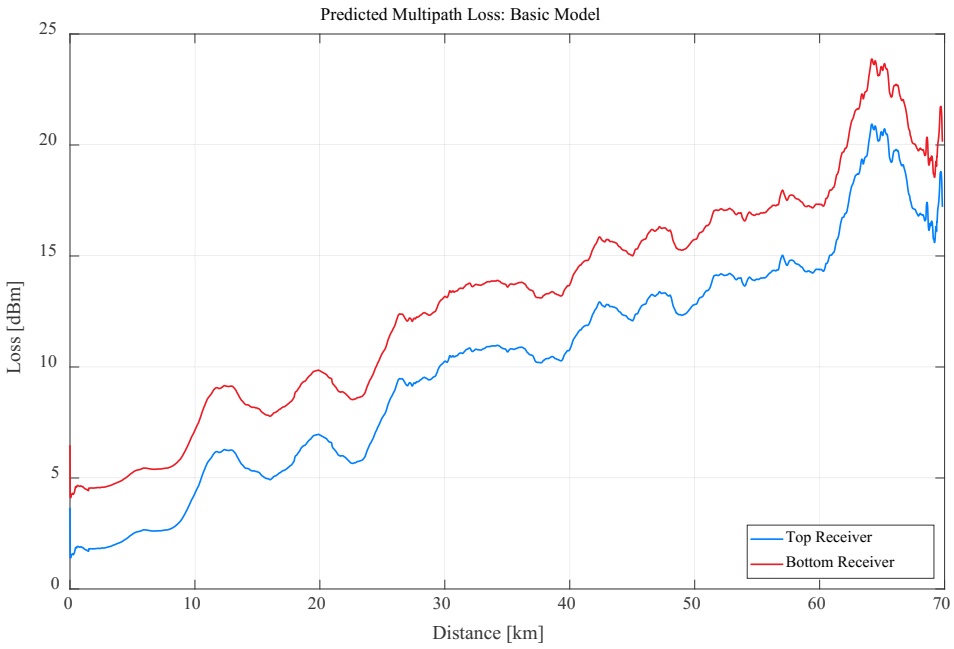

Figure 1-14: Predicted Losses Due to Multipath Interference According to a Basic Model for the N1 Route.

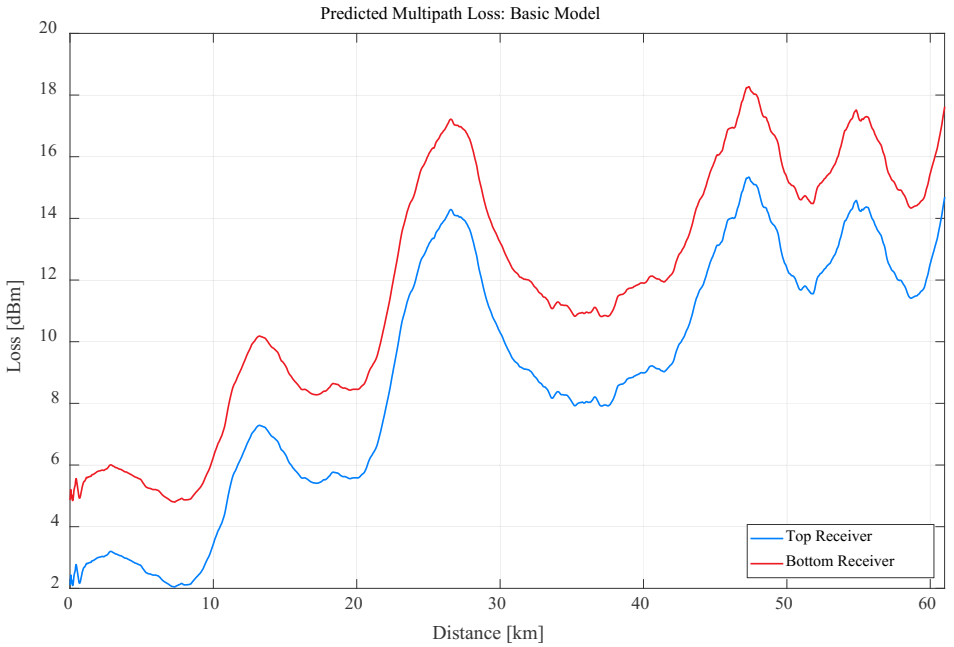

Figure 1-15: Predicted Losses Due to Multipath Interference According to a Basic Model for the N1 Route.

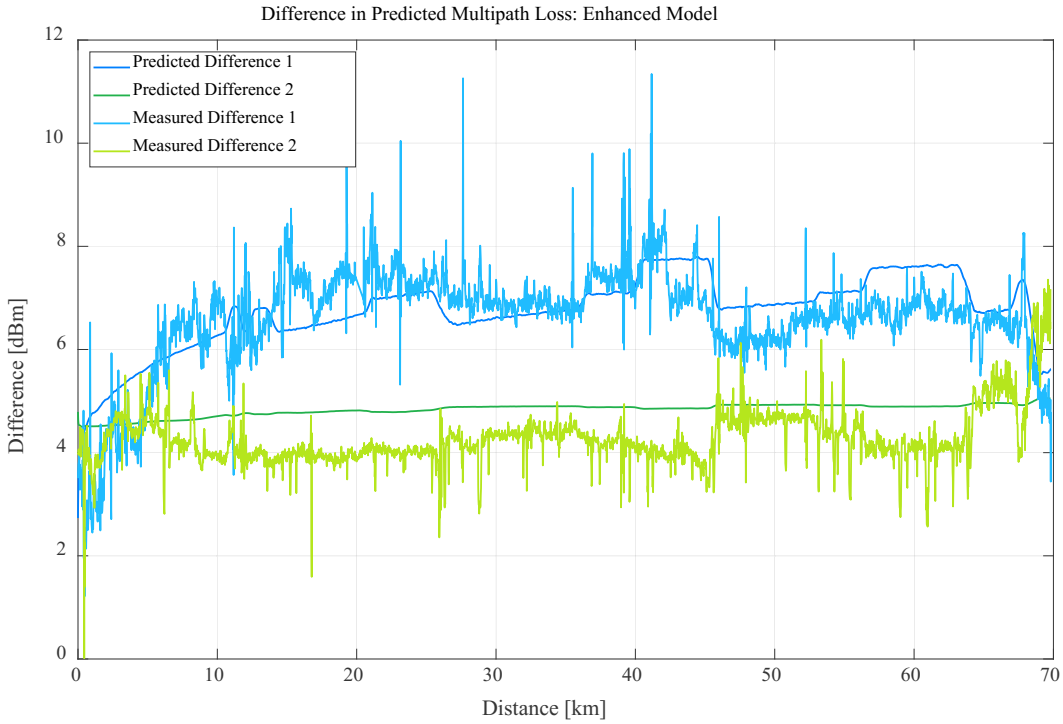

Figure 1-16: Comparison of Enhanced Multipath Model with Measured Data in Terms of the Difference in Received Power (Between the Top V-pol Antenna and the Lower V-pol Antenna) for the N1 Route.

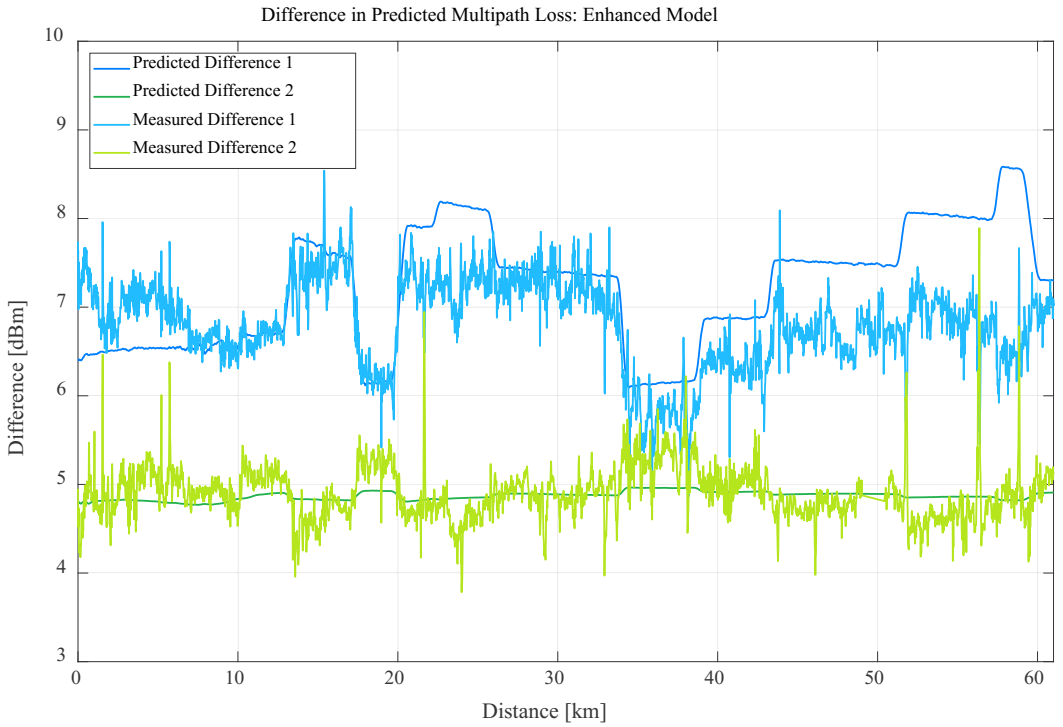

Figure 1-17: Comparison of Enhanced Multipath Model with Measured Data in Terms of the Difference in Received Power (Between the Top V-pol Antenna and the Lower V-pol Antenna) for the N12 Route.

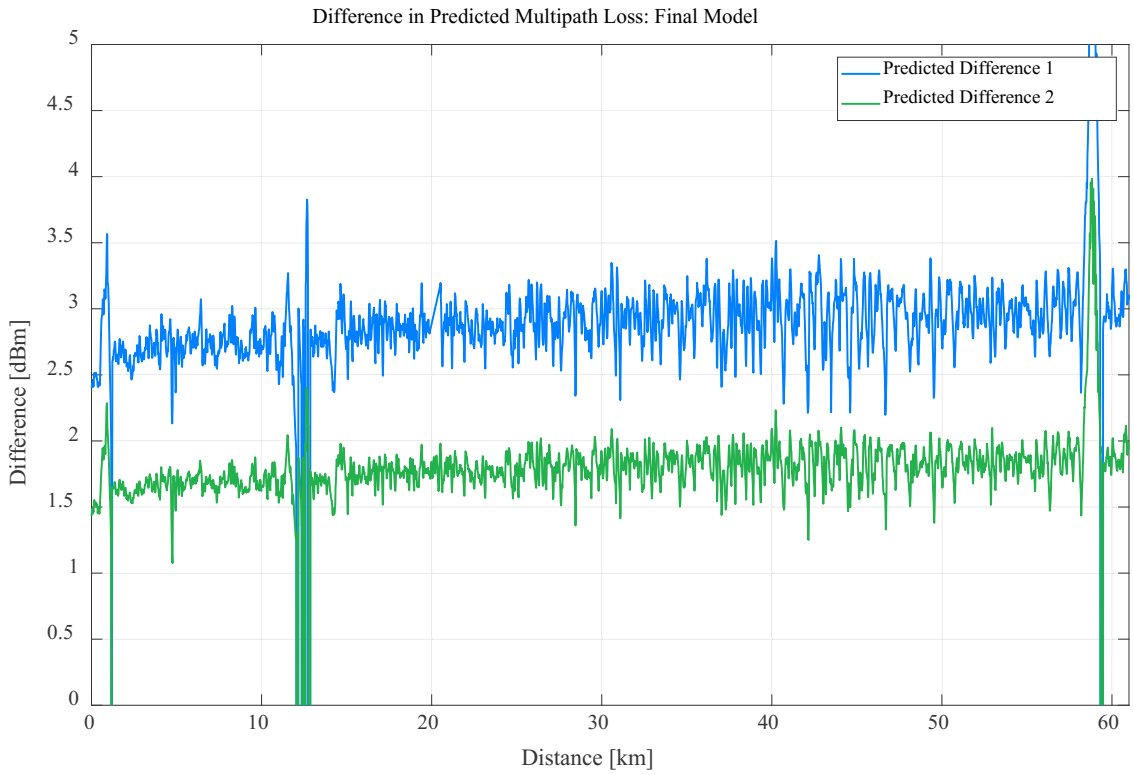

Figure 1-18: Results of the Final Multipath Model for the N1 Route.

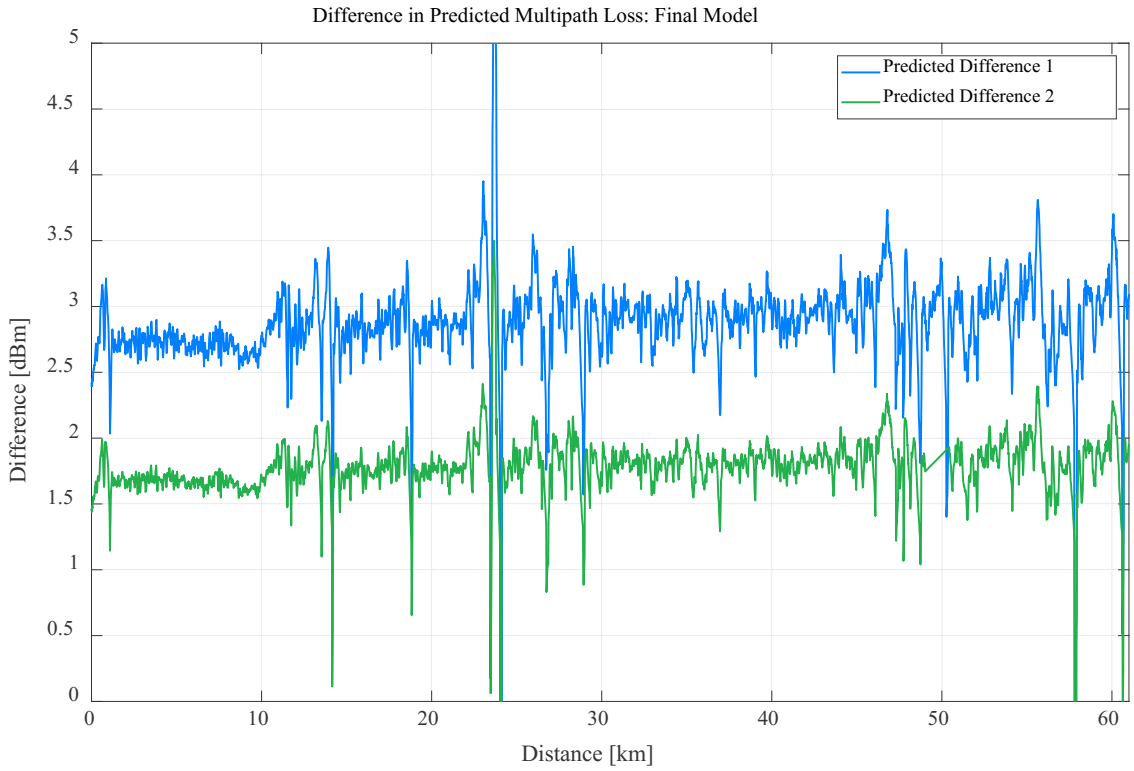

Figure 1-19: Results of the Final Multipath Model for the N12 Route.

1.5 CONCLUSION

Several conclusions can be drawn from the measurements and models that have been presented:

- FM based Passive Radar receivers that are fairly close to the ground (elevated less than 10 meters) and reasonably far from the reference transmitter (baseline longer than 20 km) will most likely be within the first multipath null and will suffer from multipath losses.
- The depth of the multipath null depends (amongst other factors) on the electromagnetic properties of the reflecting surface. Changes in conductivity and permittivity due to changing soil conditions can have significant effects on the reflection coefficient.
- Freely available terrain data is not accurate enough to predict multipath losses with any level of confidence. This is best illustrated by Figure 1-20 and Figure 1-21, where different sources of elevation data are compared.

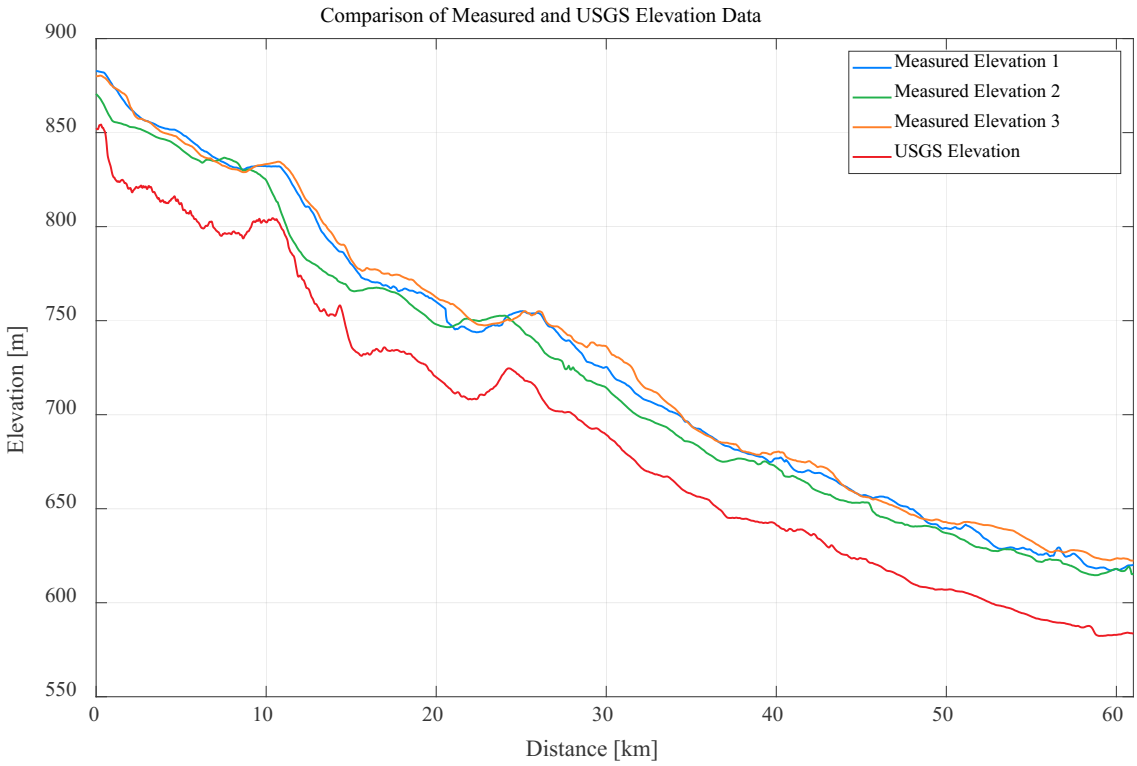

Figure 1-20: Discrepancies in Reported Elevation Along the N1.

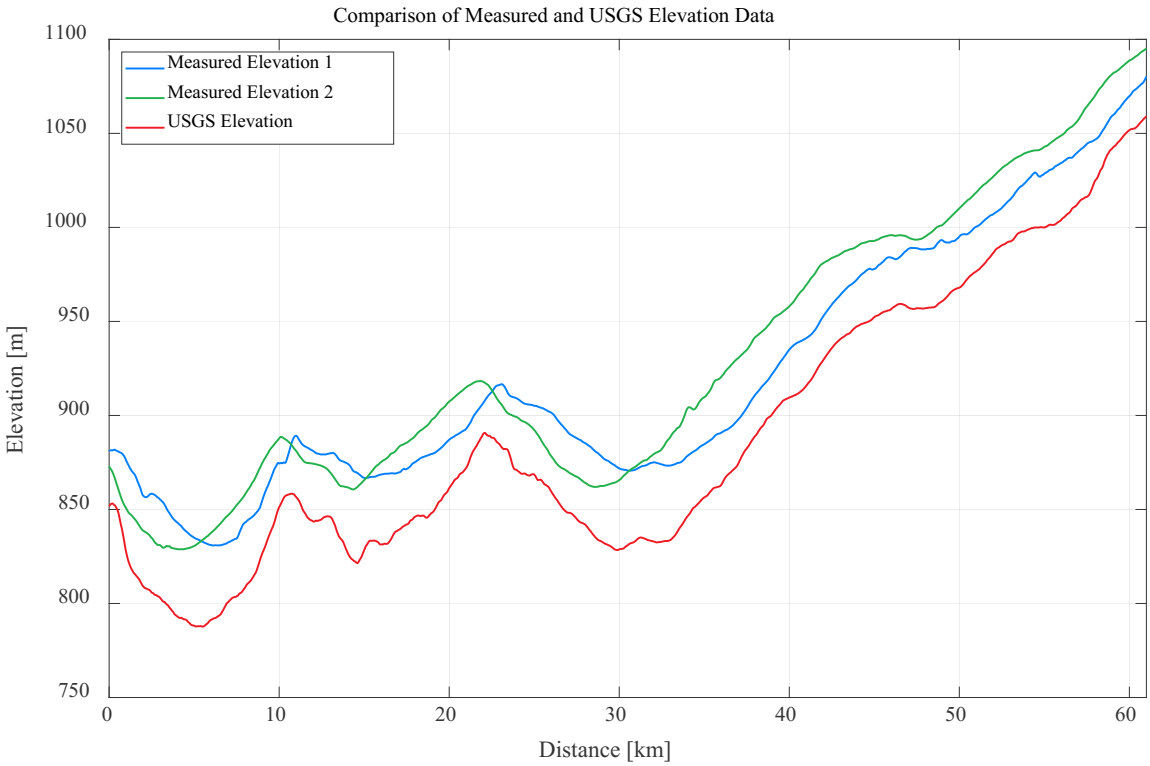

Figure 1-21: Discrepancies in Reported Elevation Along the N12.

1.6 REFERENCES

[1] J.A. Stratton, "Electromagnetic Theory," New York and London, McGraw-Hill Book Company, Inc., 1941, pp. 490-511.

[2] M.W. Long, Radar Reflectivity of Land and Sea, 2nd ed., Dedham, Ma: Artech House, Inc., 1983.

Chapter 2 – LONG-TERM MONITORING OF BROADCAST RECEPTION LEVELS IN SWITZERLAND

Passive radar is strongly dependent on the availability and reliability of the employed transmitters of opportunity. For the assessment of the coverage of a given deployment, transmitter characteristics are usually used in conjunction with terrain model data and a simplified propagation model. This, however, does not account for any statistical fluctuation in the propagation channel or the transmitter power. The present measurement and analysis was conducted to get a feeling for the behavior of the received power levels from a number of broadcasting transmitters in the FM, DAB and DVB-T band.

Over the course of more than 50 days the received power of 29 broadcast stations was monitored and weather data were collected from a nearby weather station.

In the Section 2.1, we present the measurement set-up, an overview of the results and more in-depth analyses of the statistical behavior and the correlation with weather data. Finally, we conclude and give recommendations for future work.

2.1 MEASUREMENT SETUP

The measurement was conducted in Thun, Switzerland with the following measurement equipment.

2.1.1 Antenna

HK033 by Rhode & Schwarz on the roof of Armasuisse Science + Technology in Thun. The roof height is approximately 30 m above ground.

2.1.2 Receiver

National Instruments RF Signal Analyzer PXIe-5665 with an instantaneous bandwidth of 50 MHz. The measurement software is implemented in LabVIEW. The RFSA tools in LabVIEW allow to directly fetch wide-band spectrum data without having to care about the slicing of the spectrum. In this way the entire spectrum from 88 – 800 MHz relevant for broadcasting can be captured in one fetch. The spectrum is fetched with a bin-width of app. 12 kHz and at an update rate of approximately 10 times per second. Depending on the signal bandwidth, the relevant bins are summed up to get the received channel power.

The results are written to a text-file for all FM, DAB and DVB-T channels. The resulting bandwidths after the summation of bins were 124.7 kHz, 1.62 MHz and 8.01 MHz for FM, DAB and DVB-T, respectively. The choice of these numbers is due to the restrictions in resolution bandwidth when capturing the spectrum data.

2.1.3 Post Processing

Since the captured data over 51 days yielded a very large text-file of close to 100 GB, it was not feasible to analyze the data at that level of detail. Therefore, the captured data were reduced in two ways. Firstly, only the active channels were selected and, secondly, blocks of 200 measurement points were averaged, which resulted in a final measurement update-time of approximately 20 s. The averaged data is stored in a MATLAB file and can easily be shared since its size is only about 30 MB.

2.1.4 Weather Data

The weather data were downloaded from Ref. [1]. The privately-owned weather station provides the main weather datasets such as temperature, humidity, precipitation, wind speed, and air pressure with an update every hour. Figure 2-1 shows the relative situation of receiver and weather station in Thun. The distance between the two is only 1.6 km, which ensures that even very local weather phenomena such as thunderstorms would be captured adequately for the receiver site.

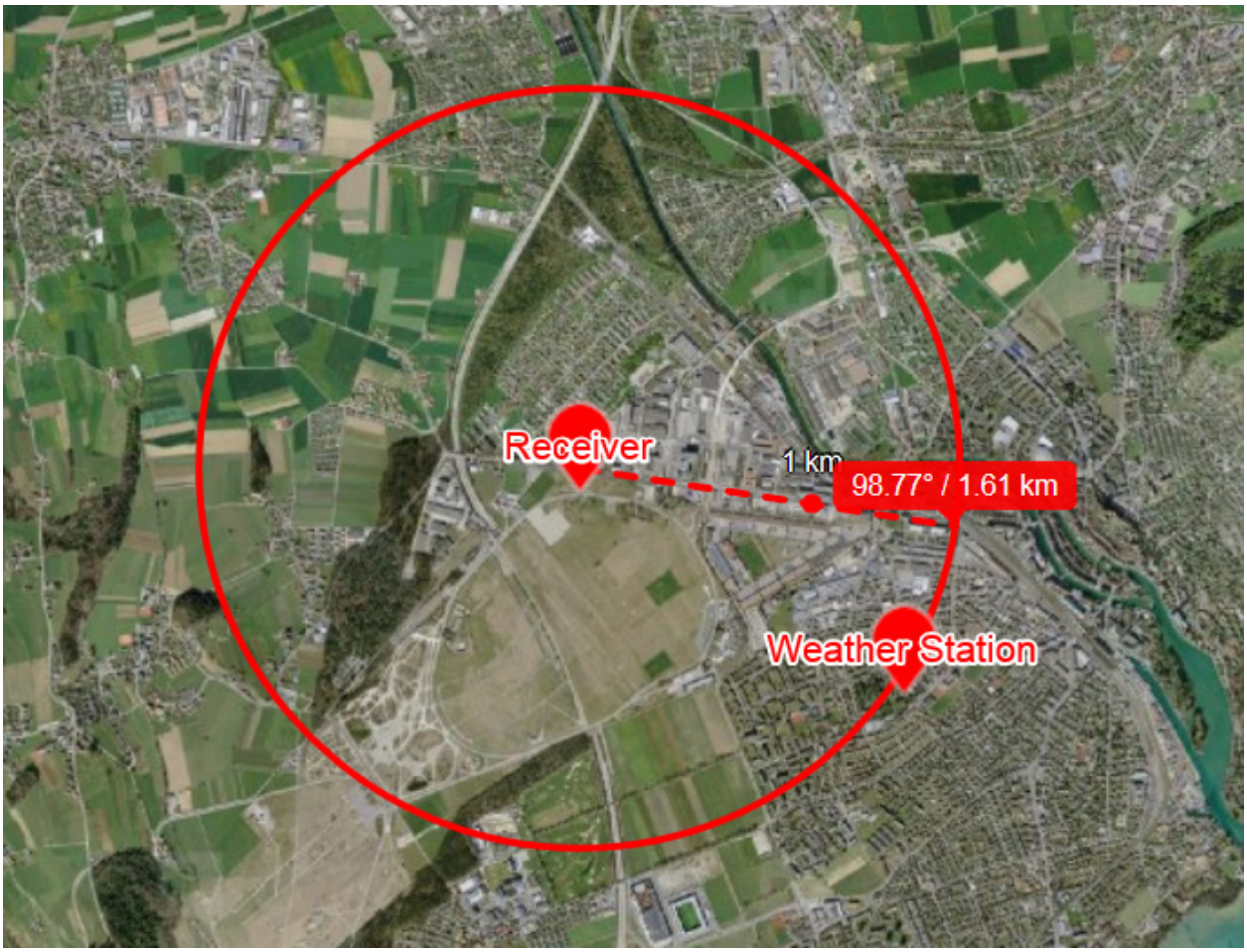

Figure 2-1: Relative Situation of Receiver and Weather Station in Thun, Switzerland.

Figure 2-2 shows plots of the obtained weather data for the period of the measurement starting on the19th of June 2017 and ending on the 9th of August 2017. Since the summer of 2017 was one of the hottest summers since the beginning of the measurement, the weather of the measurement period could be summarized as hot and dry with occasional heavy rains due to thunderstorms.

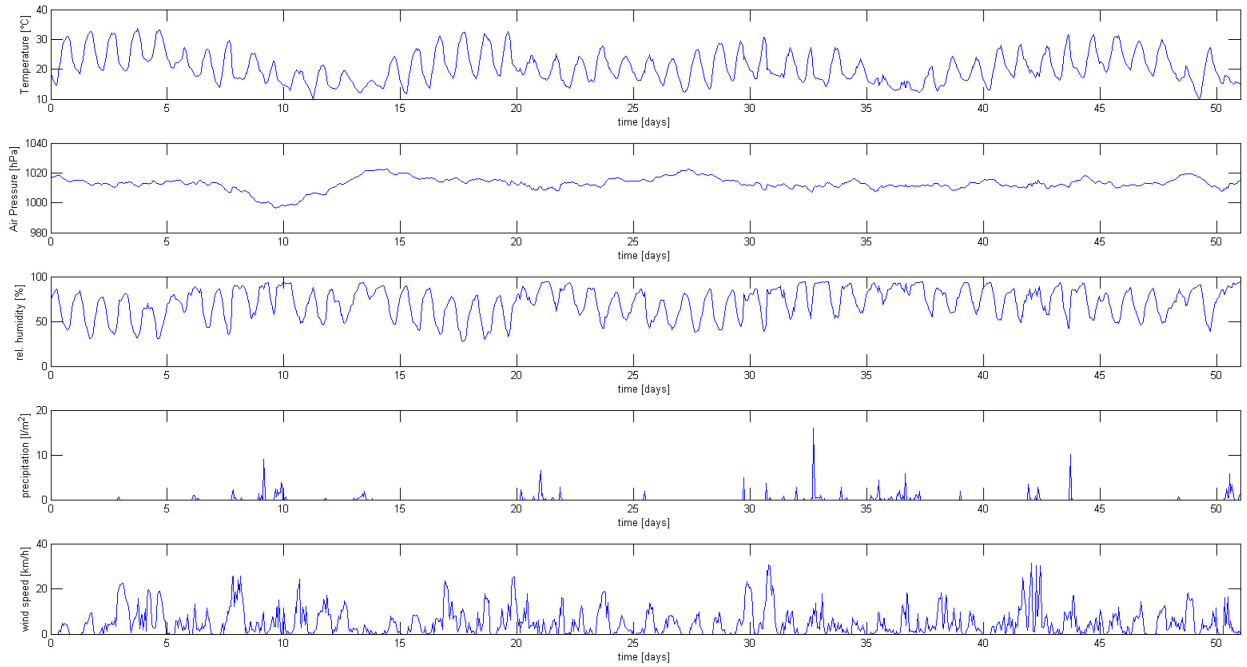

Figure 2-2: Weather Data Over the Measurement Period. From top to bottom: temperature, air pressure, relative humidity, precipitation and wind speed.

2.1.5 Transmitter Database

The characteristics of the transmitters were obtained from the official OFCOM (Federal Office of Communications) data release [2]. Since the Swiss topography allows the broadcasters to only cover a very limited area, many frequencies in the FM band are re-used even if the next cell is not very far away. Therefore, it becomes difficult, for some frequencies, to tell which of the transmitters contributes most to the reception power. In order to resolve this, the radiation patterns of the transmitters would have to be analyzed in conjunction with a propagation-loss calculation taking into account terrain data. This is left for future work. Here, the transmitters were selected based on their distance to the receiver. Furthermore, the transmitter data has, so far, only been used for the analysis of the FM band data.

2.2 RESULTS

2.2.1 Data Overview

Figure 2-3, Figure 2-4 and Figure 2-5 show the obtained data for 23 FM-band, 5 DAB and 1 DVB-T frequencies. In many of the channels there are very clear diurnal variations. These become more pronounced in channels with low power, which indicates that they could be contributions independent of the actual signal, such as “man-made-noise”.

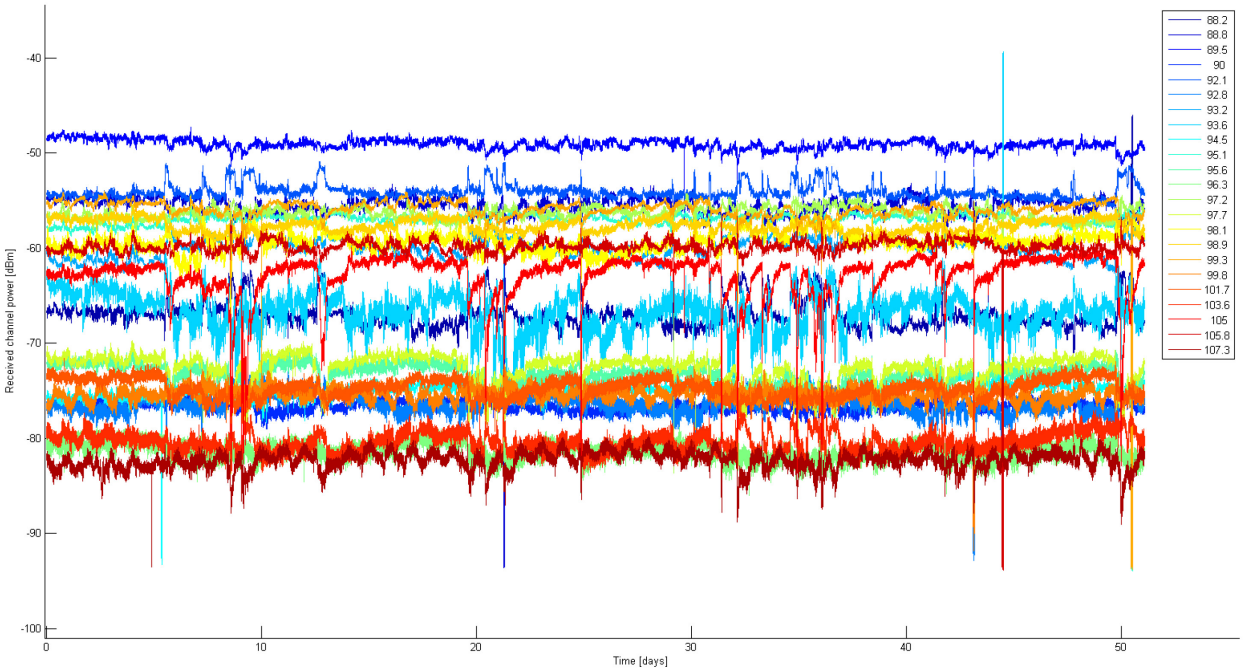

Figure 2-3: Received Power for All Active FM-Band Stations.
The legend shows the frequency in MHz.

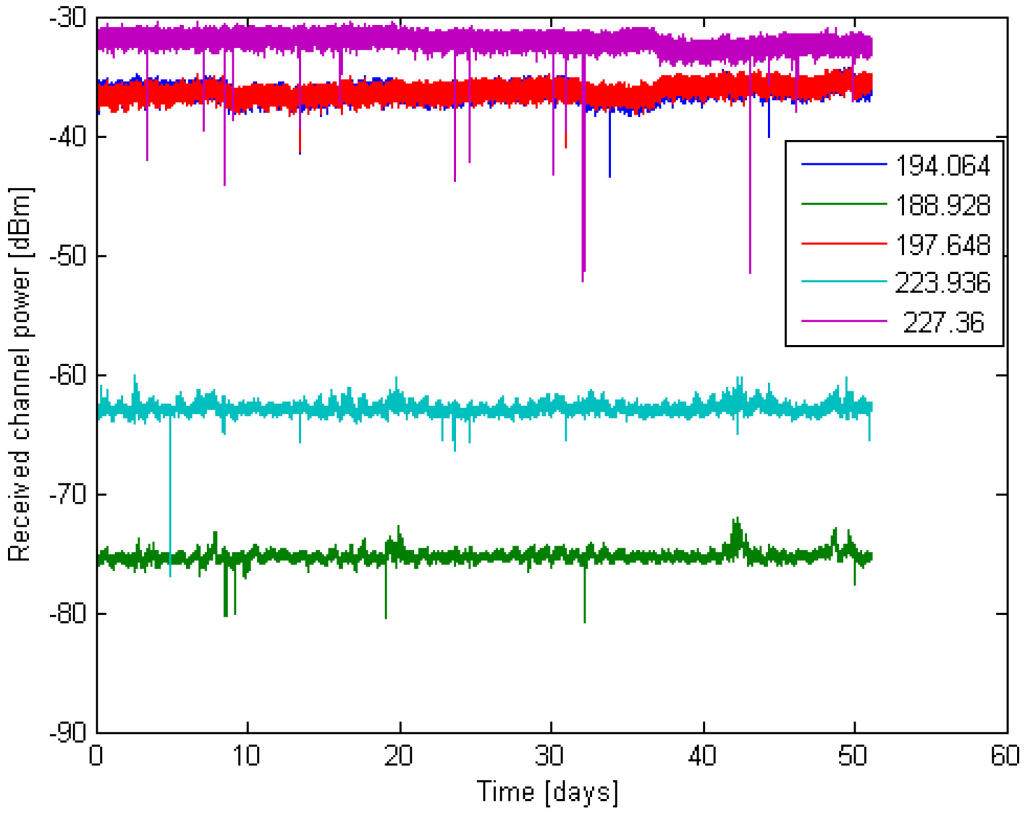

Figure 2-4: Received Power for All Active DAB Frequencies.
The legend shows the frequency in MHz.

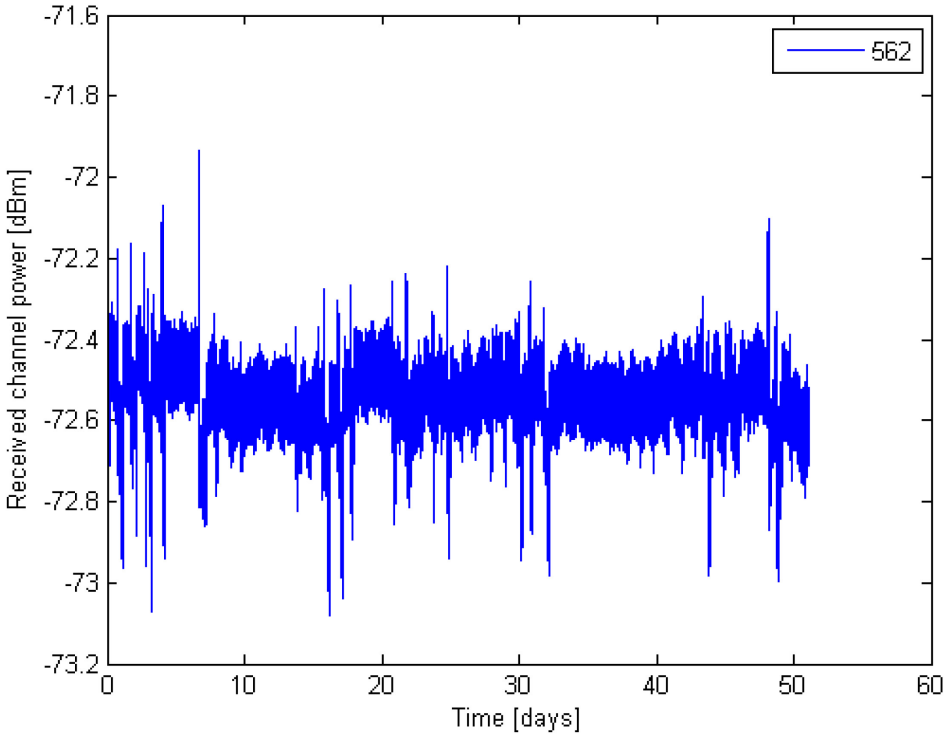

Figure 2-5: Received Power for the Only Active DVB Frequency of 562 MHz.

In a great number of the channels one can observe that there are several short but very deep troughs. These are most probably due to some operational problems or manipulations at the transmitter site and do not have anything to do with propagation phenomena.

The strongest variations can be observed in the FM-band data, which is undoubtedly partly due to the relatively small measurement bandwidth. Fluctuations of up to 5 – 10 dB are not rare and it seems that these events of high fluctuation are occurring in most of the channels at the same time. This suggests that passive radar coverage could significantly change during these periods and the diversity gain of using several transmitters is not necessarily given.

Another interesting phenomenon is that some of the channels seem to be strongly correlated or anti-correlated.

In the Section 2.2.2 we perform a more detailed analysis on the FM-band data.

2.2.2 Statistical Analysis

One of the most important aspects for modeling passive radar coverage and reliability is a statistical measure for the availability of the transmitters of opportunity. Given the data measured as part of this experiment, we can have a look at the power distributions to draw some of the necessary conclusions. Figure 2-6 and Figure 2-7 show the Probability Density Functions (PDF) and the Cumulative Distribution Function (CDF) of the measured channels. In both cases the median has been subtracted from the data such that the plots indicate the probability for the received power to be different from the median. It becomes clear that the PDFs are quite localized such that in most cases 90% of the time the fluctuation is less than ±2 dB. A more detailed analysis of the quantiles is presented with the box-whisker plot in Figure 2-8. The boxes are bounded by the first and third quartiles, while the whiskers indicate the 5% and 95% quantile, respectively. Since there are still a great number of outliers, they have been omitted for clarity.

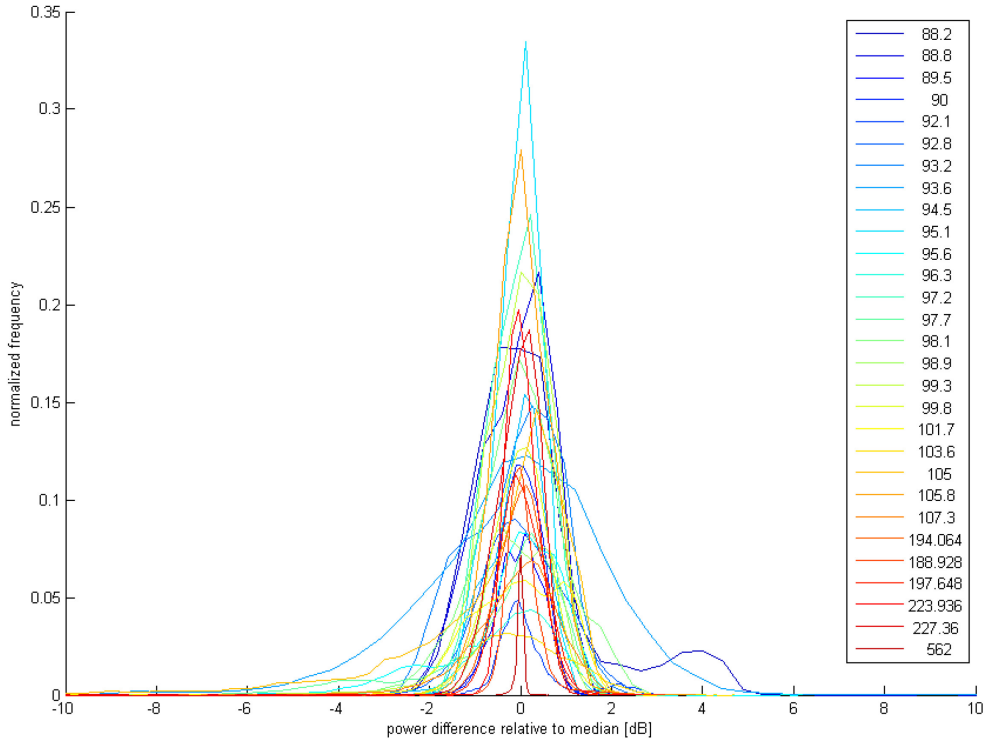

Figure 2-6: Histograms (PDFs) of Received Power Centered Around the Median. The legend shows frequency in MHz.

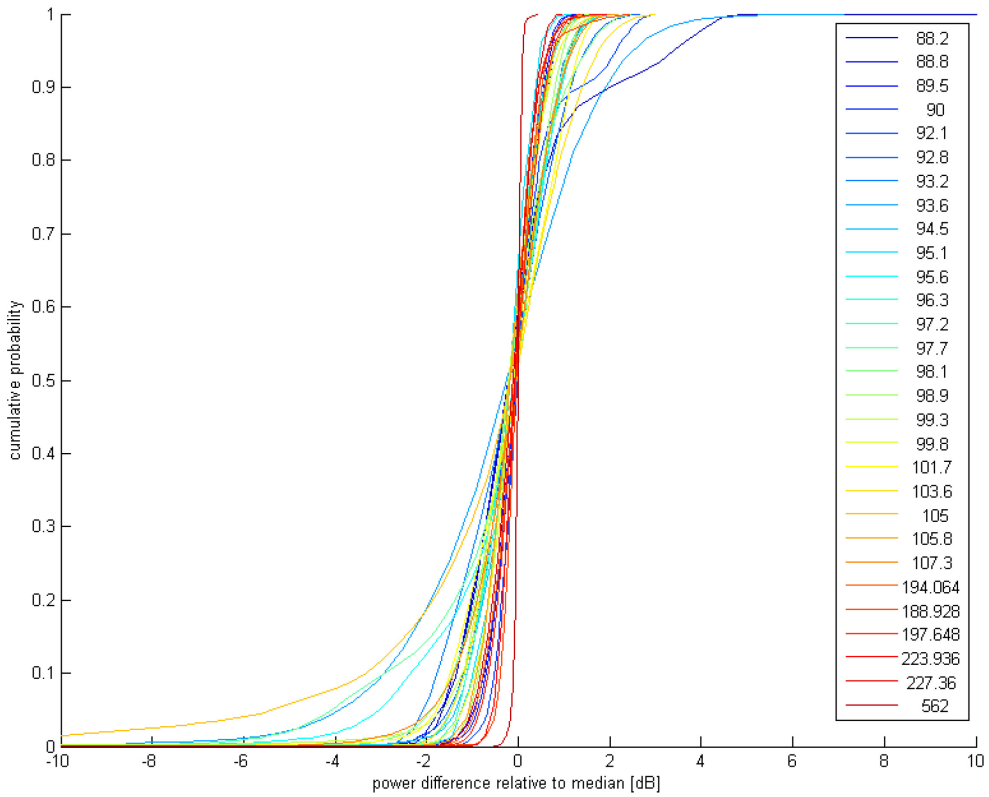

Figure 2-7: Cumulative Distribution Functions (CDF) of the Received Power Relative to the Median. The legend shows frequency in MHz.

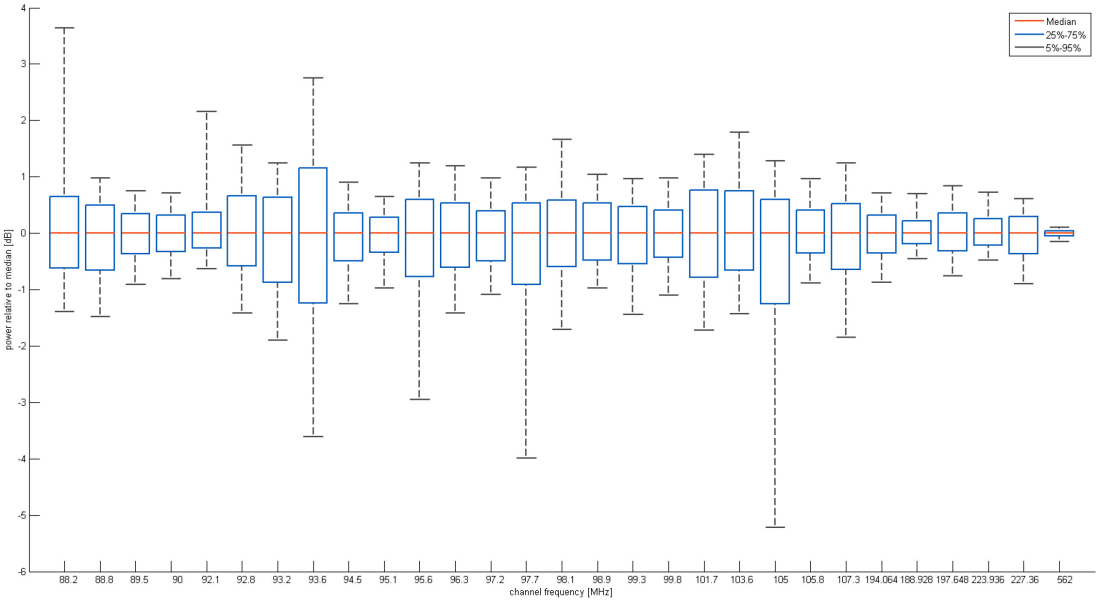

Figure 2-8: Box and Whisker Plot of Power Data Relative to the Median of Every Channel.

To account for the importance of having a sufficient number of transmitters contributing to the passive radar coverage at all times, we next look at the drop rate of the measured channels. It indicates how many channels drop by a given amount from the median value for every measurement in time. This is shown over time in Figure 2-9. To have a more detailed statistical analysis, a box and whisker plot is shown in Figure 2-10, including the outliers. It shows that there is a non-negligible risk that for certain periods some of the transmitters might contribute much less to the passive radar coverage.

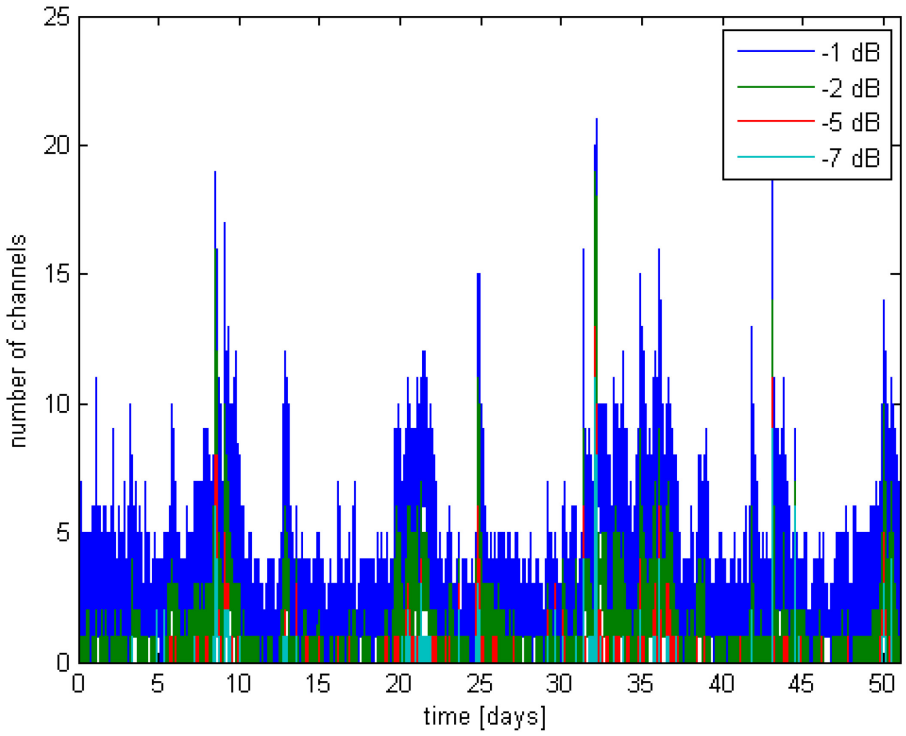

Figure 2-9: Number of Channels that Drop by a Given Value from the Median.

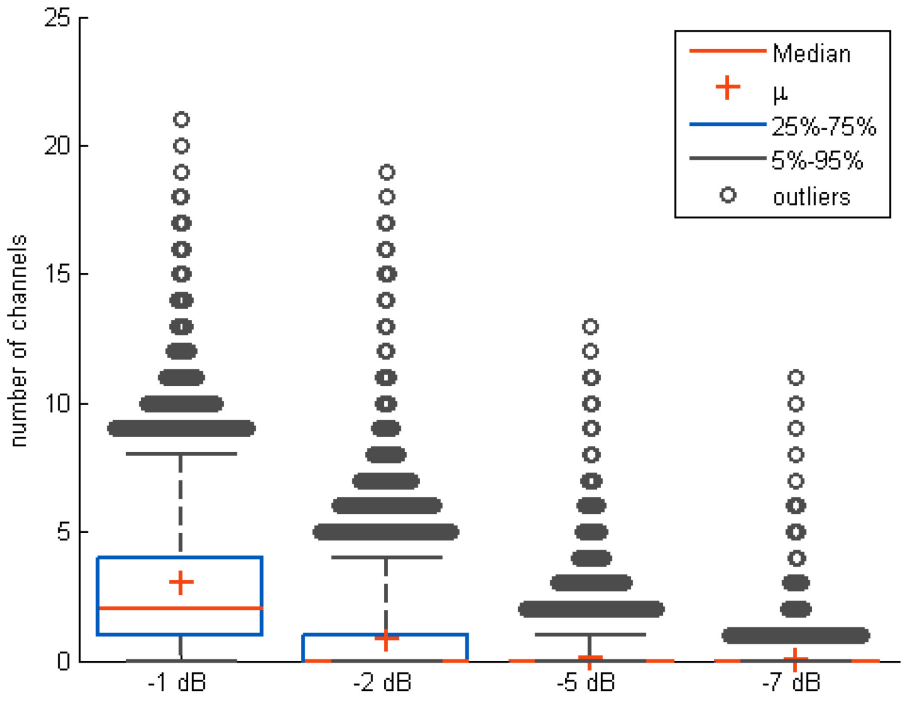

Figure 2-10: Box and Whisker Plot of Number of Channels Dropping by a Given Amount from the Median.

2.2.3 Channel Correlation

Figure 2-11 shows the cross-correlation of the data of all active channels. It shows that some channels are strongly correlated or anti-correlated. Also, it becomes clear that the transmitter types mostly correlate with transmitters of the same type (band), i.e., FM transmitters correlate with other FM transmitters but not with DAB and DVB-T transmitters and vice versa.

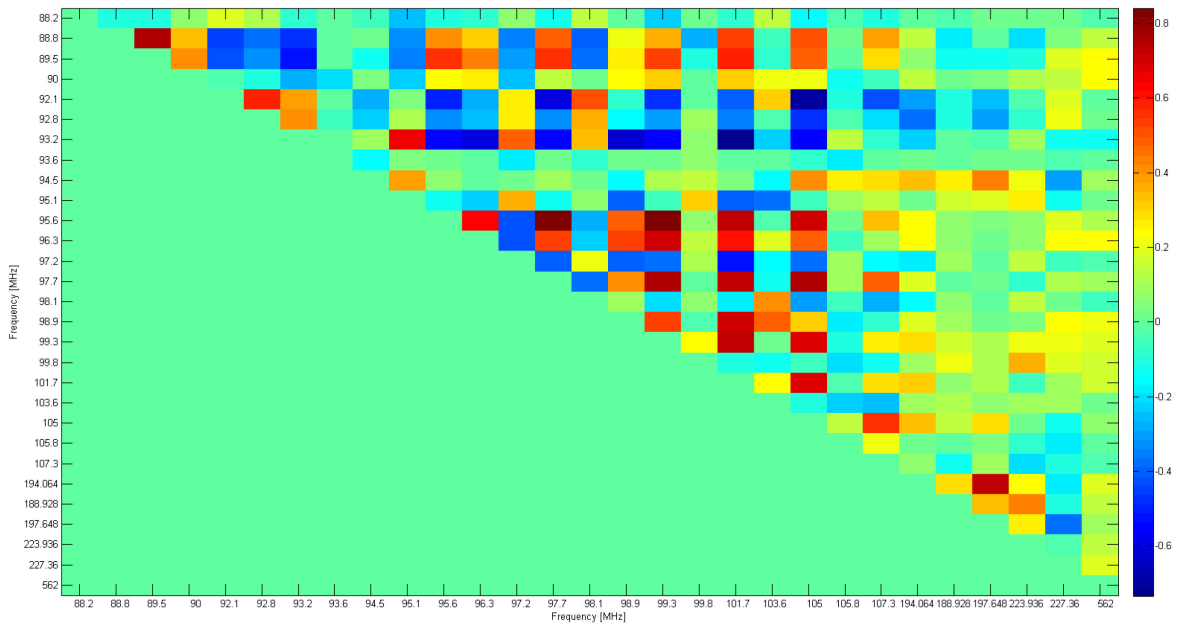

Figure 2-11: Cross-Correlation for All Channels.

In order to check whether the cross correlation of two channels is dependent on the transmitter site, the cross-correlation of every channel pair is plotted against the difference in DOA (Direction Of Arrival) in Figure 2-12. The auto-correlation pairings have been removed in this depiction such that the values with DOA difference 0° are due to different frequencies being broadcast from the same transmitter site. Again, there is no clear pattern and we see that all possible correlation values occur even for stations broadcast from the same transmitter tower.

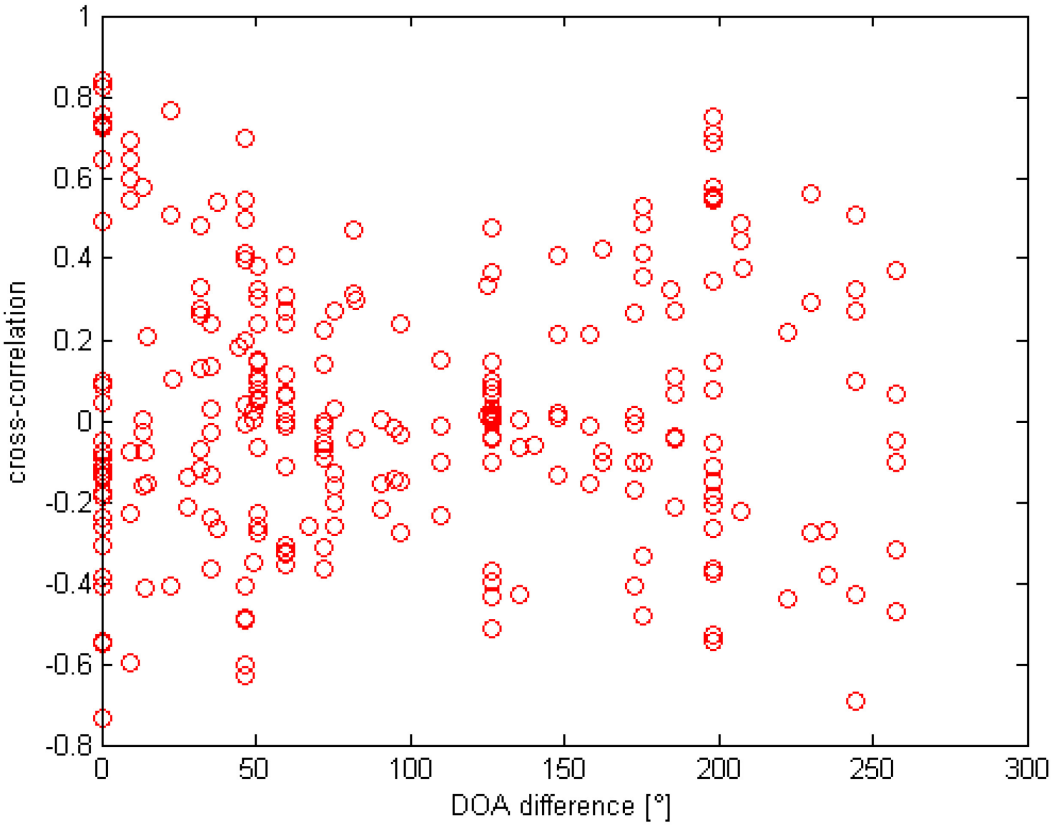

Figure 2-12: Cross-Correlation vs. Difference of DOA for FM-Band Transmitters.

2.2.4 Correlation with Weather Data

Figure 2-13 shows the correlation value of every measured channel with the available weather data sets. Before the calculation of the correlation, both weather and channel data were scaled to values between 0 and 1 and then the mean was subtracted. The resulting correlation values show the following:

1) There is no weather feature that correlates in the same way for all the measured channels. The only feature that consistently correlates weakly with all the channel data is the wind speed.

2) The correlation with all of the weather features varies strongly from channel to channel and hence we cannot conclude that any of these features influences the received power level consistently.

3) The weather features with strong diurnal variation exhibit stronger correlation but not in the same way for all the channels. This is due to the reception data also having diurnal components and most probably does not show any weather dependence.

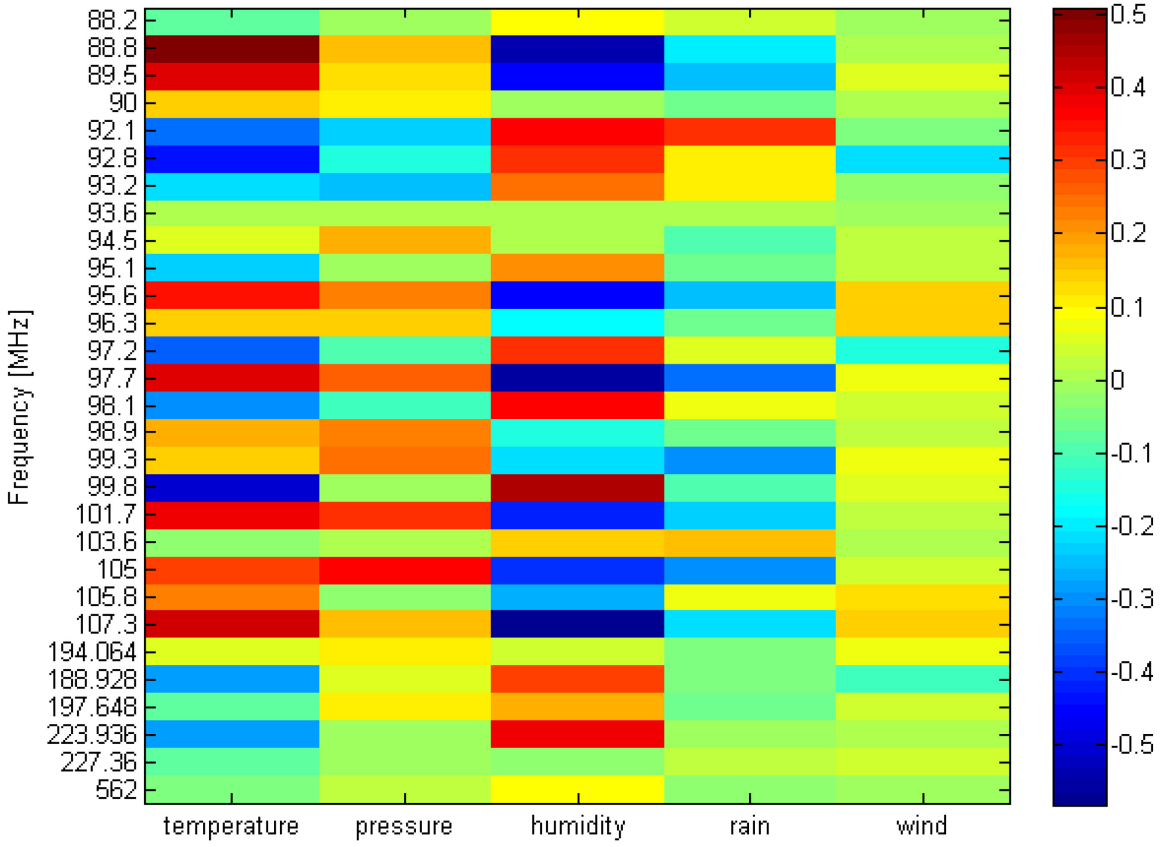

Figure 2-13: Correlation of Channel Data with Weather Data for the Measured Frequencies.

However, the correlation might not be the best tool to establish dependence between the weather data and the received power level. Especially in the case of the precipitation data, whose values are strictly positive, the subtraction of the mean might lead to a higher weight on the rain-free periods. For this reason the influence of the rain shall be investigated further.

2.2.5 Influence of Rain

In Figure 2-14, the FM-band data plot of Figure 2-3 is repeated, but this time including the precipitation data, which has been re-scaled to fit the bottom of the plot. It seems that whenever there is a precipitation spike, there is also some effect in most or at least some of the measured channels.

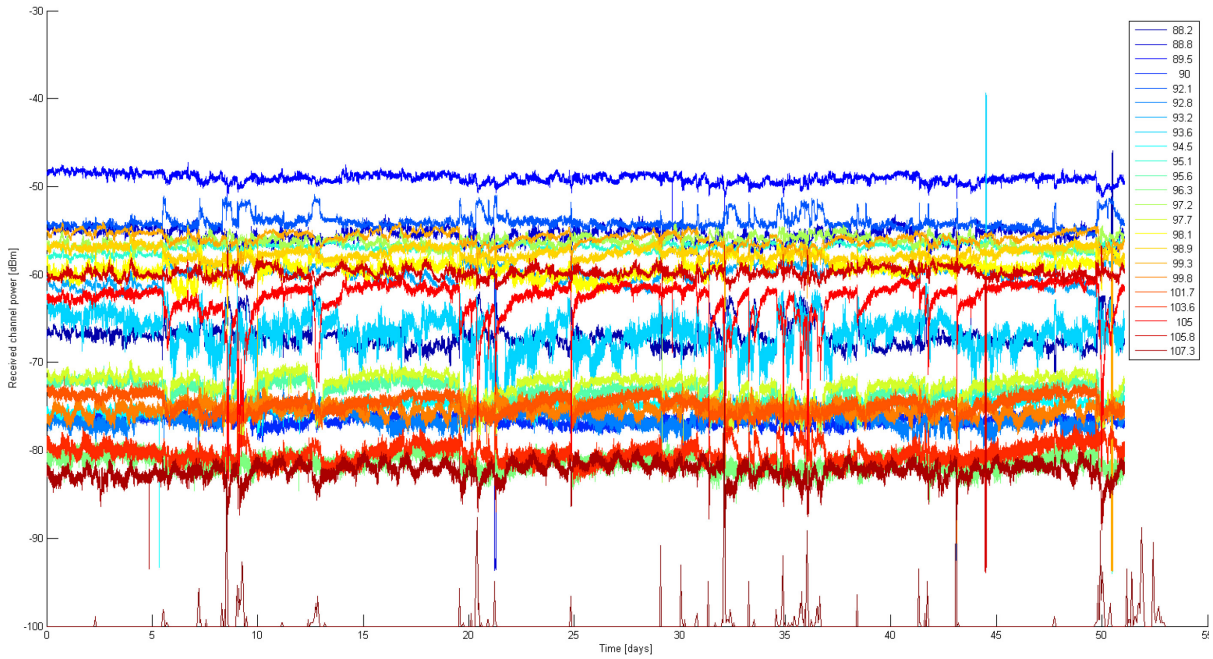

Figure 2-14: FM-Band Data for All Active Frequencies. The bottom red curve shows re-scaled precipitation data.

To investigate the difference between periods with and without rain, the following procedure is applied to the data. The mean of the received power is calculated over both periods of rain and dry periods separately. These two values are then compared by taking their ratio. The result is shown in Figure 2-15. It becomes clear that the difference can be positive or negative and take values between ±2 dB. There is no apparent dependence on the frequency.

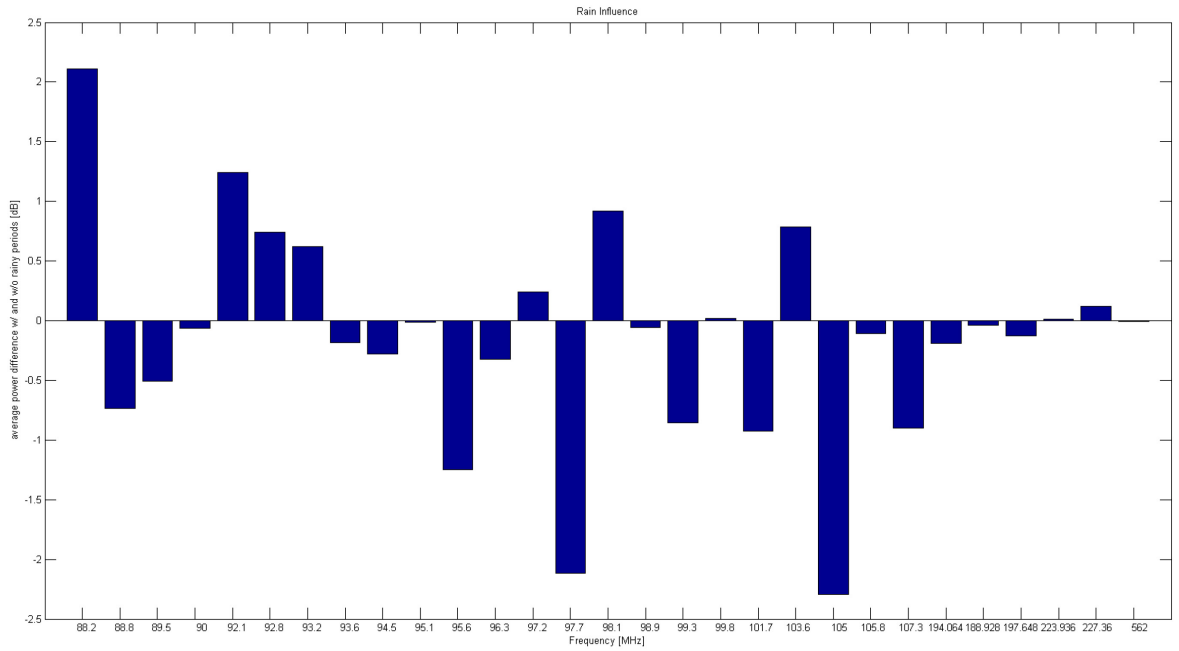

Figure 2-15: Ratio of Mean Received Power With and Without Rain for All Measured Frequencies.

Figure 2-16 shows the same plot but the channels have been ordered by the rain influence ratio. In the bottom plot of Figure 2-16, the average received power is shown with the same ordering of the channels. This shows that there is no obvious correlation between rain influence and received power. The hypothesis behind this was that rain causes the ground reflectivity to change, which in turn influences the multipath environment for the propagation channel. Since multipath might be more noticeable if the direct signal is weak, there might have been a correlation.

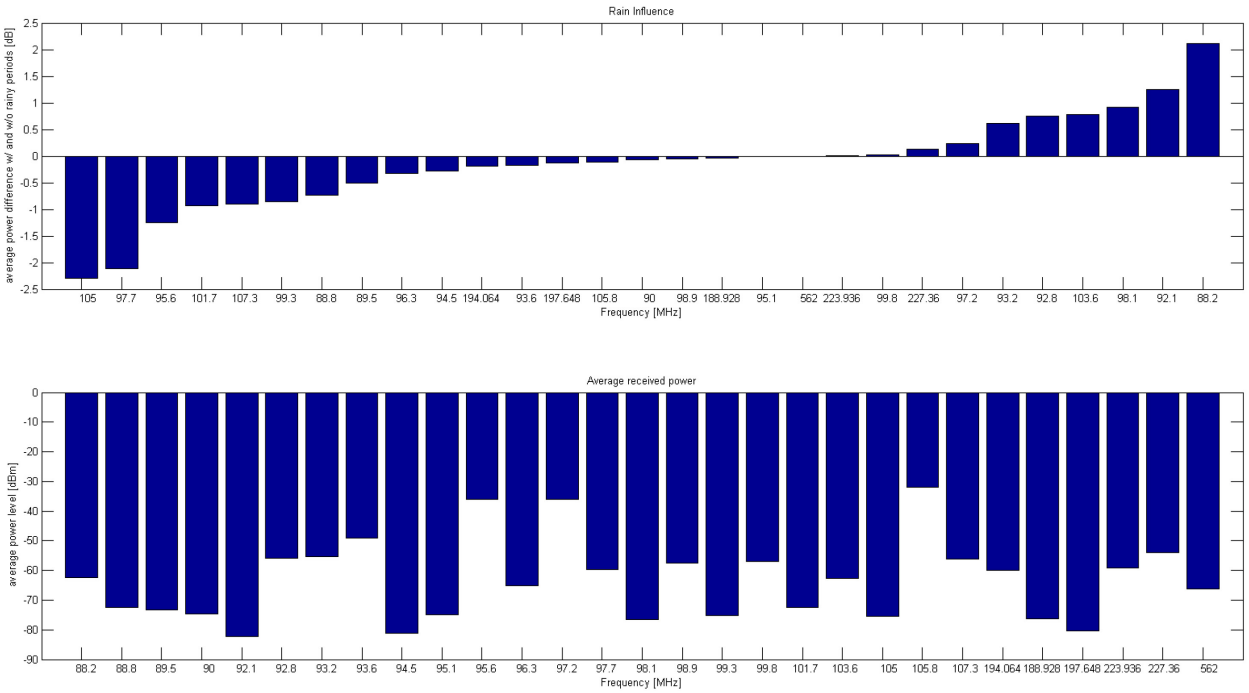

Figure 2-16: Channels Ordered by Rain Influence (Top) and Average Received Power (Bottom).

In order to check if there is a spatial dependence of the rain influence, we again look at the direction of arrival for the FM-band transmitters (calculated from the coordinates). Figure 2-17 shows the rain influence plotted against the DOA. If the DOA values are the same for two dots on the plot it can be assumed that they stem from the same transmitter tower (but are at a different frequency). This shows that, even if the transmitter and receiver sites are exactly the same, the rain influence can take all values.

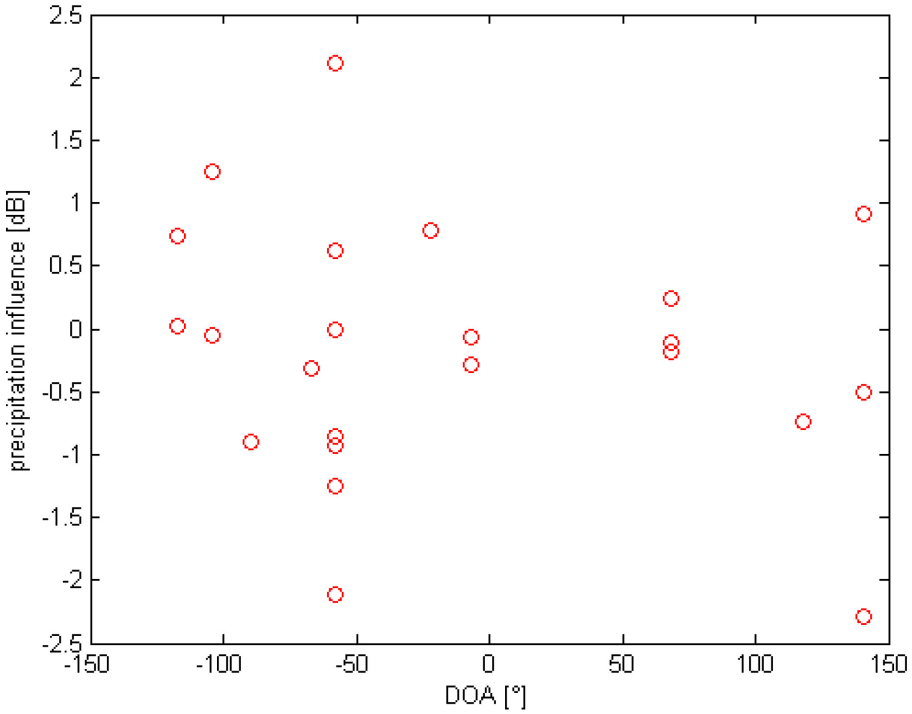

Figure 2-17: Precipitation Influence versus Direction of Arrival Calculated from the Coordinates of Receiver and Transmitter Sites.

In conclusion, there is not enough evidence to prove a significant influence of precipitation on the received power level.

2.3 CONCLUSION AND OUTLOOK

The collected data shows that received power of FM-band stations can fluctuate quite a bit. Even though the statistical analysis shows that this fluctuation is mostly contained within ±2 dB, there are still a great number of outliers. The strong correlation between the channels, on the other hand, makes clear that different transmitters of opportunity should not be considered independent from each other. There is a risk that a considerable number of stations will drop in their received power level at the same time over some periods.

There is no conclusive evidence – at least, based on the analyses performed – that precipitation or other weather features have a significant effect on the received power.

For future work the following aspects could be addressed:

- **Channel Impulse Response (CIR):** Instead of only measuring the received power level, the CIR could be measured. This would give an indication of the change of the multipath propagation environment. Especially in conjunction with weather data, the CIR could potentially reveal the influence of other factors, e.g., wet and dry ground.
- **Distributed measurement:** To help discriminate between true propagation effects and measurement artifacts, a distributed measurement with several measuring stations would be very valuable.
- **Development of a statistical measure for modelling influence on passive radar coverage and reliability:** It should be investigated how the shown statistical behavior of the received power can be accounted for when modelling passive radar coverage and reliability.

2.4 REFERENCES

[1] Public weather station in Thun, Switzerland (2016), www.thunerwetter.ch.

[2] Federal Office of Communications Switzerland, www.bakom.admin.ch.

Chapter 3 – TECHNIQUES IN ATMOSPHERIC MODELLING AND MEASUREMENT

3.1 INTRODUCTION AND POWER-BASED MODELLING

This chapter considers the power-based approach to performance prediction for Passive Radar (PR), and explores the path loss component in detail. In this approach, we cast the computational model as in Figure 3-1, and define the critical aspects of the problem to include:

a) The transmitters, described by generic, relevant characteristics;

b) The terrain, described by the altitude, in various resolutions;

c) The target, described by its dynamics and radar cross section; and

d) The receiver, described by its dynamics and sensitivity.

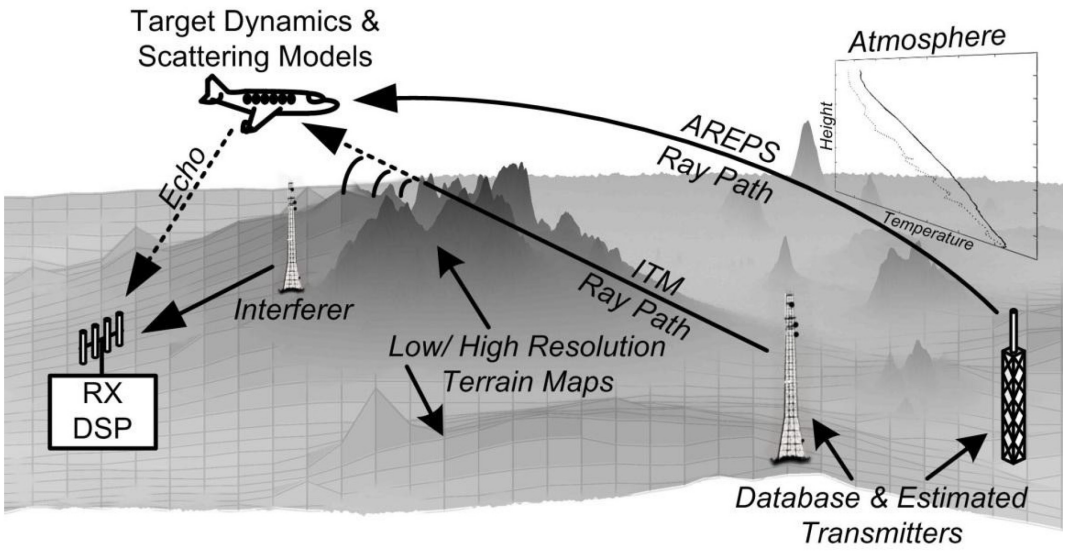

Figure 3-1: Basic Approach to Modeling the Passive Radar Power Budget.

Under this model, the signal to interference and noise ratio, *SINR*, of the radar echo is calculated as in equation (3-1), with constituent terms described as follows:

$$SINR = \frac{S_{\text{Illum}}\sigma_0 L_{\text{Echo}} FOM_{\text{RX}} \eta_{\text{sys}}}{\left(1 + \sum_{k=1}^{K} \hat{T}_k\right)} \tag{3-1}$$

- S_{Illum}: The illumination flux present on the target, in W·m^{-2}. This includes relevant properties of the illuminator (e.g., power and pattern) as well as the path (e.g., shadowing, atmospherics, and multipath).
- σ_0: The radar cross section of the target. This may be taken to be the particular RCS realized at a known aspect, or the mean RCS, which may be used as a starting point to models for fluctuating targets.
- L_{Echo}: The path loss of the return link from the target to the receiver; this should include the receiver's radiation pattern and account for terrain shadowing, atmospherics, and multipath.

- FOM_{RX}: The figure of merit of the receiver, including all properties such as its noise figure, coherent processing interval, maximum gain, and processing efficiencies.
- η_{sys}: Efficiencies of the radar link, such as spatial null losses as might be incurred in DPI suppression.
- $\hat{T}_k$: Normalized desensitisation terms that account for clutter, direct path, and cochannel interference.

Uncertainties in the characterization of any of the preceding terms will impart uncertainty into the SINR predicted for the passive radar. This cascades to uncertainty in the detection performance, described as P_{D} for a reference target. The detection uncertainties compound to uncertainty in the localization performance, given as P_{L} for achieving a desired error ellipse on the target's position solution, such as might be attained by non-coherent multistatic fusion of multiple detections.

Because of the importance in reducing, or at least characterizing, uncertainty in the SINR expression, the work reported in this chapter focused on modelling and characterizing the radio link loss in the passive radar problem. Solutions for the link loss are invoked several times in Ref. [1], including: the illumination and echo of the target, the illumination and echo of the clutter, and the direct path of in-band interferers including DPI and CoChannel Interference (CCI). We find, principally, that:

- Several accepted techniques exist to approach the problem of modelling terrestrial path loss; however, these techniques do not always agree to each other or to measurements;
- Given these differences, the absolute performance of a passive radar is currently both difficult to predict and expected to vary with changes in the troposphere;
- However, initial investigations indicate that these models provide relatively consistent guidance as to which design choices (e.g., illuminator selection) maximize performance; and
- Further, useful statistics of performance might still be viably generated based on these approaches, if the statistics of the propagation are known.

Section 3.2 of this chapter examines the problem of radio propagation from a modelling perspective, and presents results comparing Longley Rice (instantiated as the Irregular Terrain Model, ITM) to Split-Step Parabolic Equation methods (instantiated through AREPS, TEMPER, and PETOOL). Simulations are used to attempt to quantify the differences between the absolute predictions of these models, their influence on passive radar performance prediction, and their suggested influence on passive radar design choices. Next, Section 3.3 examines the problem via measurements, and presents results from several different campaigns intended to quantify the variability of the link losses and to assess the predictive accuracy of the models. Some areas for future work are discussed throughout and summarized in Section 3.4.

3.2 RADIO PROPAGATION MODELS

The essential element in assessing the radio link loss in passive radar performance prediction is the radio propagation model. Both statistical and electromagnetics-based approaches are known, and are complicated by factors such as multipath, varying land use, and the non-uniform (and temporally-varying) refraction of the atmosphere. Effects of the atmosphere are the focus of this work, which attempts to describe differences between results offered by selected models, and examine the importance of these differences in PR.

The influence of the atmosphere on radio waves has been noted since the advent of broadcast radio. VHF campaigns in the UK date back to 1932 and early measurements were used for frequency planning [1]. Ordinary atmospheric variability often manifests in the probability that a user will receive a satisfactory signal; extreme variations, termed anomalous propagation, can lead to detections at unusual ranges. Different propagation modes for terrestrial communications are described by Hitney [2], and relevant modes include free space loss, multipath, diffractive propagation, and tropospheric ducting. The study of these phenomena is of continued interest (e.g., Ref. [3]).

Among non-wave-based models, the ITU recommendation P.1812.2 [4] provides a method for calculating path-dependent propagation for terrestrial VHF and UHF links. In the absence of path-specific terrain data, P.1546.4 [5] gives statistical models considering factors such as terrain type, antenna heights, and frequency. The Longley-Rice model [6], and its implementation in the Irregular Terrain Model (ITM) [7], remain in use in the United States [8]. Despite some shortcomings [9] the LR method offers significant speed of analysis to the PR modelling problem.

One disadvantage of non-wave-based and statistical models is that they cannot describe situation-specific refractive conditions that might affect the PR. Historically, radar operators noted "unorthodox radar vision" [10] and other refractive phenomena soon after their development [2]. Atmospheric ducts alter target detection range [11] and surface clutter [12], and are of continued interest (e.g., Ref. [13]). Several popular refractive models, such as the AREPS [14], TEMPER) [15], and PETOOL [16] are based on the Split Step Fourier method applied to the Parabolic wave Equation (SSPE). While such models give similar solutions to each other and the ITM, the exact solutions vary.

Various link loss calculation methods have seen use in passive radar performance prediction. Both Hoyuela [17] and Inggs [18] used AREPS as a path loss prediction tool. The SET-164 report presented results from both ITU models and the APM (i.e., AREPS), and noted the difficulty in matching these results to clutter measurements.

3.2.1 Description of the Irregular Terrain Model

The ITM is a statistically-based model that estimates the effects of terrain (e.g., by knife edge and smooth earth diffraction) within a standard atmosphere. Statistical uncertainties are incorporated in model factors representing the reliability and confidence of the prediction [19]. The ITM FORTRAN implementation is described by Ref. [7] and a C++ implementation is also available from the NTIA [20]. As compared to wave-based models, the ITM is fast: a typical 36K-path profile for a single transmitter requires less than a second to calculate. Further optimization is possible, and Ref. [21] describes a GPU-accelerated ITM implementation calculating 256K profiles in hundreds of milliseconds.

Examples of radio flux maps created using ITM, intended for PR simulations, are shown in Figure 3-2. These illustrate the ability of the model to account for terrain shadowing (at left, representing a transmitter near Los Angeles, CA), as well as the importance of understanding the illuminator's radiation characteristics (at right, for a transmitter north of Miami, FL, using FCC data).

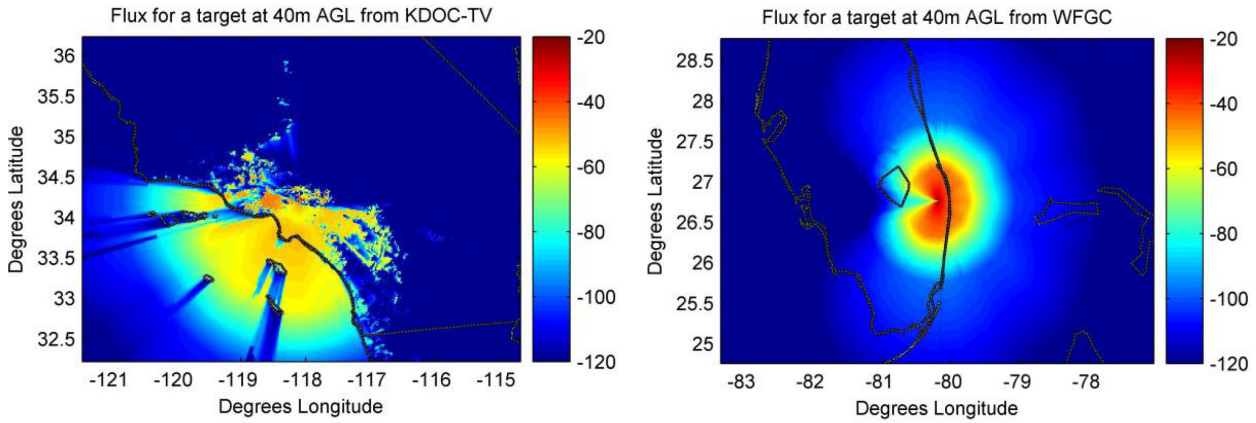

Figure 3-2: Example Radio Flux Maps Created Using ITM.

3.2.2 Description of SSPE Approaches

Situation-specific refractive effects, arising from atmospheric conditions, can be modeled using Split-Step Parabolic Equation (SSPE) techniques. These approach the problem from the perspective of 2D wave propagation and apply a location-dependent refractivity at each point in the simulation. For simplicity, the atmosphere is often assumed to be laterally homogenous: a condition likely to be violated, but noted by Hitney [2] to be "adequate most of the time". An example comparing the results of ITM to AREPS (one of the SSPE models examined here) is illustrated in Figure 3-3. These plots represent the predicted flux at various ranges and azimuths from the transmitter, taken at 5000 m AGL. Observations may include:

a) That the results from AREPS are generally more-complicated, owing to the refractive model; and

b) That AREPS is a hybrid model, and the transition to simpler calculations within 50 km is readily seen.

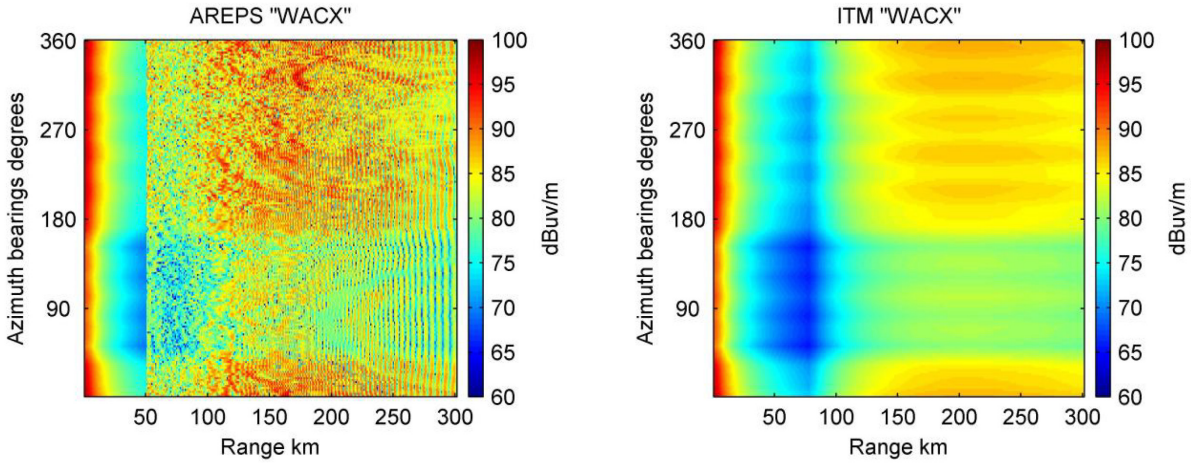

Figure 3-3: Example Comparing Range/Azimuth Slices Generated by the APM in AREPS (Left) to ITM (Right).

3.2.3 Comparison of Model Results (General Flux Expectations)

The criticality of the propagation prediction to PR motivated studies comparing the outputs of these radio propagation models, as well as of the behavior of the models under different conditions. An initial comparison between AREPS and ITM focused on examining the differences in the predicted illuminator fluxes. A region of 5° around Ocala, Florida was selected for this task, and the flux of all 1 MW transmitters in the region was evaluated using both models for a range out to 300 km for 181 different bearings.

The selection of the Ocala region was a deliberate effort to include only slowly-changing terrain. It included regions up to middle Georgia and Alabama, allowing moderate foothills while avoiding mountainous regions (e.g., the western USA). Early work had shown mountainous regions to result in very deep shadowing with AREPS (and large differences from ITM), and it was desired to exclude these from the analysis.

Flux profiles from the transmitters were aggregated and concatenated along ϕ (azimuth) into $S_{\text{region}}(x, \phi)$ (range/azimuth). These data were sorted along ϕ, such that the result represented the distribution of fluxes observed at each range. The top plots in Figure 3-4 include curves from both AREPS and ITM, illustrating the 90% and 10% quantiles of flux as a function of range, for profiles at 600 m AGL and 5000 m AGL.

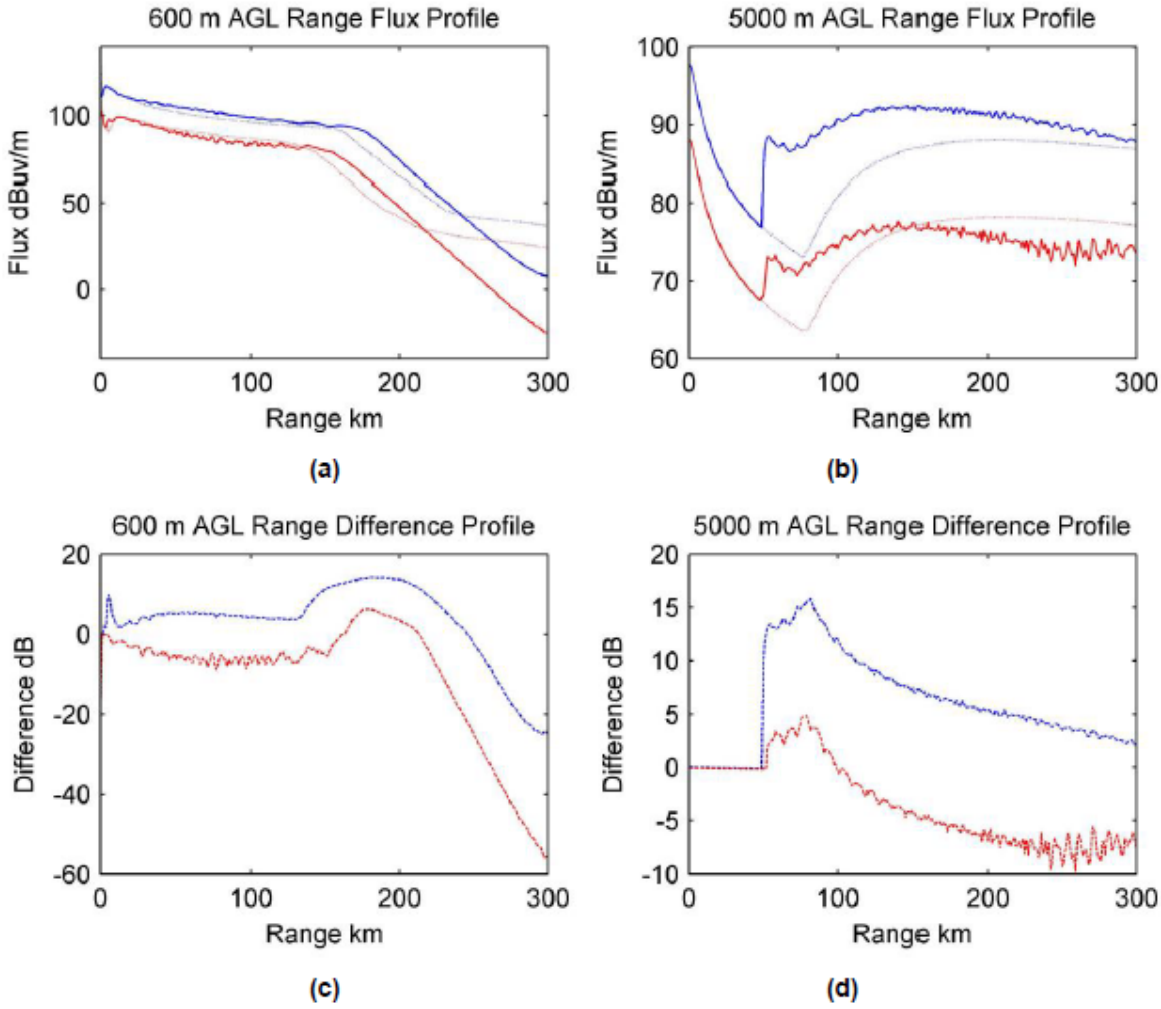

Figure 3-4: (a) and (b) Represent Aggregated 90% (Blue) and 10% (Red) Confidence Fluxes (dB μvm-1) for AREPS (Dark) and ITM (Light) in the Ocala, FL Region; (c) and (d) Represent 90% and 10% Confidence Curves of the Difference (dB) of the Propagation Loss Models, Where Positive Values Represent Higher Flux Predicted by AREPS.

The bottom plots in Figure 3-4 were calculated by performing a similar aggregation, but by computing the difference $L_{\mathrm{APM}}(x,\phi) - L_{\mathrm{ITM}}(x,\phi)$ prior to sorting. This resulted in range-dependent statistics of the point-by-point dB-differences between the propagation loss models. The curves in each plot represent the 10% and 90% confidence bounds on the difference at each range. Here, values greater than 0 dB in represent situations in which AREPS predicts a stronger flux than ITM.

The 600 m and 5,000 m plots each show regions of differing agreement between the propagation loss models. At 600 m, the models agree to within about 10 dB in the line of sight region. Within the diffractive region, AREPS predicts generally stronger fluxes; however the situation is reversed in the troposcatter region, in which the ITM predicts fluxes up to 50 dB stronger than AREPS.

Examining Figure 3-4 further, at 5,000 m AGL, ranges within 50 km of the transmitter indicate very good agreement between AREPS and ITM. This area corresponds to the ray optics region in AREPS where geometrical optics is used. The largest variations occur in the extended optics and parabolic equation regions, where AREPS implements PE mode. Solutions in the parabolic equation region are scenario-specific, and approximated neither by simple ray optics nor by statistical estimates like ITM [22].

3.2.4 Additional SSPE Models

Not all SSPE models provide identical results, and two additional SSPE-based models were examined in this work. The first is the Tropospheric Electromagnetic Parabolic Equation Routine (TEMPER), a product of The Johns Hopkins University Applied Physics Laboratory. It is similar in concept to AREPS; Brookner provides descriptions of both tools and their applicability to radar [23]. The second is the parabolic equation software tool (PETOOL), which was developed by Ozgun [16]. As compared to AREPS and TEMPER, PETOOL has the advantage of being implemented solely in MATLAB, potentially easing integration into research models for passive radar.

Figure 3-5 illustrates one example of the flux predicted by the four models (ITM and the SSPE models) for a DTV transmitter in Florida. Although each model is identically-initialized to the greatest extent possible, multipath-related fading is different to about the 10 dB level (especially in the 50 – 100 km range). General trends and long-range multipath ringing are consistent, however, among the models. With the exception of the diffractive region at long ranges, the SSPE models appear to follow the general predictions of ITM.

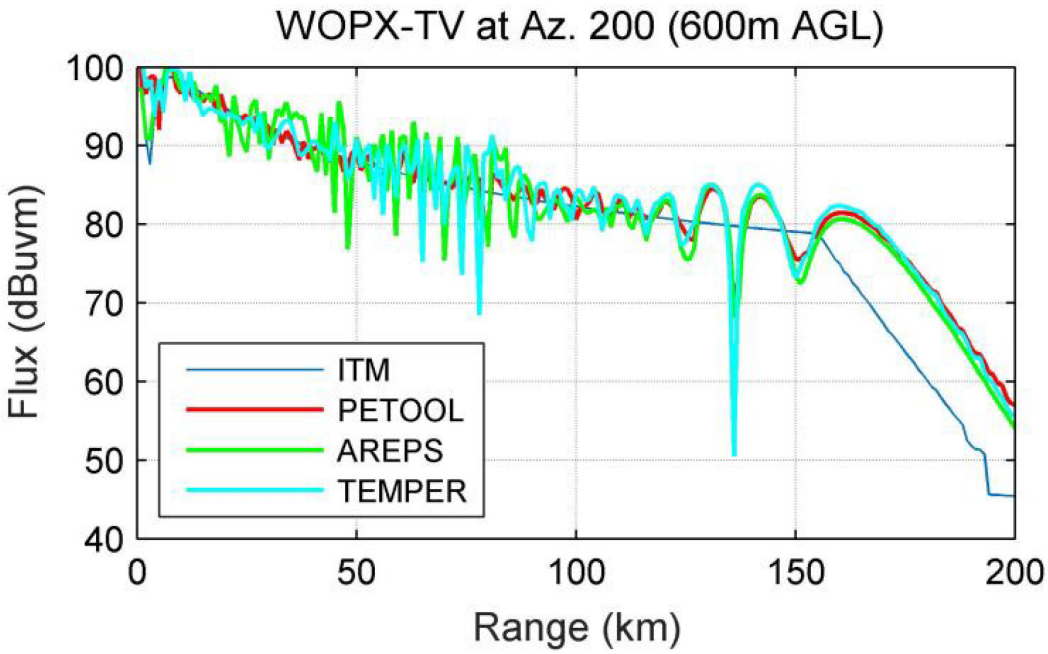

Figure 3-5: Illumination for the DTV Station WOPX in Florida, Taken at 600 m AGL for Three Different SSPE Models as well as ITM. Includes antenna pattern effects. Each model is provided the same initialization.

From the perspective of the passive radar, the effects illustrated in Figure 3-5 result in uncertainty in illumination and echo path losses (both for the target and clutter), as well as differences in the levels of interfering signals (e.g., DPI and CCI). These differences will manifest as uncertainties in the predicted target SINR, detection probability, and ultimately in the geographic coverage of a PR system.

An example illustrated in Figure 3-6 shows the predicted PR coverage using three different propagation models for an airborne system, with both the receiver and targets at 600 m AGL. The color scale represents the Cramer-Rao lower bound on 2D target localization. This bound is calculated presuming the use of non-coherent multilateration of echoes from multiple DTV illuminators (indicated as cyan 'x') and a single PR receiver (the red '+'). The CRLB is found as $\sigma^2 = \mathrm{tr}\{\mathbf{J}^{-1}\}$, where $\mathbf{J} = \mathbf{H}^T\mathbf{Q}^{-1}\mathbf{H}$, and is composed of elements representing the illuminator-target-receiver geometry for each successful echo, defined as having an echo above 13 dB SNR and a direct path above 20 dB SNR. The geometric terms are given as:

$$\mathbf{H}_{nk} = \frac{-\left(\boldsymbol{\theta}_{nk}^{(TX)} - \boldsymbol{\theta}_{nk}^{P}\right)}{\left|\mathbf{R}_{n}^{(TX,P)}\right|} + \frac{-\left(\boldsymbol{\theta}_{nk}^{(RX)} - \boldsymbol{\theta}_{nk}^{P}\right)}{\left|\mathbf{R}_{n}^{(RX,P)}\right|} (\text{range}), \text{and} \tag{3-2}$$

$$\mathbf{H}_{n}^{(Az)} = \frac{1}{\left|\mathbf{R}_{n}^{(RX,P)}\right| \sin(\varphi_{3dB})} \hat{\boldsymbol{\varphi}}^{(RX)} (\text{azimuth}). \tag{3-3}$$

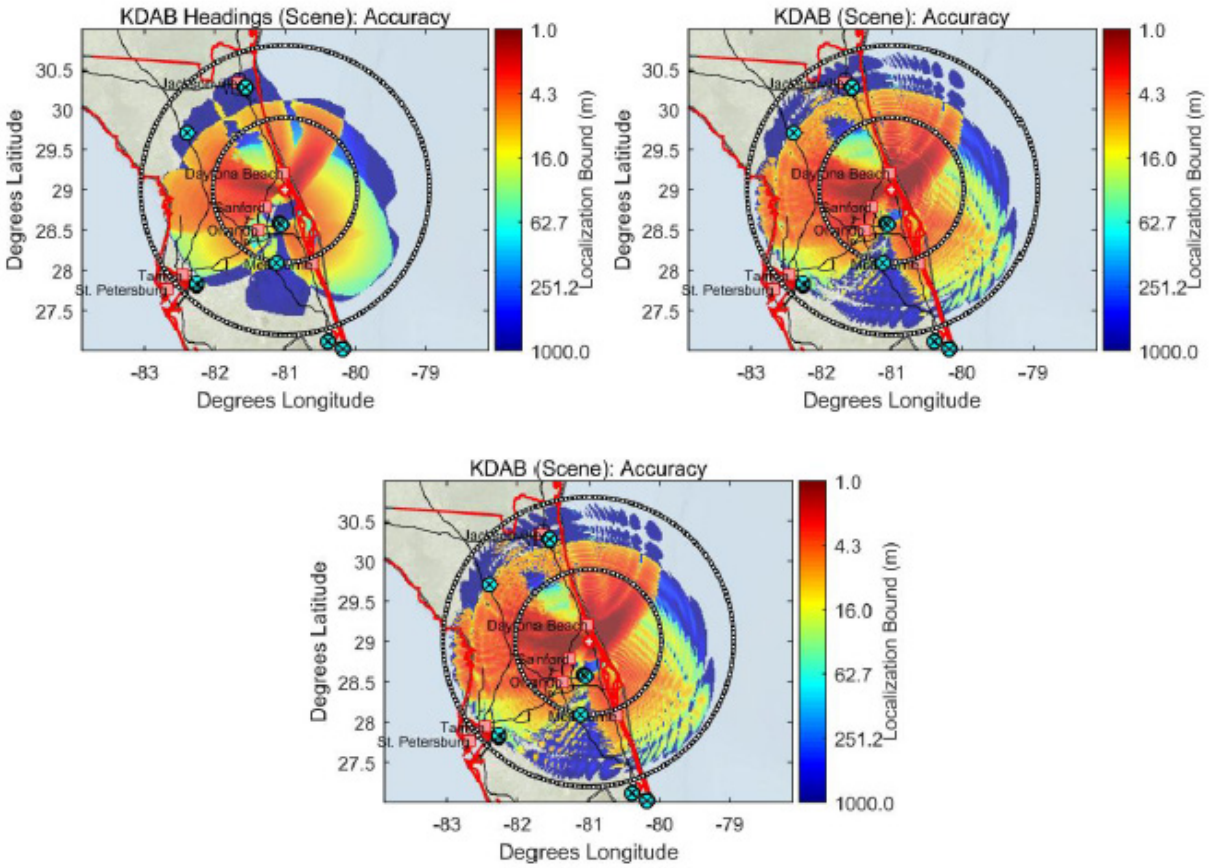

Figure 3-6: PR Coverage Predictions Near Daytona Beach, FL, Comparing ITM (Top Left), PETOOL (Top Right), and TEMPER (Bottom).

The noise terms are given as:

$$(\mathbf{Q}^{-1})_{jj} = \frac{2B^2 SNR}{c^2} \text{ (range) and } (\mathbf{Q}^{-1})_{jj} = 2SNR \text{ (azimuth)} \tag{3-4}$$

3.2.5 Performance Over Frequency

Despite their computational accuracy, one weakness of the SSPE models is that they are monochromatic; that is, they consider only a single frequency within the analysis. This property leads to the multipath ringing in range, and later to the scalloping observed in the 2D coverage maps. For wideband signals, however, the monochromatic result might not accurately represent the observed path loss. Kulpa [24] showed that the

impact of multipath in passive radar depends on the relationship of the excess delay, $\tau = d/c$, to the waveform's bistatic range resolution, ΔR. Whereas the regime of small delays $d \ll \Delta R$ will exhibit typical multipath lobes, larger delays $d \geq \Delta R$ manifest multipath as a true-time delay. Garry's experimental data showed the manifestation of multipath illumination at excess time delays [25].

One way to approach the problem of modeling wideband signals is to invoke the SSPE models at many different frequencies f across the signal's bandwidth. The average of the results describes the mean flux $\bar{S}$ present at the point of interest r as:

$$\bar{S}(r) = \frac{1}{N} \sum_{f\,min}^{f_{max}} S(r, f). \tag{3-5}$$

The number of N_f points should be sufficient to resolve the longest multipath in the frequency domain, such that the frequency step is approximated by $\Delta f \approx c/\Delta \mathrm{R}$. While this technique is computationally-simple and captures the total power arriving at each point (by Parseval's theorem), it is computationally-intensive, and multiplies the already-significant cost of using SSPE models over wide areas. For example, modelling a 6 MHz illuminator using the 60 kHz step size in this work requires 100 discrete calls to the underlying PE model.

It is noted that a possible extension of (3-5) is to consider complex Fourier analysis instead of power-based frequency averaging. Although not pursued here, such an approach might allow the direct path propagation component to be separated from the multipath; this might help PR performance prediction simulations better identify both the on-target flux as well as predict the presence of the multipath ghosts. A limited exploration of complex analysis of SSPE outputs, examining atmospheric evolution, is presented later in this chapter.

Figure 3-7 contains results of applying multi-frequency averaging to the same DTV illuminator used in Figure 3-5. This illuminator (WOPX) is located in Florida, which has characteristically-flat terrain. The curves represent the fluxes at 600 m AGL along a single radial taken at an azimuth of 200° from the transmitter. These curves were rendered in both TEMPER and PETOOL and compare 3 different signal bandwidths to both the narrow-band predictions and the reference prediction of ITM. In each case, the curves are offset by 5 dB from each other for clarity.

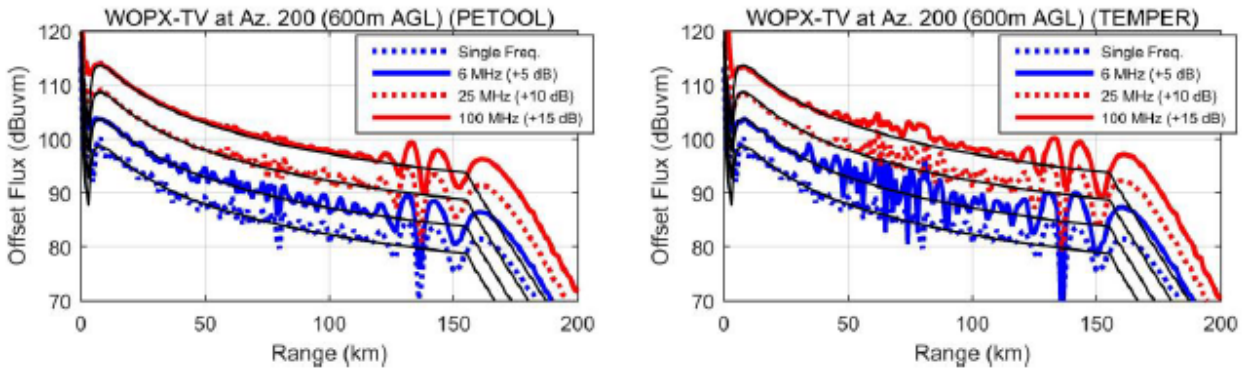

Figure 3-7: Illumination vs. Range for the WOPX Illuminator Using Frequency Averaging. The curves at different bandwidths are offset for clarity, and each is superimposed with the ITM result (black).

The smoothing in Figure 3-7, which extends in range with higher bandwidths, is the expected result when the lobes are due to multipath. The convergence of these models toward the ITM result might support the use of

ITM for general simulations that do not require scenario-specific refraction. The increased variation seen in the 6 MHz TEMPER data is noted without present explanation and should be examined further, as each model and case is initialized with similar inputs. The multi-frequency models use 60 kHz steps.

A 2D result of the multi-frequency averaging is compared to a monochromatic prediction in Figure 3-8. This uses the same transmitter as Figure 3-7, but is here predicted at 3000 m AGL to emphasize the transition from large-time multipath to short-time multipath. Here, the 5.38 MHz bandwidth UHF DTV transmitter was simulated over 27 frequency steps. The effect of smoothing is most-readily seen to the south and east of the transmitter, where extreme values predicted by the monochromatic model are deemphasized.

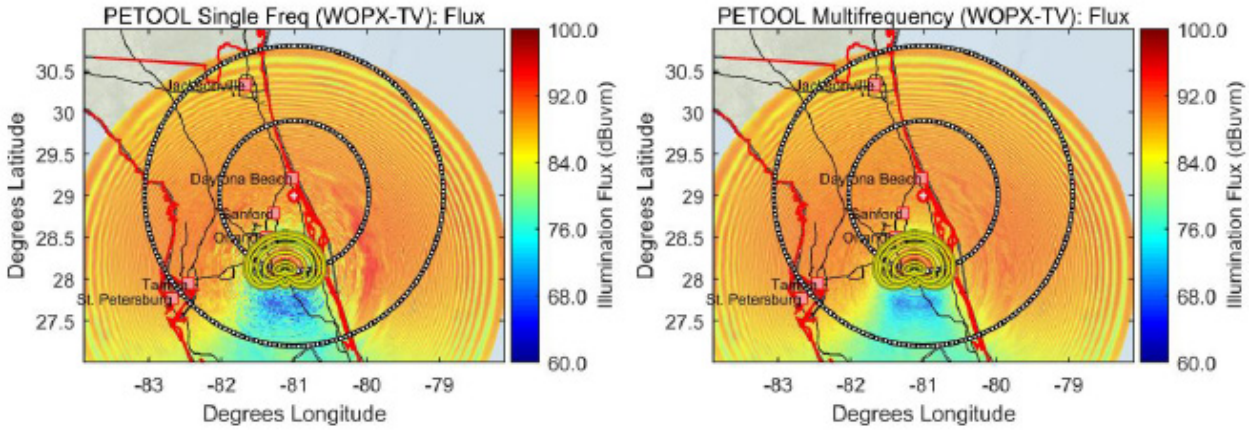

Figure 3-8: 2D Flux Comparison of the Multifrequency Models, Using PETOOL.

The effect of modelling the signal bandwidth was next observed for the passive radar's multilateration (target localization) performance. This simulation used targets at 3000 m AGL, a receiver at 1000 m AGL, and assumed that both were traveling east at 80 m/s. These altitudes allowed significant multipath lengths as compared to the DTV signal's range resolution. The receiver has a sensitivity similar to an array of four UHF dipoles with a 100 ms CPI and requires 13 dB SNR to detect the 1 m^2 targets. This simulation merges the results of smoothing of each constituent link and the overall effect on the PR.

Figure 3-9 contains the results of this multi-frequency analysis and suggests several observations. First, the multi-frequency model exhibits a smoothing in performance that is consistent with Figure 3-8 and the smoothing of the underlying links. Second, although PETOOL results predict a much farther useful range for the radar, this result should be taken with caution. Examination of the data shows that predicted SNRs are near the model's 13 dB detection threshold in this disputed region; multipath ringing might be responsible for raising the predicted SNR just above the threshold in the PE data. This model used only binary detection statistics, and further analyses should be conducted using Swerling target models.

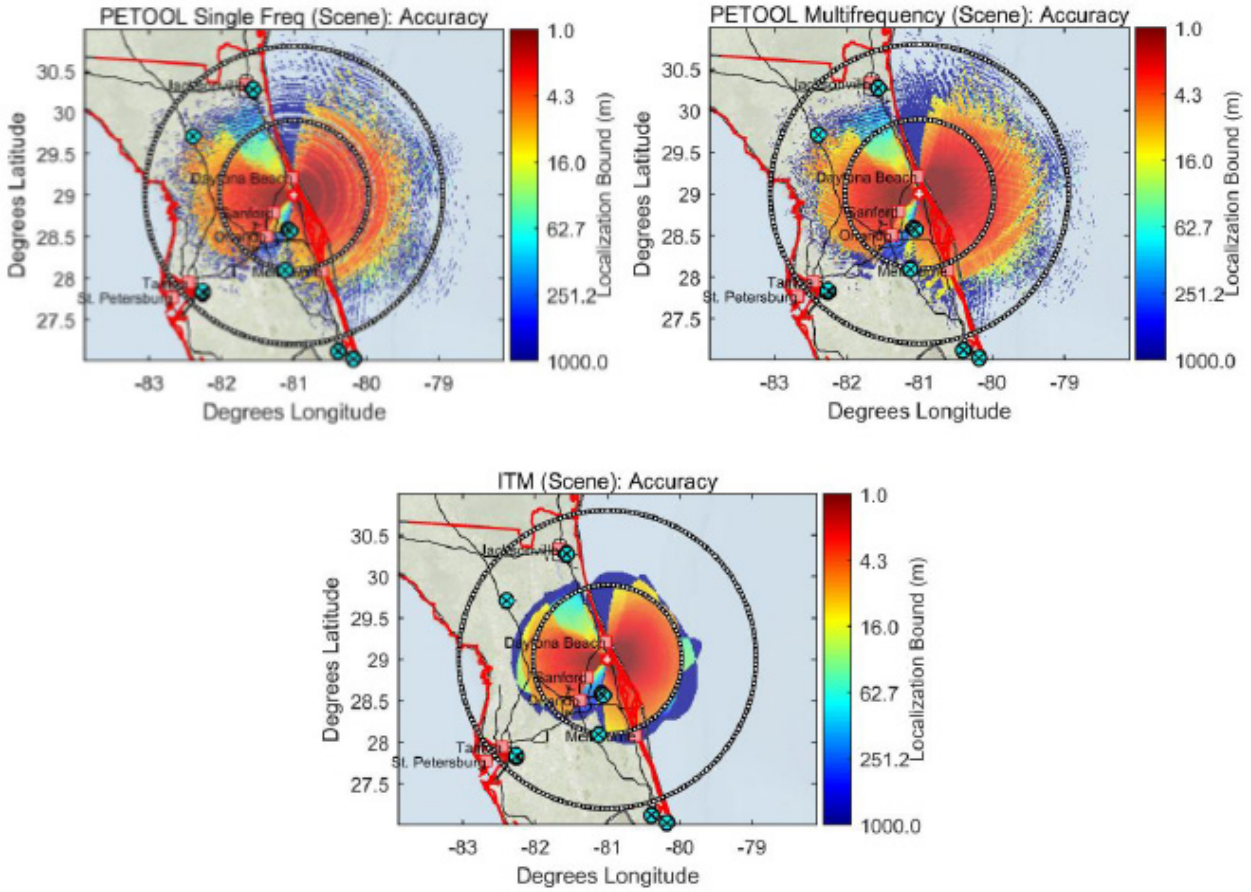

Figure 3-9: Passive Radar Localization Performance Predictions Comparing the PETOOL Monochromatic and Multifrequency Results (Top) to ITM (Bottom). The receiver is at the center of the image at 1000 m AGL.

3.2.6 Performance Over Ducting Conditions

Whereas the preceding work examined differences across models using a standard atmosphere, the principal advantage offered by refractive models is their ability to incorporate a refractivity profile in the simulation. This allows results to apply to specific conditions, and offers the opportunity to consider the variation in performance across different such conditions. This profile is described by the modified refractivity $M = (n - 1 + z/a_e) \times 10^6$, which relates the refractive index n to the height z and earth radius a_e. This quantity is convenient for refractive modeling, as negative gradients are associated with ducts or other trapping [26].

Global historical refractivity data can be obtained from the US National Oceanic and Atmospheric Administration (NOAA) through its radiosonde archives in the IGRA [27]. The present work examined data from stations in Jacksonville, FL (72206) and Wilmington, OH (72426). Refractivity profiles were applied to simulations using the DTV channels WACX (for Florida) and WSTR (for Ohio), which were selected as typical stations for these regions. The profiles were assumed to be laterally homogenous. In each case, PETOOL was invoked to create range-height profiles of the predicted flux for 1000 soundings (comprising about twice-daily soundings from the most-recent data). Selected results comparing high-ducting and low-ducting cases for each location are shown in Figure 3-10.

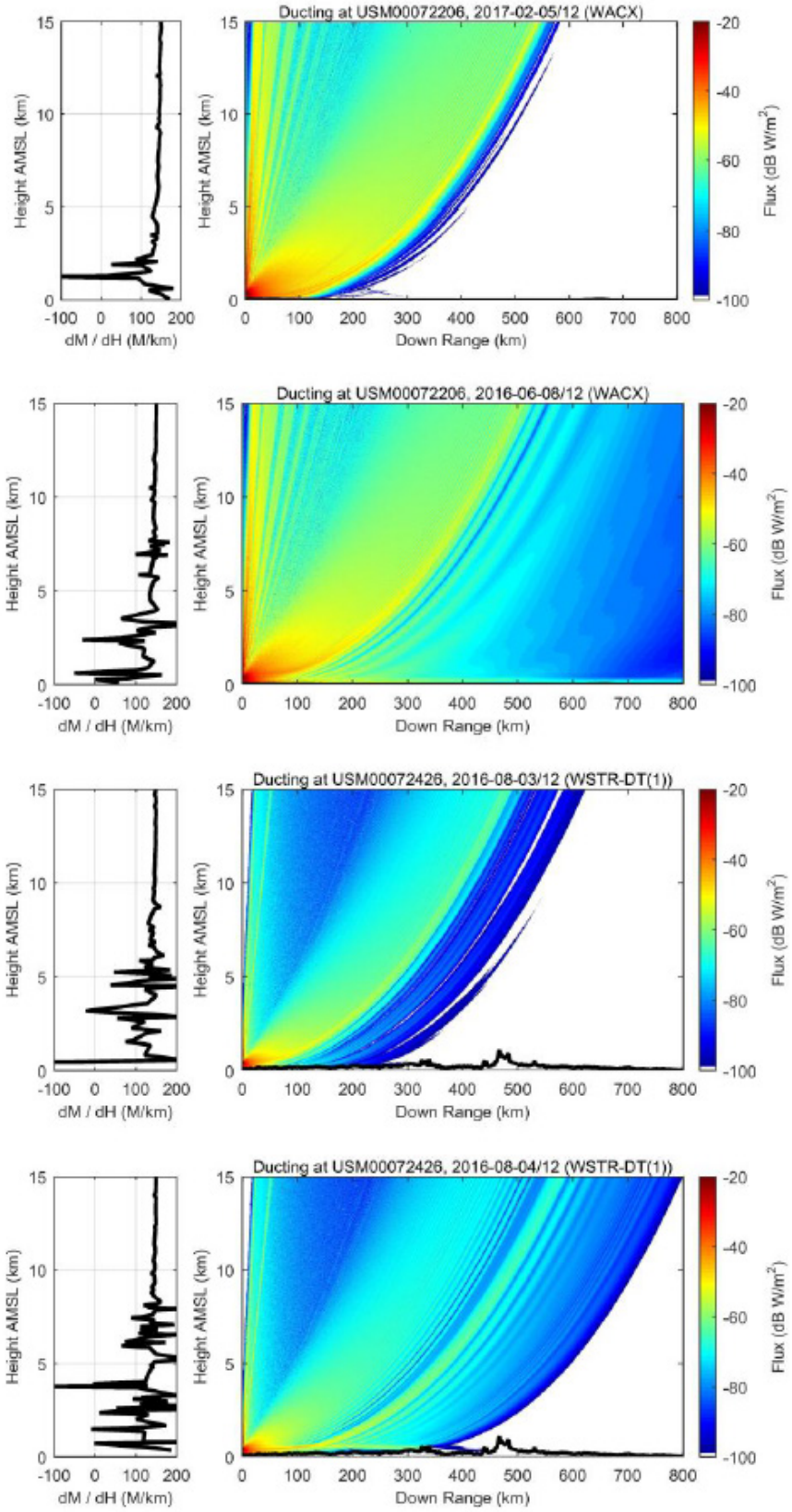

Figure 3-10: Selected Range-Height Slices and Accompanying Radiosonde Profiles. From top to bottom, Florida with low and high trapping, and Ohio with low and high trapping.

Beyond the variation in predicted signal strength, a key result is the observation that high-ducting cases might provide flux exceeding -70 dBW/m^2 Beyond the traditional Line Of Sight (BLOS) of the illuminator; this might enable target detection using sufficiently-sensitive receivers. It is not clear whether this high-altitude BLOS flux is observed in reality; empirical studies of this effect should be pursued in future work.

Results from sorting the ducting data into quantiles are illustrated in Figure 3-11. These are thresholded as the values exhibited the worst 10% and best 10% (shown as 90%) of the time. These plots illustrate that the importance of the atmosphere on the illumination flux is not limited to rare events. Further, although not clear in Figure 3-10, Figure 3-11 shows that the variability also affects the flux at points within the direct line of sight of the illuminator (e.g., the high altitudes within 200 km). The variability predicted here leads to useful flux beyond the radar's line of sight in at least the best 10% of the time, in locations where it would be excluded in at least the worst 10% of time.

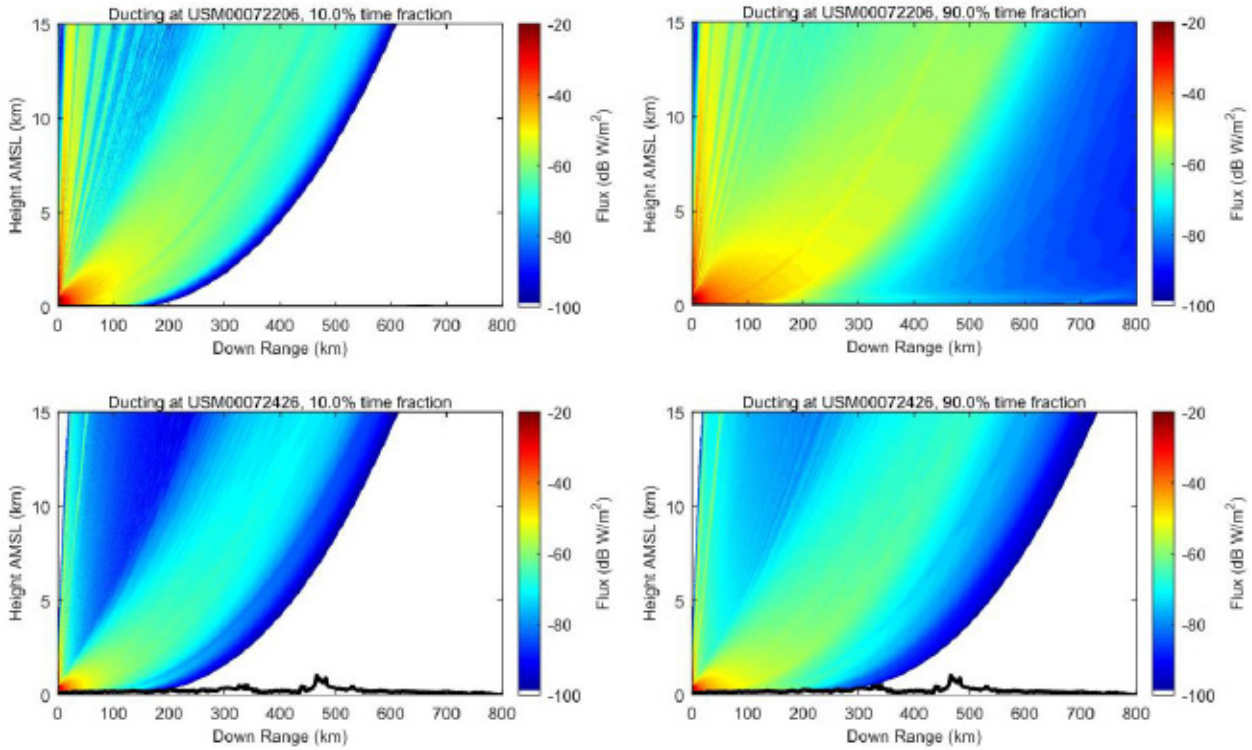

Figure 3-11: Predicted Flux Quantiles Over 1000 Ducting Profiles for Florida (Top) and Ohio (Bottom). Data are thresholded at the 10% quantile (left) and the 90% quantile (right).

The final point highlights that the ultimate range of a passive radar is expected to depend on the state of the atmosphere. While surface ducting is a known phenomenon in active monostatic radars, a key difference for passive radars is that a PR might be able to exploit (or avoid) a duct by selecting the appropriate illuminator. Future work should further study this problem, including:

a) How these predictions change when the condition of lateral homogeneity is no longer assumed; and

b) How PRs could effectively interact with the dynamic atmospheric conditions.

A final comparison examined the statistical variance of the illumination arising from these profiles, and compared the result with that predicted by ITM's internal models. Values for the PETOOL data were obtained by finding the standard deviation of the flux at each pixel; values for ITM were determined by fitting a Gaussian PDF to ITM data calculated using two different values of the *reliability* parameter (one of

the two confidence settings provided in the model), which Hufford [19] describes as "concerned with a fraction of time." The results in Figure 3-12 show that ITM provides a reasonable approximation of low variability within the line of sight, and somewhat higher variability near the radio horizon, but fails to capture the exceptionally high values observed beyond the radio horizon. This is not surprising, as ITM was developed for broadcast purposes, but nevertheless points to an area of future work.

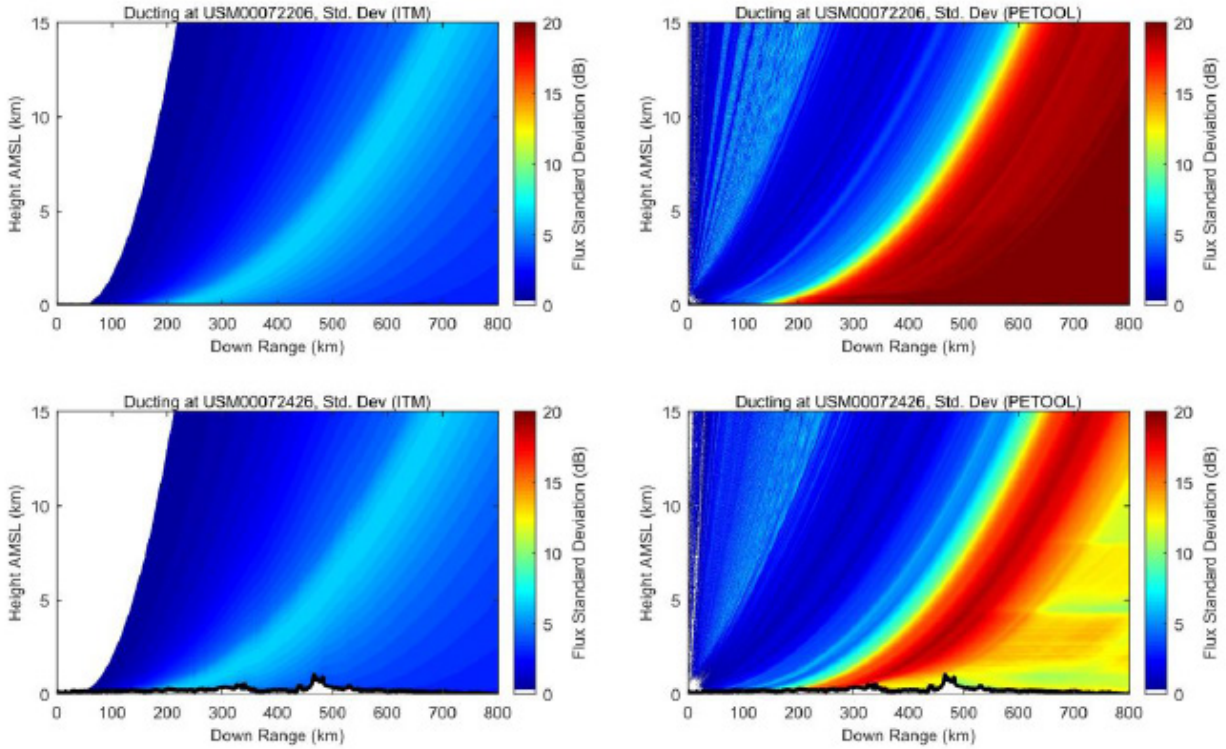

Figure 3-12: Predicted Standard Deviation of the Illumination Flux for Florida (Top) and Ohio (Bottom) as Predicted by ITM's Internal Model (Left) and PETOOL's Analysis of 1000 Radiosonde Profiles (Right).

3.2.7 Influence of Variation on Passive Radar Coverage

The ultimate influence of the atmospheric variations on the performance of a passive radar was evaluated by extending the preceding analysis to a complete PR coverage simulation. The performance of the radar is characterized as its coverage area, and the Prelude simulator is used to prepare figures in scenarios similar to Figure 3-6. Here, the target and receiver altitudes were lowered to at 600 m AGL to reduce simulation times, but the other attributes of the simulation were retained (velocities east at 80 m/s, 100 ms CPI, receiver having 4 UHF dipoles and requiring 13 dB SNR to detect the 1 m^2 targets). Non-fluctuating targets are presumed.

This work used the monochromatic PETOOL model, which was prepared using 1000 different radiosonde profiles from the IGRA. These represent the Jacksonville region for twice-daily profiles beginning June 1, 2016. The atmosphere was laterally homogenous; although this assumption should be re-examined further in future work. The simulator was invoked for the 1000 separate scenarios and the results examined.

Figure 3-13 shows selected results of this work. The predicted radar coverage for two (extreme) realizations of the atmosphere is illustrated in the top two panels, with the relevant refractivity gradients inset. These show the possible difference in coverage from changes in the atmosphere alone. The final (bottom) panel is formed by combining the 1000 different realizations into a single figure, and here represents the probability of target localization P_L, where the atmosphere is taken to be the random variable, and successful

localization is defined as having a multistatic CRLB better than 100 m. Note that this, by necessity, incorporates the P_D of all of the constituent passive radar links within the scene.

$$P_L = \frac{1}{1000}\sum_{k=1}^{1000} \boldsymbol{\sigma}_{k,LLA} \leq 100\text{m} \tag{3-6}$$

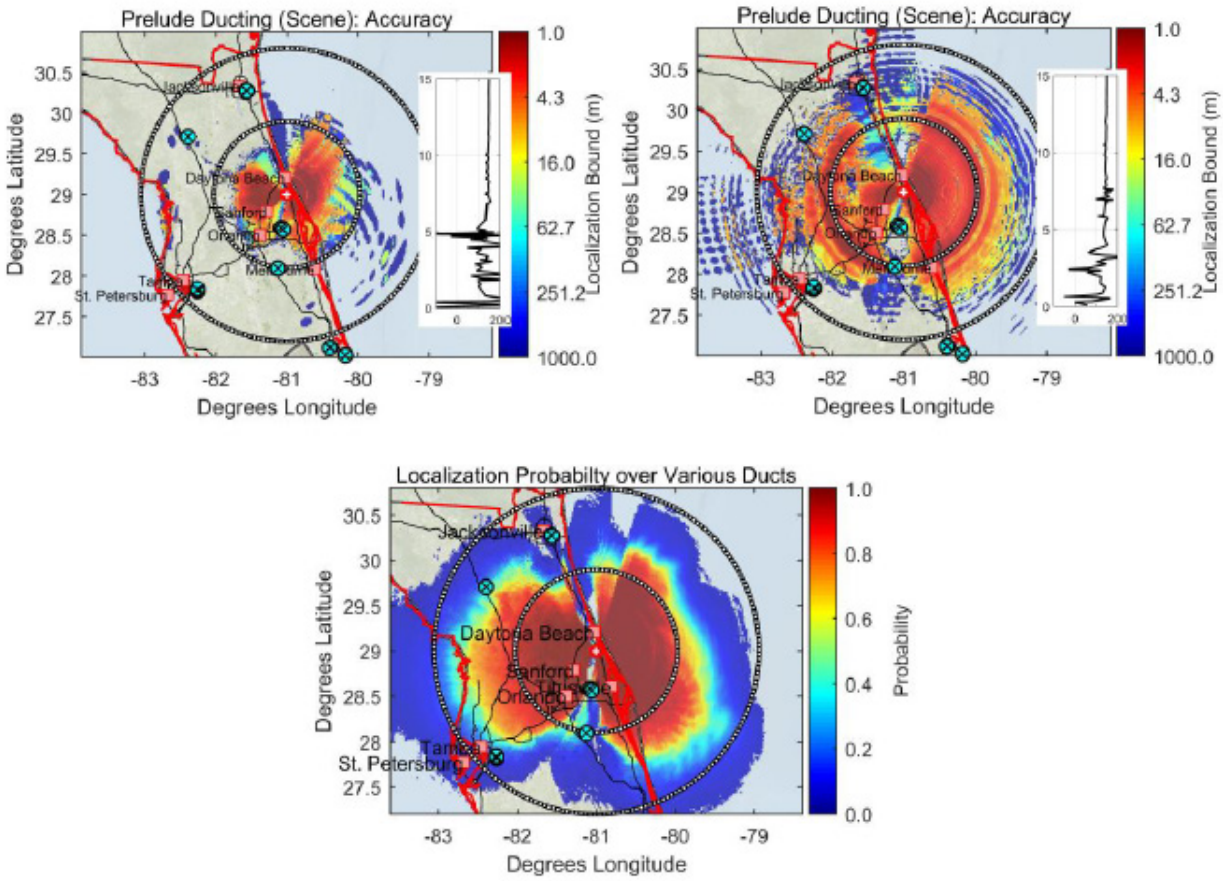

Figure 3-13: Predicted Passive Radar Coverage Variations When Using Different Atmospheres (Station 72206). Top left: 2017/09/07; Top right: 2016/06/08. Insets indicate dM/dH vs. altitude. At bottom, coverage probability.

3.2.8 Influence of Models on Illuminator Selection: AREPS vs. ITM

The two key conclusions of the preceding results are that:

a) There are differences between the passive radar coverage predicted using different propagation models; and

b) Even with the same model, differences will exist over the evolution of the atmosphere.

If the designer accepts that performance prediction models cannot predict the absolute performance of the radar a priori (either because of the unknown factors, or unknowable factors), then the performance prediction problem can be recast as a performance maximization problem.

In these conditions, the goal is to design a passive radar such that its performance is maximized irrespective of the variations in the unknown factors. This work uses illuminator selection as the design choice, in which it is presumed that the receiver comprises a resource-limited system capable of ingesting only a limited number of available transmitters. The choice of which transmitters to sample is optimized to maximize the coverage area of the radar.

The first analysis examined this optimization problem in the context of the question of which path loss model is selected; in this case, comparing AREPS and ITM. A total of 70 different regions were simulated with each model, in a configuration similar to the previous analysis, and a greedy optimizer was applied to each result to maximize the number of pixels (target locations) satisfying a CRLB $\sigma_{\mathrm{LLA}} \leq 1000$ m (termed here as lateral localization accuracy, LLA). The optimizer was configured to select varying numbers of illuminators, $3 \leq \mathrm{M} \leq 9$, representing passive radars of varying complexities.

Given the discrepancy of absolute performance between the two models, a useful high-level metric is to quantify how the coverage predicted by each model changes based on which illuminators are used, and whether an illuminator selection that is optimal for one model (e.g., for ITM) is optimal for the other (e.g., AREPS). Such a match would indicate that the models agree at least on a strategy for how to best maximize the radar performance, even if they cannot agree on what the value of that performance ultimately is.

This problem is evaluated by defining a general function $f_{\mathrm{PR}}(\mathbf{M})$ that generates the score (coverage) based on the transmitters $\mathbf{M}$ using the propagator PR. For example, $f_{\mathrm{ITM}}(\mathbf{M}_{\mathrm{ITM}})$ (termed the *self-selection* score) describes computing a score using the ITM propagator, using the set of transmitters selected by optimization of ITM results. In contrast, $f_{\mathrm{AREPS}}(\mathbf{M}_{\mathrm{ITM}})$ (termed the *cross-selection* score) describes computing a score using the AREPS propagator, using the set of transmitters selected by ITM. Similar terms are defined as $f_{\mathrm{ITM}}(\mathbf{M}_{\mathrm{AREPS}})$ and $f_{\mathrm{AREPS}}(\mathbf{M}_{\mathrm{AREPS}})$. Under these definitions, we define the two metrics:

$$\left|\frac{f_{\mathrm{ITM}}(\mathbf{M}_{\mathrm{AREPS}})}{f_{\mathrm{ITM}}(\mathbf{M}_{\mathrm{ITM}})} - 1\right| \text{ and } \left|\frac{f_{\mathrm{AREPS}}(\mathbf{M}_{\mathrm{ITM}})}{f_{\mathrm{AREPS}}(\mathbf{M}_{\mathrm{AREPS}})} - 1\right| \tag{3-7}$$

to describe the error between the self-selection and cross-selection results. Data over the 70 analyzed regions were analyzed to identify statistical bounds on thresholded errors of this metric. Curves showing the results for thresholds at 0%, 5%, 10%, and 20% of errors are illustrated in Figure 3-14.

The results from the selection analysis indicate that overall, these regions tend to exhibit only small changes in coverage regardless of whether the self-selection or cross-selection data sets are used. This variation is reduced as the number of transmitters allowed in the receiver is increased. As an example interpretation, when 6 transmitters are used and the AREPS propagator is considered, 75% of the regions showed less than a 5% difference in coverage between self-selection and cross-selection. When the ITM propagator is used, this value increased to 85% of regions for the same tolerance.

These results support a description of the cross-selection sets as *pseudo-optimal*; although a penalty is incurred by using the alternative illuminator selection with a propagator, the penalty is generally not high. Further, the pseudo-optimality suggests that the efficiency of ITM might be exploited, especially in scenarios where fast, low-complexity calculations must be assessed; if AREPS is regarded as *truth* and the goal of the optimization is to achieve the best possible performance (regardless of what that performance might be), then ITM could be used for this task.

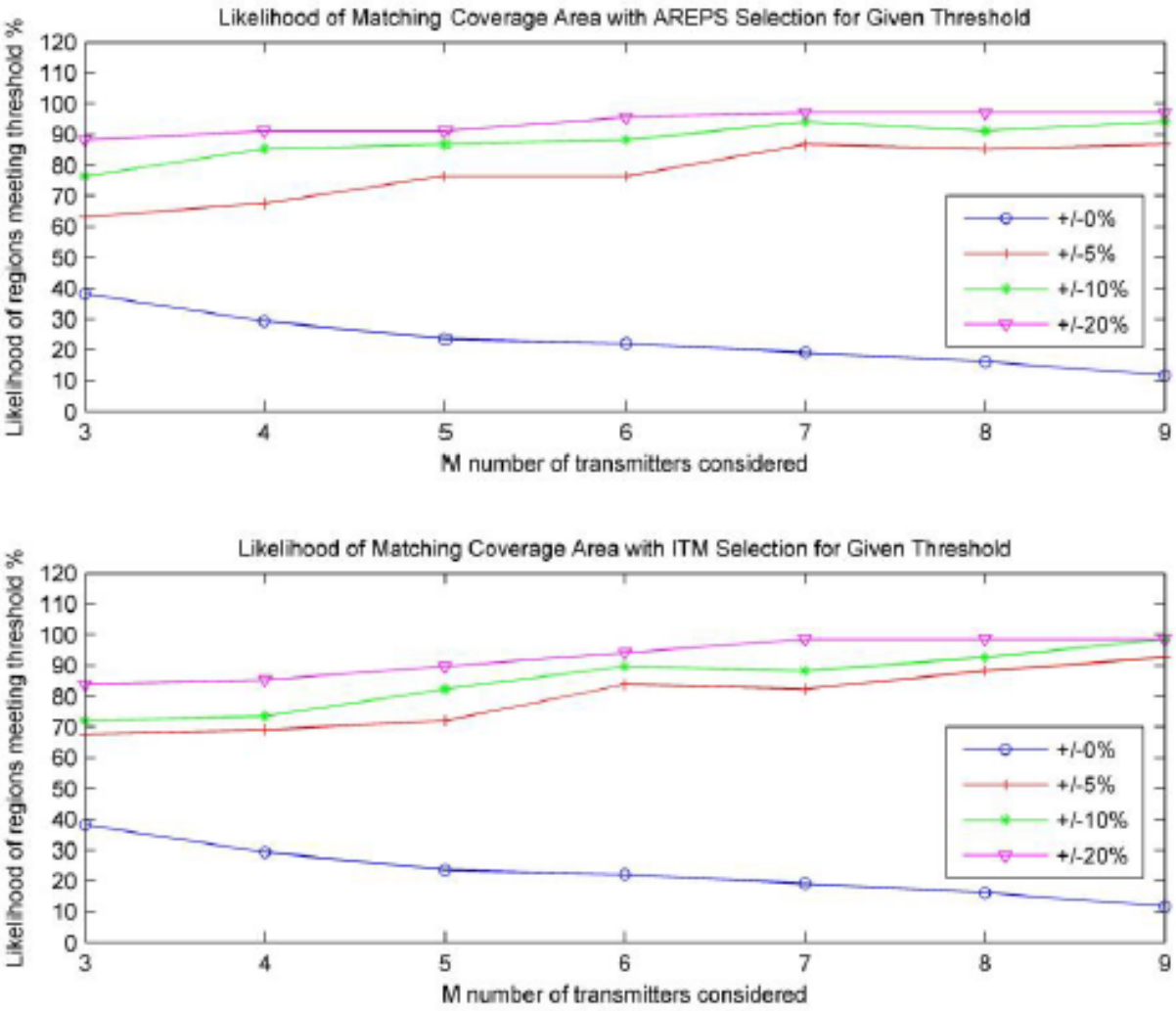

Figure 3-14: Calculated Statistical Bounds for the Self/Cross Selection Analysis, Showing Results Calculated Using AREPS (Top) and ITM (Bottom). An example interpretation of this plot is that when 6 transmitters were used, the metric for AREPS indicated that 75% of regions varied by less than 5% coverage between the AREPS and ITM transmitter sets.

3.2.9 Influence of Models on Illuminator Selection: Atmospheric States

A second analysis, similar to the preceding comparison of AREPS vs. ITM, was performed to examine the influence of the atmospheric state on the illuminator selection problem in passive radar. The state of the atmosphere is a priori *unknowable* to the radar designer; while it can be measured directly by radiosondes or, perhaps, inferred by indirect measurement, the dynamic nature is such that a passive radar must either constantly adapt or accept a performance penalty for being configured in a way that is mismatched to the conditions.

This analysis considered the 1000 atmospheric realizations of the Florida PETOOL dataset, and used the same greedy optimizer to select the subset M of the available N illuminators, selected to maximize the score $D(\mathbf{M})$, calculated as the number of locations satisfying the localization requirement $\sigma_{\mathrm{LLA}} \leq 100$ m, within a range of 150 km from the receiver. As compared to the AREPS analysis (which used a 1 km threshold), this represents a stricter localization requirement. Unique subsets of $M = 6$ illuminators were found as

$\mathbf{M}_k$ different sets across the many ducting profiles. The analysis further calculated the 1000^2 scores $D_j(\mathbf{M}_k)$ arising from using the k_{th} set with the j_{th} profile. These represent both self-selection $D_j(\mathbf{M}_j)$ and cross-selection $D_j(\mathbf{M}_k), j \neq k$.

The ratio of cross- and self-selection represents the penalty of operating within the j_{th} atmospheric conditions using the mismatched illuminator set designed for the k_{th} conditions, and may be taken as a metric of the importance of matching the radar's configuration to the state of the atmosphere. The results are presented as a 2D histogram Figure 3-15. The vertical axis shows $D_j(\mathbf{M}_k)$, given in square arcmin, and the horizontal axis represents the penalty of using the non-optimal set, $D_j(\mathbf{M}_k)/D_j(\mathbf{M}_j)$. One key result from this work is that most scores have only a small penalty (e.g., 92% of points do better than 92% of their optimal coverage), although the worst mismatch penalty was about 52%.

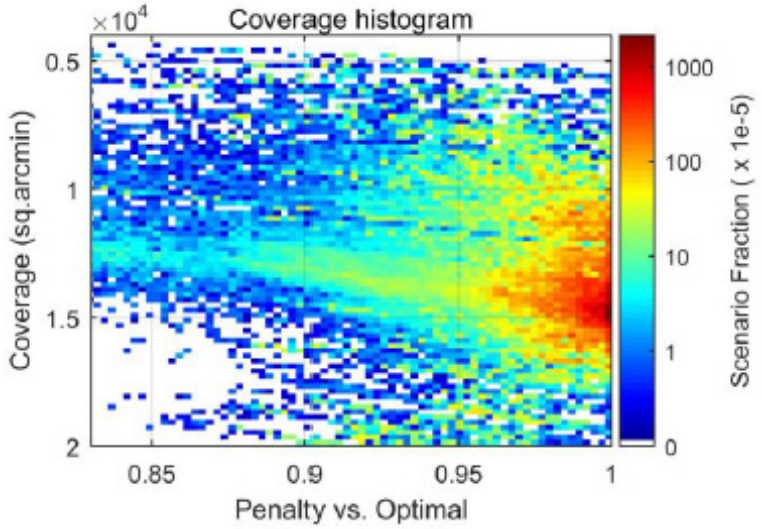

Figure 3-15: 2D Histogram of the Scoring Penalty vs. Realized Coverage for the 1000 Scenarios in Each of 1000 Different Configurations, Indicating that Most Scenarios Exhibit Only Little to Moderate Penalty.

For the radar designer creating a static (non-adaptive) system, it might be desirable to choose a configuration $\mathbf{M}_k$ that performs optimally across all conditions. While several different optimization costs are envisioned for this task, this work used the score $S_k = \min\left(D_j(\mathbf{M}_k)/D_j(\mathbf{M}_j)\right)\ \forall j$, which defines each configuration by its worst penalty across all realizations of the atmosphere. The configuration $\mathbf{M}_k$ maximizing S_k is selected as the best. The Florida dataset yielded one atypical configuration with S_k of 92%, that is, the radar's coverage was at least 92% of the optimum value for those conditions, for *all* atmospheric profiles against which it was tested. Although the atmosphere will continue to affect the performance of the PR, these results show the possibility of designing the PR to negate the requirement dynamically adapting to the atmosphere.

3.2.10 Modeling Atmospheric Variation

A final exploratory effort was undertaken to examine the feasibility of modelling complex propagation coefficients for passive radar with the SSPE models. Complex field analysis might allow usefully-examining time delay, multipath, and atmospheric evolution. A toy scenario was developed for the purpose of exploring the techniques and possible data products: this described a scene with flat terrain, a single illuminator (based on WACX in Florida), and an atmospheric refractivity profile that changed smoothly between ducting and non-ducting conditions.

PETOOL was invoked 40,000 times for this scenario, describing 100 instantiations of the atmosphere (for a linear change between the two states) and over 400 frequencies spanning 600 – 700 MHz. The resulting complex field outputs are described in four-dimensions as $U(r, h, f, t)$, which can be visualized in different ways. Figure 3-16 shows the illumination at 632 MHz at two times during the experiment, $\|U(r, h,)\|$, where the $\|\cdot\|$ applies all corrections from the PE native field matrix to field intensity. The effect of the duct is observed. Next, the field matrix was transformed using the Fourier Transform as:

$$U(r, h, \underline{f}, t) \overset{FFT}{\Longrightarrow} U(r, h, \underline{\tau}, t) \tag{3-8}$$

to represent the delay spread (channel response) observed by each point in the simulation. These are plotted in Figure 3-17 as $U(r, \tau)$ for an observer at 1000 m AGL for the same two times as Figure 3-16 (note that customary 2D/3D normalizations for SSPE techniques are not applied). Here, the time delay τ is expressed as an excess path length relative to the down-range distance; the delay of the direct path is consistent with the refractive index of the atmosphere. The range-dependent decay of the lowest-τ echo is similar, but not identical, to the anticipated decay of specular reflection and warrants further scrutiny.

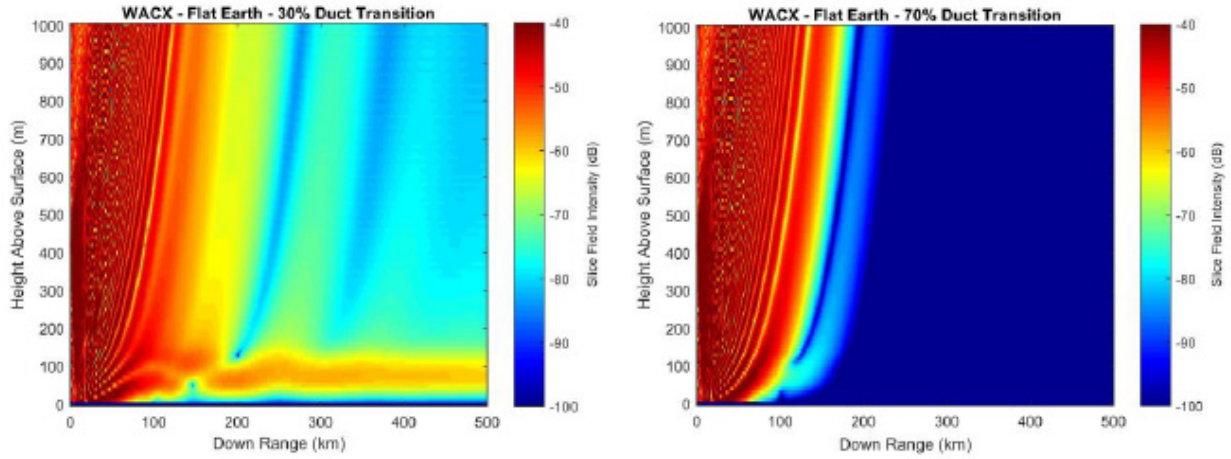

Figure 3-16: Range-Height Illumination Profiles for Time Steps 30% (Left) and 70% (Right) in the Simulation.

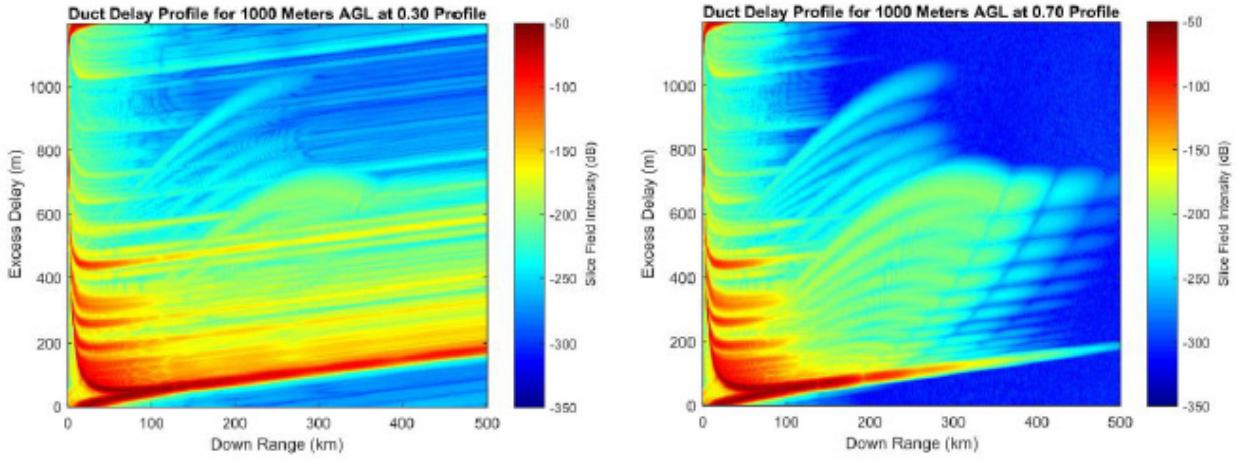

Figure 3-17: Channel Response Profiles Observed at 1000 m AGL as a Function of Range at Time Steps 30% and 70%.

Observing that the delay profiles in Figure 3.17 evolve over time, a final transform examined the effect of the evolution of the duct on the radar's clutter response across the simulation time, as:

$$U(r, h, \tau, \underline{t}) \overset{FFT}{\Longrightarrow} U(r, h, \tau, \underline{f_D}) \tag{3-9}$$

Example results showing $U(\tau, f_D)$ for ranges of 100 km and 200 km at heights of 10 m and 190 m respectively are illustrated in Figure 3-18. These are interpreted like common range-Doppler maps. Key results of this analysis that can be observed from Figure 3-18 include:

a) That the complex field matrix preserved in SSPE propagators appears to offer a viable technique for predicting the channel response of the link;

b) That the channel response for this simulation is observed to have non-zero Doppler components in both the direct path and the clutter as the duct evolves; and

c) That the frequency of the offset response will depend on the timescale of the atmospheric change.

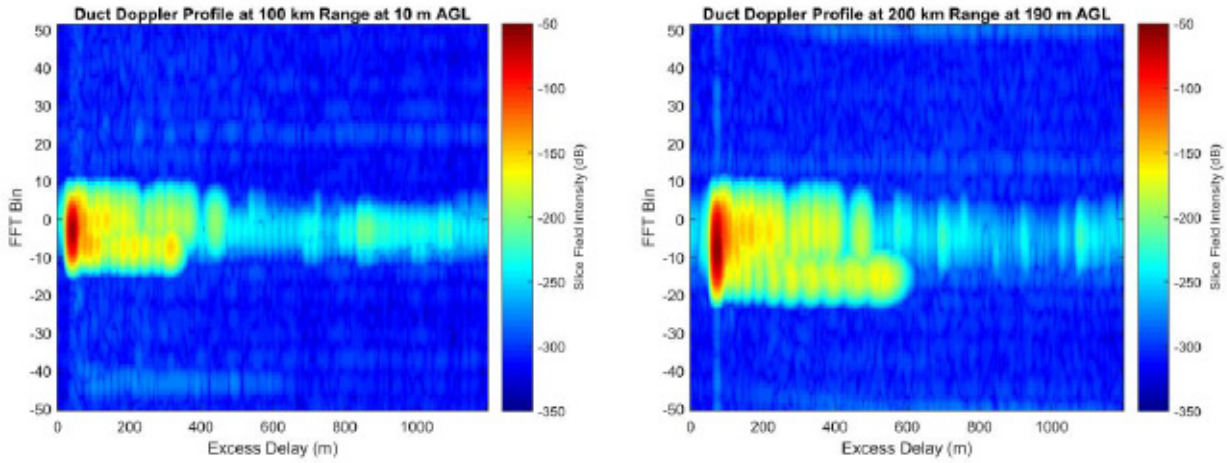

Figure 3-18: Ducting-Induced Range-Doppler Maps at Different Down-Range Locations and Heights – Nonzero Doppler Responses are Due to the Evolving Atmosphere in this Simulation.

These observations could be useful to further characterization of passive radars, as common DSI/clutter suppression techniques either assume the clutter to lie along the zero-Doppler (e.g., ECA), or allow limited variability based the time constant of adaptivity (e.g., LMS). Combining Figure 3-18 with the timescale of the fastest atmospheric change observed in experimental data (about 1 min) gives an anticipated Doppler spreading of about 0.33 Hz. While small, this implies the possibility of an atmospherically-induced non-stationary clutter response. Further investigation of this phenomenon and related techniques is left as an area of future work.

3.3 MEASUREMENTS OF RADIO PROPAGATION EFFECTS

While the previous modelling work and results were limited to simulation, a second set of work focused on experimental campaigns intended to validate and support existing models, and to (where necessary) motivate the development of new models. This work was divided into three campaigns that will be discussed separately, including:

a) The 2015 Ohio measurement campaign, which observed DTV from a fixed 100 foot tower over several weeks;

b) The 2015 and 2017 Daytona Beach campaigns, which included both preliminary measurements of variation as well as a six-month survey of DTV signal variation; and

c) The Armasuisse land mobile measurement campaign, which is described separately, but for which the present work attempted to fit model data to the experimental measurements.

The motivation for the measurement campaigns arises from the acknowledgement that the atmosphere is far from stable in VHF/UHF propagation. Diurnal and seasonal changes in the path loss (e.g., Ref. [28]), not accounted for in static modelling, are well-known and might significantly affect passive radars. One such phenomenon is tropospheric ducting, which carries VHF and UHF radio waves beyond the line of sight. This phenomenon is caused by an inversion in the modified refractivity profile, which creates a trapping layer that can enhance beyond-the-line-of-sight propagation beyond even the line-of-sight predictions [2].

Although the existence of ducting is well-understood, and it can be predicted from the PE propagators when the refractive index profile is known, comparatively few resources exist regarding observational or predictive models to study the effect of ducting (or regular diurnal changes) on passive radar. It is known from other studies that tropospheric refraction exhibits diurnal and seasonal variation as well as dependence on weather and climate. Rudd [3] illustrates the diurnal variation of DVB-T links traversing the English Channel and North Sea. Blood [29] describes UHF data from the VOCAR observations off the coast of southern California. The indicated strength of a 130 km over-sea UHF link is seen to vary by more than 30 dB over several days, illustrating variations possible in PBR observations.

Although the majority of these measurements focus on the one-way link from a broadcast tower to a ground-level receiver, several key points should be considered with respect to the application of this work to passive radar, and are described as follows:

- For ground-based passive radars, this variation will influence the quality of the direct path signal, either favourably or adversely.
- For all passive radars, variations in the clutter illumination will influence the radar's ability to detect certain types and sizes of targets.
- Minor variations might be expected in the illumination or echo involving airborne targets, although the magnitude of this illumination, especially for low-grazing-angle propagation, is not clear.
- The correlation of the variation among ray paths does not appear to be an explored topic, but will be important to passive radar, in determining the joint probabilities of detection for different illuminators.

3.3.1 Ohio Measurement Campaign and Analysis

The 2015 Ohio campaign measured the variation of DTV signals using the Wideband Enhanced Passive Surveillance System (WEPSS) installed on a 30 m tower in Springfield, Ohio. This system's radome houses an array of 4 separate planes of 48 flared notch dipole (Vivaldi) antenna elements, optimized to operate in Lband at around 1.2 GHz. These 4 antenna planes are fed into 48 separate vertical beamformers that provide 2 fixed beam outputs. Only the vertical beam directed at the horizon was utilized. A Wullenweber-style beamformer includes physical switching to utilize a 120° sector of antennas when forming beams, and is capable of steering in 48 different directions. This array is shown in Figure 3-19. The outputs of the array were sampled with a spectrum analyzer and a digitizing oscilloscope, and a MATLAB-based controller coordinated the beam steering and data collection. The results of these measurements were published in Ref. [30].

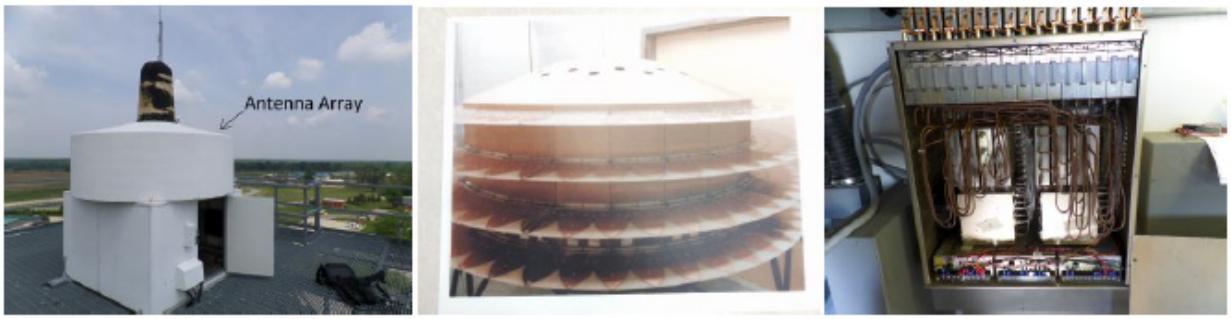

Figure 3-19: Hardware Using the Springfield Data Collection – Tower-Mounted Array (Left, Top of Image), its Vivaldi Elements (Center), and the Hardware Beamformer (Right). The beamformer outputs were sampled by a spectrum analyser and digitizing oscilloscope.

For these measurements, a custom controller was retrofitted onto the beamformer to allow beam steering from MATLAB; a spectrum analyzer (for spectral data) and oscilloscope (for time-domain captures) were used to record data. Spectral data were taken over several weeks by stepping the beamformer through all 48 of its beams. The spectrum analyzer saved a 10 s max-hold capture of each beam; the cycle was then repeated. Measurements were collected over about 10 days in July 2015. Plots of the observed power in selected TV channels as a function of time are contained in Figure 3-20. Each of these stations varied in power by at least 10 dB with some apparently-diurnal component; one in particular (WBNS) has variation exceeding 20 dB. Note that the flat curves at about -88 dBm indicate the system noise floor.

A second data collection recorded a series of half-second time domain captures using two beams over a three-day interval from July 31 to August 2, 2015. The surveillance beam was directed toward the Columbus airport (beam 18) while the reference beam was directed toward the Dayton area (beam 33). Data processing used the extensive cancellation algorithm [31] to suppress the first 100 range bins of DPI and clutter prior to cross correlation. Data were analyzed for two different illuminators (542 MHz and 686 MHz) located about 700 m apart, and about 38 km from the receiver. Figure 3-21 contains results of this analysis illustrating variations in the zero-Doppler clutter response of the CAFs over the course of the three day collect. The generally-diurnal response is similar to the results from Figure 3-20, and indicates variations in the clutter profile that might be observed by a passive radar.

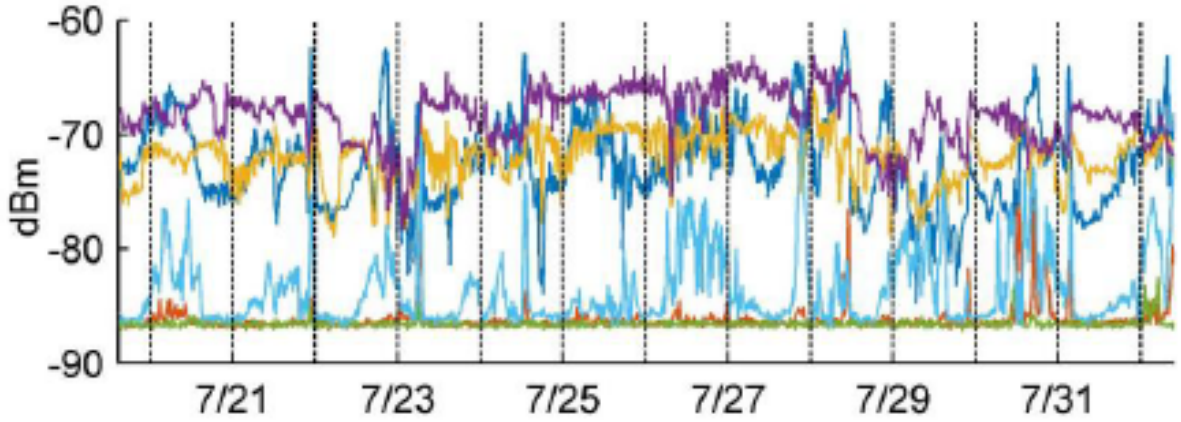

(a) Stations between 500 MHz and 600 MHz

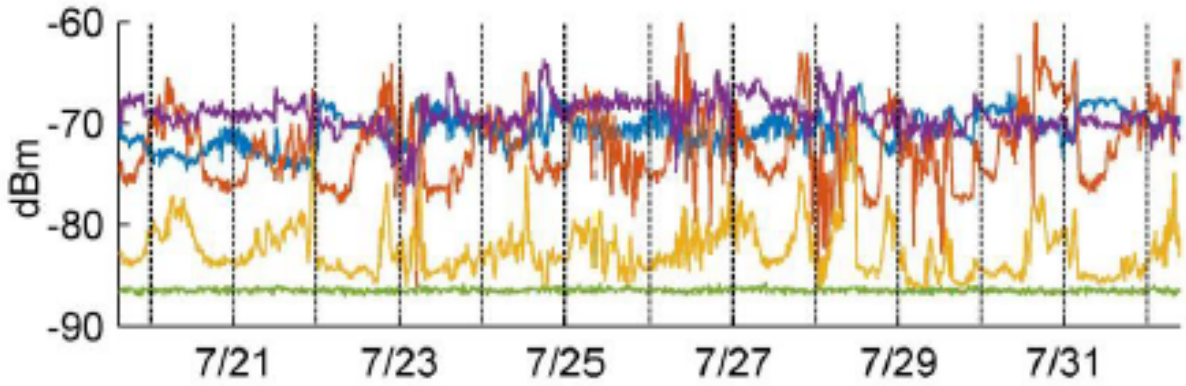

(b) Stations between 600 MHz and 700 MHz

Name	Freq. (MHz)	Latitude	Longitude	Beam Number	Color
WBNS-PT	512	39.9711 N	83.0278 W	11	
WIPB-PT	524	40.0936 N	85.3922 W	38	
WBDT-DT	542	39.7244 N	84.2550 W	33	
WRGT-DTV	566	39.7244 N	84.2550 W	33	
OH-PT-1116	572	39.1164 N	84.5019 W	29	
WLWT-PT	596	39.1242 N	84.5217 W	29	
WCHS-TV	632	38.4078 N	81.9036 W	18	
WHIO-DT	632	39.7339 N	84.2481 W	33	
WWHO-PT	662	39.5889 N	83.1122 W	15	
WSYX-DR	674	39.9372 N	83.0211 W	11	
WDTN-PT	686	39.7186 N	84.2361 W	33	
WKEF	692	39.7244 N	84.2550 W	33	

Figure 3-20: Power Variations Observed in Beam 18 of the Springfield Data. The colors in (a) and (b) are believed to correspond to the stations identified in the legend. All date labels are at noon of that day, with grid lines every 24 hours. Note that Beam "0" is approximately magnetic north, and each beam increment is about 7.5° in azimuth.

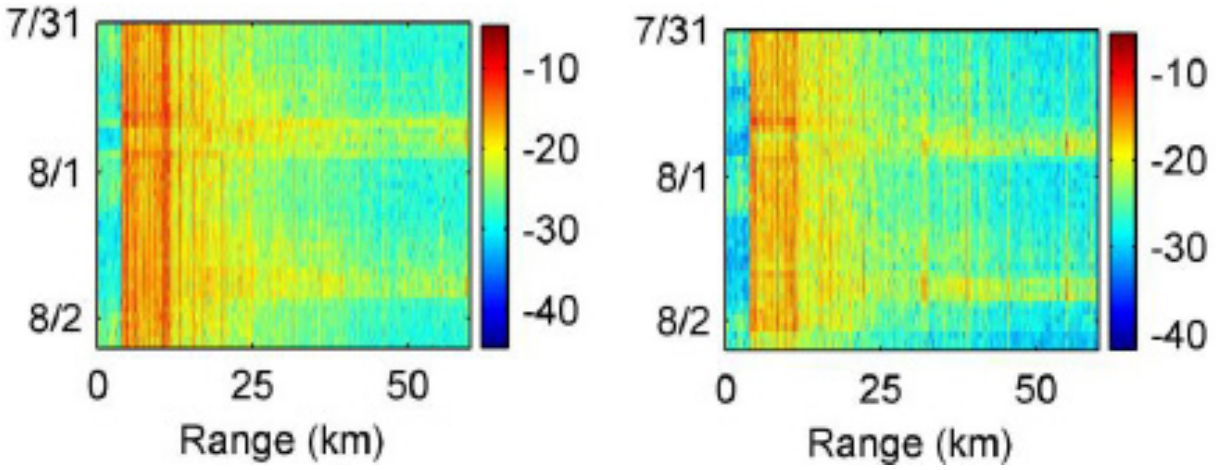

Figure 3-21: Raw Clutter Power (in dB, Arbitrary Scaling) for WBDT-DT at 542 MHz (Left) and WDTN-PT at 686 MHz (Right) Showing Variation Over Several Days. Date labels are at noon on each day.

Visual examination of the power time series in Figure 3-20 motivated a statistical analysis of these curves, as some stations exhibit seemingly-correlated fluctuations (WWHO and WSYX), while others are seemingly anti-correlated (WRGT and WBNS). A computational analysis of these data examined the correlation coefficients between the time series for pairs of stations, e.g., $\rho_{T1,T2} = \mathrm{cov}(P_{T1}(t), P_{T2}(t))/(\sigma_{T1}\sigma_{T2})$. The results were examined visually as a function of measurable attributes, such as azimuth difference, range, and frequency difference, to identify any dominant contributing factors. The results of this analysis are shown in Figure 3-22. These data suggest that:

- Stations in the same direction are generally, but not exclusively, positively correlated; and
- Stations in opposite directions are generally, but not exclusively, inversely correlated.

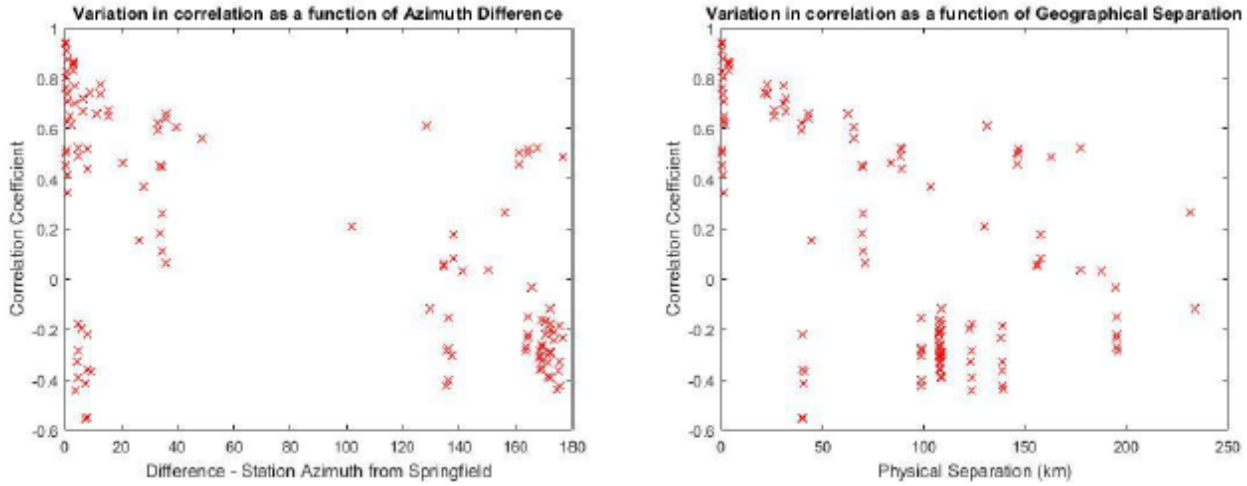

Figure 3-22: Scatterplots of Direct Path Variation Observed in the Springfield Data, Plotted Against Azimuth (Left) and Station Separation (Right). Although the limited data does not provide a definitive model, suggestive clustering is observed.

From the perspective of passive radar performance prediction, correlations among fading are important because they can be describe conditional probabilities of the variation of the path losses along different atmospheric links, e.g., $P(LOSS_1|LOSS_2)|$. Such calculations can assist in determining optimal illuminators

and predicting overall statistical performance. As of this writing, no similar analyses establishing the statistical correlation of this fading, or its spatial scale, have been identified in the open literature. As identified in the discussion of the Daytona Beach measurement campaign, examination of this effect should be a topic of future work.

3.3.2 Daytona Beach Measurement Campaign and Analysis

The Daytona Beach measurements included two campaigns (2015 and 2017) aimed at characterizing the surface variability of DTV signals over a more-significant timescale (ultimately six months). These measurements were performed at Embry-Riddle Aeronautical University, using antennas on the roof of the Lehman Engineering Building, about 17 m above the ground. The 2015 campaign used only a V-polarized discone, while the 2017 campaign included an additional H-polarized directional bowtie array. DTV signals in the United States are H-polarized. A photograph of the measurement site, and its relationship to prominent local stations (principally to the south and south-west) is shown in Figure 3-23.

Figure 3-23: FCC Map of the Prominent Transmitters Near Daytona Beach (Left); Photograph of the ERAU Measurement Site Showing the H-pol Array and V-pol Discone (Right). The view of the photograph is south-southwest.

The 2015 campaign spanned two months from March to April of 2015. Uncalibrated power measurements were automated using a spectrum analyzer and computer. Ten 18 MHz bands composed the entire collection range of 180 MHz; each band was visited for ten sweeps at a cadence of approximately 30 minutes. The spectral resolution was 70 kHz, which provided about 85 points per station and was sufficient for identifying passband characteristics. Example data in Figure 3-24 show diurnal variations (left) and a stronger enhancement event (right).

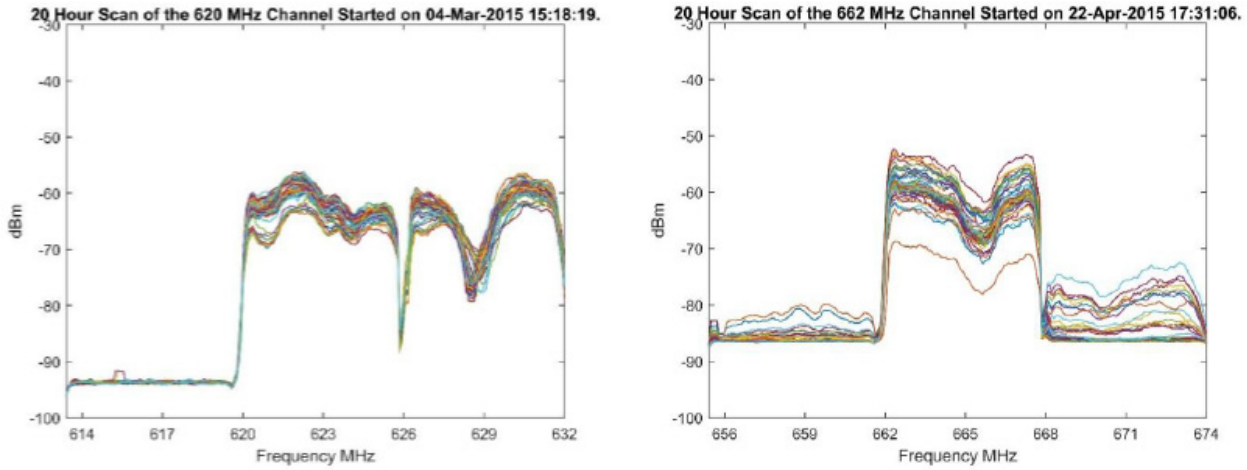

Figure 3-24: Two 20-Hour Profiles from the First Daytona Beach Campaign, Which Show Typical Diurnal Variation and Evident Change in Multipath (Left), and Ducting of Different Stations Having Different Time Profiles (Right).

The 2017 campaign was intended to improve on the techniques used in the 2015 Daytona and Springfield measurements, and had the specific goals of obtaining:

a) Dual-pol data;

b) A high recording cadence, so that the smooth evolution of the propagation could be identified; and

c) High spectral resolution covering the entirety of the UHF television band simultaneously.

Goal (a) was supported by adding a horizontally polarized antenna to the observation site. Goals (b) and (c) were supported by the development of a custom real-time FPGA spectrometer using the ROACH platform and high-speed 3.2 GS/s samplers. These data had characteristics of:

- Data direct-sampled at 3.2 GS/s and digitally decimated using a 200 MHz FPGA;
- A spectral resolution of 48.8 kHz, presenting 6144 frequency bins generated by two overlapping 4096-point FFTs with 100% duty cycle over the entire window;
- A recording window of 400 MHz to 700 MHz, usefully-presented as 450 MHz to 700 MHz due to high pass filtering required to eliminate local interferers;
- A mean temporal cadence of 0.35 s; the temporal cadence was determined by the software receiving the spectral data, and did not have real-time constraints; and
- This second campaign collected data for approximately six months, from January 14 to July 10 2017 and resulted in about 1.28 TB of data.

The resulting spectra were recorded at an average cadence of about 2 Hz. With the exception of several short interruptions, data collection ran continuously for almost 6 months. The example in Figure 3-25 shows measurements of a strong station at 584 MHz (integrating the power from 584 to 590 MHz), normalized to its median value, for 20 days selected from the dataset. A small diurnal variation of several dB is present. Two additional unexpected features include short signal dropouts (e.g., around day 60) and longer off-air events (about day 66). These features illustrate an important aspect of the *reliability* of illuminators; passive radar modelling should consider that even otherwise-dominant local illuminators might become unpredictably unavailable.

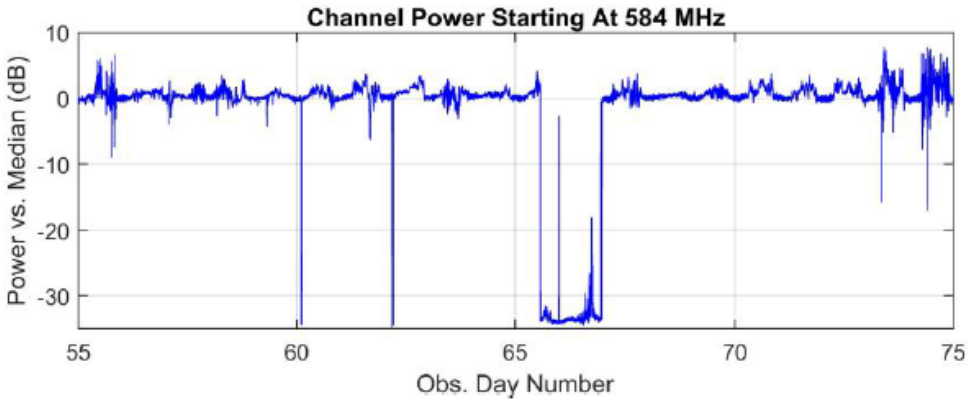

Figure 3-25: Channel Power of a Typically Strong Signal, Showing Minor Daily Variation in Addition to Both Brief and Extended Off-Air Events.

Selected data from two additional stations are illustrated in Figure 3-26. The top panel shows a station at 614 MHz, which is nominally below the noise floor of the receiver. While Diurnal variations show typical enhancement of up to 10 dB, the feature at Day 10 shows an enhancement of almost 40 dB and was associated with intense weather[1]. Conclusively assigning this signal to a specific station is challenging; candidates within 4° of Daytona Beach include WTCE (1 MW, 255 km, predicted 33.5 dBuvm^{-1}) and a smaller, but closer WHDO (15 kW, 97 km, predicted 38.9 dBuvm^{-1}). This figure emphasizes the importance of considering atmospheric variability in passive radar. Regular diurnal variations will change clutter illumination, target illumination, and DPI, and might be exploited either to minimize interference or allow a receiver to sample distant reference signals. Extreme events, like the duct illustrated, might allow otherwise unusable signals to be used as illuminators, or unexpectedly enhance clutter or CCI in a way that prevents normal target detection.

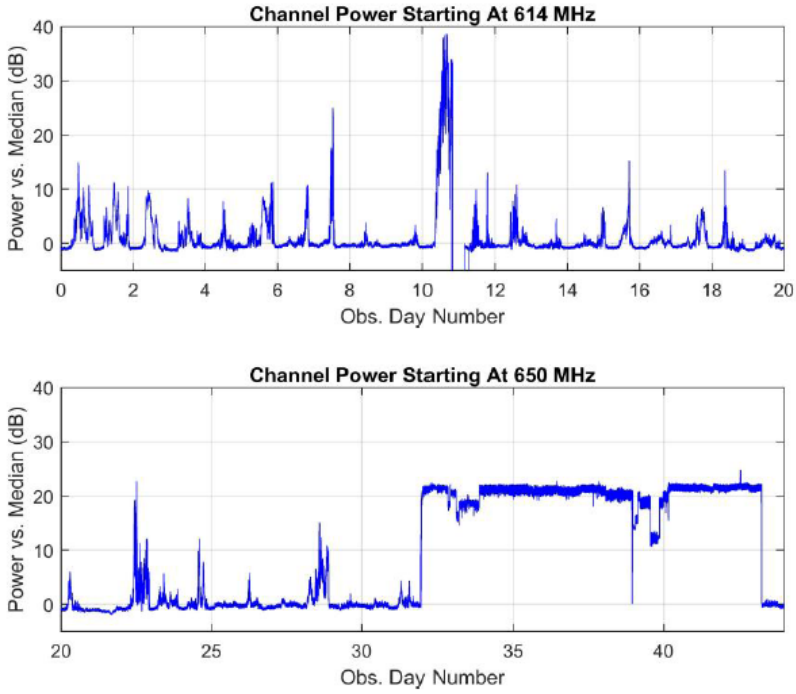

Figure 3-26: Channel Powers at 614 MHz (Top) and 650 MHz (Bottom).

[1] The loss of signal following the duct was caused by a power interruption at the measurement location.

The second panel in Figure 3-26 shows the unexpected appearance of a new station beginning on about Day 32. This station persisted for just under two weeks and then vanished. The appearance was associated with major events at the Daytona International Speedway. This plot emphasizes that illuminator *discovery* might be important to passive radar, to identify otherwise-unknown useful illuminators.

The next analysis attempted to assess the predictive accuracy of the ITM by comparing measured and predicted powers of individual stations. All stations between 470 MHz and 668 MHz (identified by their lower edge) were considered. Each station ID was presumed as that for which ITM predicted the highest flux at the measurement site. Results are presented in Table 3-1; here, the *Predicted Flux* column is that originating from ITM and *Measured* indicates the H-pol data, normalized and averaged across the channel's band and across 2 days of measurements. The *Score* for signals above the noise floor is calculated by the difference of these two, normalized by the average distance across all of the observed stations, as:

$$Score_n = \left(P_{\mathrm{ITM},n} - P_{\mathrm{Meas},n}\right) - \underset{n}{\mathrm{mean}}\left(P_{\mathrm{ITM}} - P_{\mathrm{Meas}}\right) \tag{3-10}$$

Table 3-1: Table of All Stations Observed in the Daytona Measurements, Showing the Most Powerful Flux (and Station) Predicted on Each Channel, the Normalized SNR Observed in a 2-Day Average, and a Matching Score Discussed in the Text.

Frequency (MHz)	Station	Distance (km)	Azimuth (°)	Predicted Flux (dB µvm-1)	Avg. Power (dB-Norm)	Score
470	WDYB-LD	33	222	76.2	-0.087	–
476	WNFT-LD	155.7	195	27	-0.1168	–
482	WVCI-LP	75.5	164	42.3	-0.3146	–
488	WKCF	67	183	92.2	10.0077	22.0752
494	WESH	38.2	223	82.2	0.0261	–
500	WTEV-TV	131.5	338	48.2	-0.5512	–
506	WARP-CD	212.9	227	19.1	6.0957	-47.1128
512	W21AU	76.1	212	41.6	-0.4465	–
518	WOFL	65.2	183	97.8	26.9593	10.7236
524	WUCF-TV	65.4	184	97	29.6497	7.2332
530	WPXC-TV	194	340	38.6	-0.1039	–
536	WJGV-CD	76.7	305	44.1	-0.2834	–
542	WKMG-TV	64.4	181	96	31.1334	4.7495
548	WRDQ	69	181	96.4	35.1158	1.1671
554	WGFL	155.7	289	36.4	0.1118	–
560	WFTS-TV	191.1	219	39.9	0.2467	–
566	WEFS	64.4	181	94.7	32.0238	2.5591
572	WOGX	125.7	212	43.4	-0.1007	–
578	WAWS	131.5	338	47.9	0.3158	–
584	WDSC-TV	64.4	181	94.9	31.4185	3.3644
590	WCWJ	130.8	219	46.9	0.5284	–
596	WRCF-CD	71.3	195	47.5	2.0175	-14.6346
602	WZXZ-CA	67.6	182	52.2	-0.3375	–

Frequency (MHz)	Station	Distance (km)	Azimuth (°)	Predicted Flux (dB μvm-1)	Avg. Power (dB-Norm)	Score
608	–	–	0	–	-0.8269	–
614	WHDO-CD	97.2	200	38.9	1.6849	–
620	WFTV	69	181	96.2	37.2065	-1.1236
626	WACX	67.1	183	99.4	34.8511	4.4318
632	WRBW	64.4	181	99.3	33.4003	5.7826
638	WJXT	130.1	338	46.8	-0.335	–
644	WOTF-DT	67	183	89.7	28.2322	1.3507
650	WJEB-TV	130.8	338	47.3	0.1083	–
656	WTBT-LD	193	338	21.6	0.3424	–
662	WTGL	67	183	98.4	38.8493	-0.5664
668	WFTT-DT	190.7	219	35.5	0.9114	–

It should be observed that, under this normalization, a perfect match would exhibit all scores having a value of 0 dB. Caveats of the interpretation of this table include:

- The most extreme outlier among detected stations was WARP, which was detected at a level significantly stronger than anticipated (a score of -47 dB); this was not investigated and could have represented a newer station not described by the database;
- The low-frequency response (488-550 MHz) probably includes contributions from the first low-pass filter, applied prior to the first-stage amplifier[2]; and
- The detection of WRCF (-14 dB), was of a very low SNR (2 dB), and so the score could be influenced by the noise floor or an error in the normalization.

If the preceding stations are neglected, the remaining data span a range of 6.9 dB and have a standard deviation of 2.54 dB. This result appears within expected confidences extracted from the confidence parameters of the ITM [7]. It is noted that the group of stations considered in this case were bounded within 4° of azimuth, and so variations due to the receiver's broad azimuthal beam were not considered significant.

Additional analyses were next applied to the dataset following a process of time-frequency calibration and channel integration. The calibration process used noise floor measurements in empty (unassigned) DTV slots to estimate the frequency-dependent bandpass gain of the system. Temporal measurements of the empty slots were used to calibrate hypothesized diurnal (potentially temperature-dependent) gain variations of the receiver. In total 39.2 million power values were generated for the 40 channels, representing data recorded over about 6 months with an average cadence of about 400 ms.

3.3.2.1 Dropout Analysis

The most peculiar phenomena in the data are temporary dropouts. Most of the stations exhibited this phenomenon; the five least-reliable stations exhibited between 49 and 225 dropouts over the campaign (as measured by a signal drop of at least 6 dB in one 400 ms data frame). Figure 3-27 illustrates the distributions of these dropouts; most are several seconds, and the worst station has typical dropouts of about 8 – 10 seconds. The source of this phenomenon has not been identified, but it is anticipated to be related to the reliability of the transmitter; Figure 3-28 contrasts a time-frequency plot for a drop-out event with one for

[2] This filter (Minicircuits SHP-600) was required to mitigate intermodulation products caused by sporadic local 400 MHz-band radios. These were applied before the LNA, which determined the noise floor and the ultimate pass-band normalization.

naturally-occurring fading (which is not detected by the algorithm). The associated dropouts of the several stations could indicate a common cause (e.g., an interruption of local power).

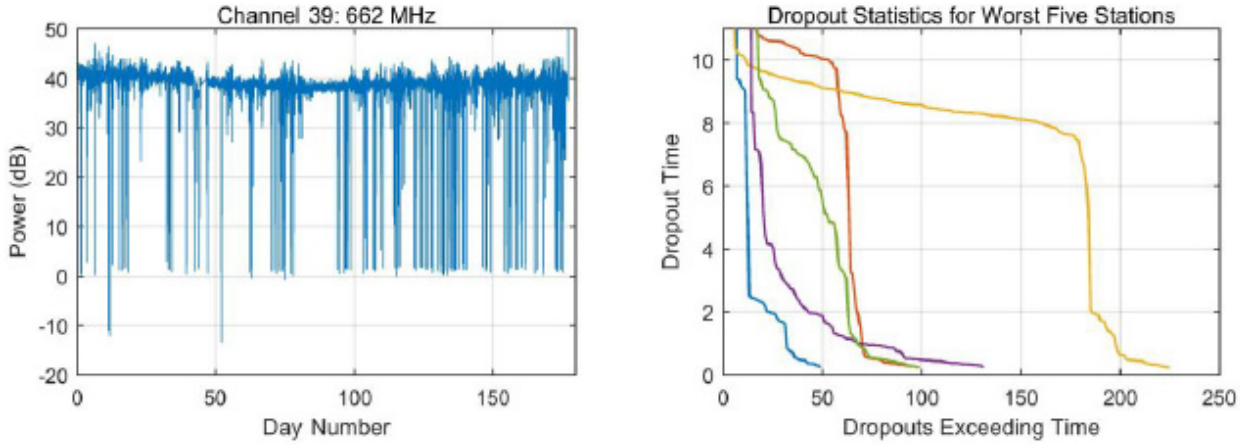

Figure 3-27: Power vs. Time for the Station that Exhibited the Lowest Reliability (Left); Collections of Dropout Times Exhibited by the Five Least-Reliable Stations (Right). Typical dropouts are on the scale of several seconds.

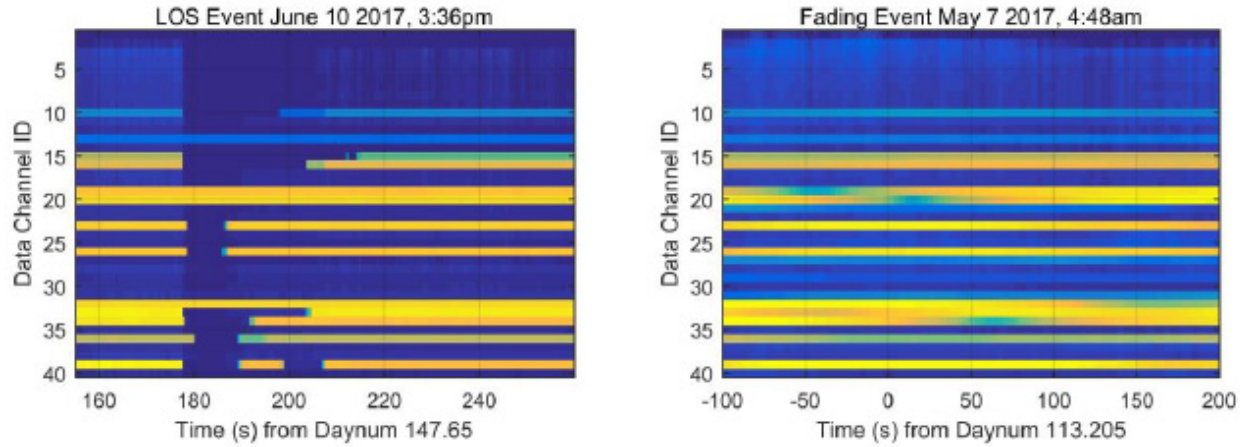

Figure 3-28: Comparison of Signal Loss Attributed to Transmitter Reliability (Left) and Natural Fading (Right). The natural fading occurs on a much slower timescale and is not detected by the dropout detection algorithm.

3.3.2.2 Power Histograms

Each of the normally-visible channels was processed to produce a power histogram and quantify the expected variation. The 6-month channel powers were averaged using a 30 s window, binned in 0.3 dB intervals, and plotted as the likelihood of an observed deviation from the median value. Results of this analysis are contained in Figure 3-29, with stations grouped as strong and weak (normally not visible); both plots include the statistics of a band containing no station (dashed red) as a reference distribution of the thermal noise and instrumental effects.

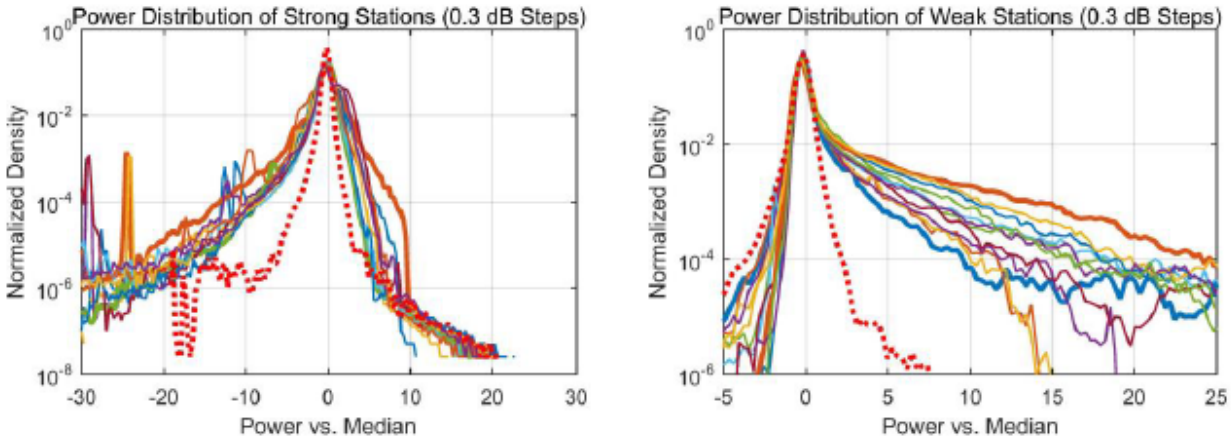

Figure 3-29: Histograms of the Deviations of Strong (Left) and Weak (Right) Stations, Compared to a Noisy Channel (Dashed).

Two key aspects that can be observed from the differences in the distributions are as follows. First, strong stations exhibit a wider distribution than implied by noise statistics alone, and appear slightly biased toward fading events (reduction in signal). Second, the ducting probability for weak stations appears consistent with a power law, with different stations exhibiting different slopes.

It is presumed that these results are consistent with foundational work in broadcast statistics. It is noted, however, that the statistical models known to the author do not generally reproduce these distributions. The ITM statistical model is consistent with a normal distribution (in dB). In contrast, the model given for ITU P.1546 [5] uses a piecewise-linear model for likelihood vs. deviation.

3.3.2.3 Time-of-Day Histogram

Given the anticipated association of signal variability to temperature and weather events, the data were binned to create histograms by time-of-day, as a first attempt to view this behaviour. The power samples for each station were grouped according to time-of-day with intervals of 7.2 minutes (200 intervals in a day). Binning of 0.2 dB was used in amplitude, and the 6 month campaign data were sorted to produce a 2-dimensional histogram (occurrence vs. power and time of day). In addition, the standard deviation vs. time of day was calculated for the inner 98% of the data (to discard several outliers that would skew the results).

Examples of these plots for interesting stations are shown in Figure 3-30 and Figure 3-31. These plots suggest that the evening, overnight, and morning hours appear to have the highest volatility, with the most reliable atmospheric conditions between about 9:30 am and 2:30 pm; although this is not corrected for season. Additionally, the prevalence of dropouts in the daylight hours suggests the possibility that they are either maintenance-related or heat-related.

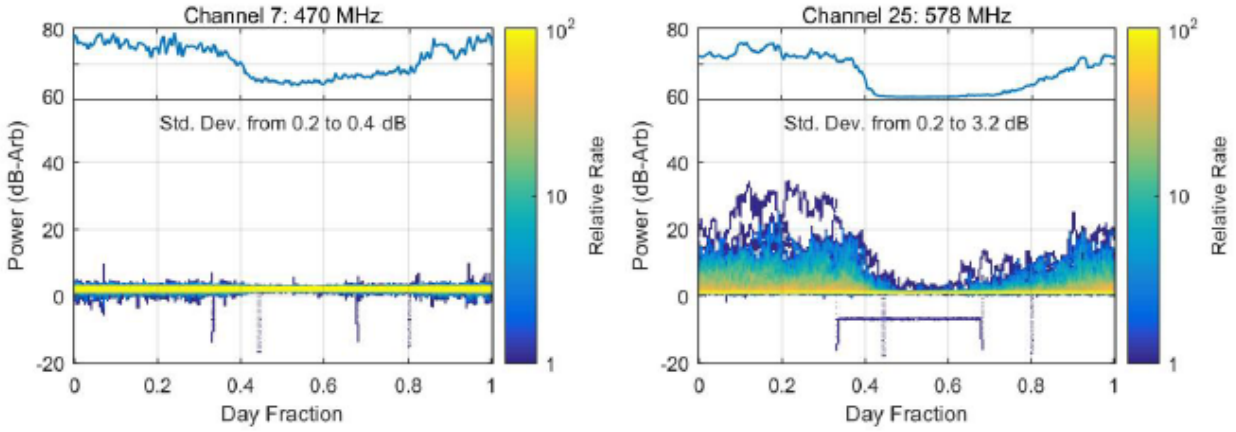

Figure 3-30: Time-of-Day Histograms – (Left) A Noisy Channel; (Right) A Normally-Hidden Station that is Observed to Exhibit Significant Ducting During the Dataset. It is observed that few ducting events occur near midday or afternoon.

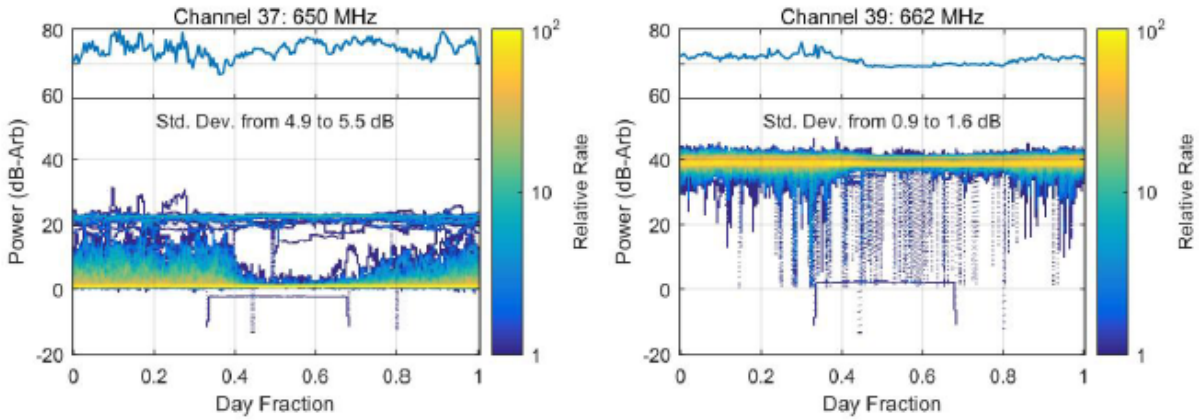

Figure 3-31: Time-of-Day Histograms – (Left) The Station that Exhibited a Temporary Broadcaster During Racetrack Events, but Exhibited a Ducting Channel During Other Times; (Right) The Strong Station that Exhibited the Most Signal Dropouts.

3.3.2.4 Statistical Correlation

The final analysis that was considered here is a statistical correlation of the transmitters amongst each other. In this process, each of the integrated and calibrated channel powers was correlated with the time series for the other channel powers, according to the process:

$$\Xi_{xy}(\tau) = \mathrm{cov}\big(A * P_x(t), A * P_y(t)\big) \,|\tau \leq t < (\tau + T) \tag{3-11}$$

This approach creates time-dependent covariance (and correlation) matrices and is necessary since atmospheric variation does not correspond to a stationary process.

Two analyses were conducted, using windows of 15 minutes and 2 hours, and used only the data for the strongest observed stations. The power series were filtered using both 10-second and 7-minute averaging, A, to emphasize the desired timescale. Each was conducted twice; first considering all of the data, and second limited to only the time slices with $\mathrm{var}(P_x(t)) > 0.5\mathrm{dB}^2$. Results are shown in Figure 3-32 and Figure 3-33. Key results suggested by these data include:

a) Few strong correlations exist on the short timescale, but more are suggested when using only the stronger-variance data; and

b) The long timescale suggests correlations that are skewed-positive among all stations.

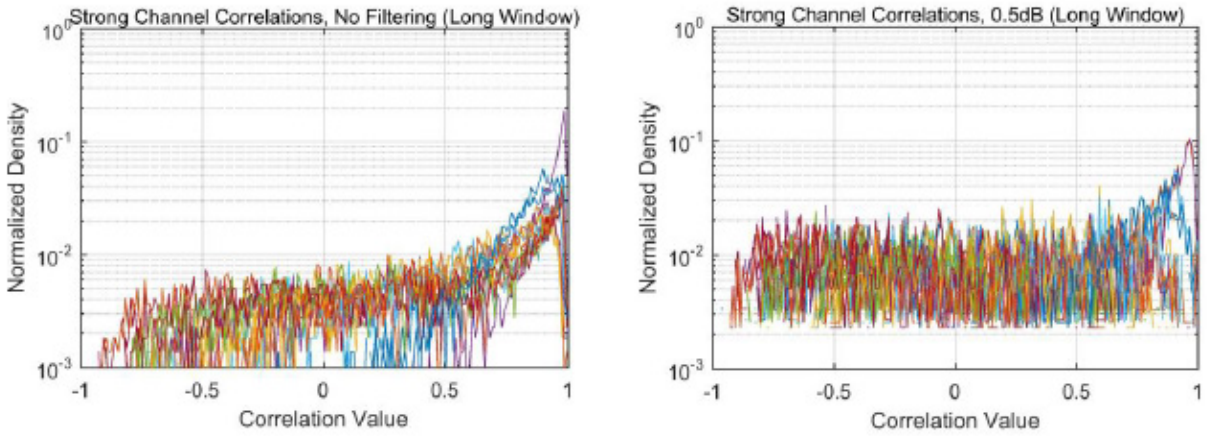

Figure 3-32: Cross-Correlation Histograms for the Strong Stations Using a 15-Minute Window and 10-Second Averaging, Including All Data (Left) and Thresholded to Only Windows with a Covariance Greater than 0.5 dB^2 (Right).

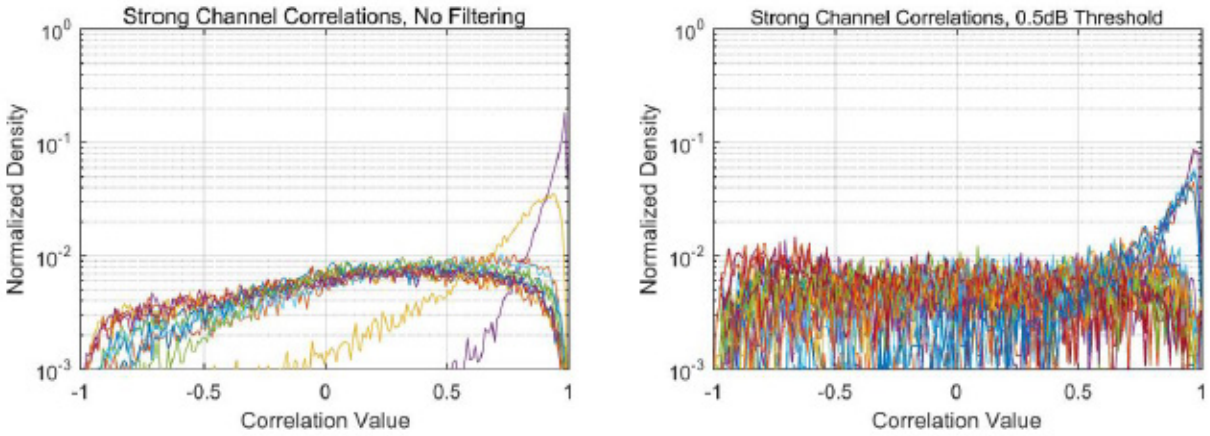

Figure 3-33: Cross-Correlation Histograms for the Strong Stations Using a 2-Hour Window and 7-Minute Averaging, Including All Data (Left) and Thresholded to Only Windows With a Covariance Greater than 0.5 dB^2 (Right).

Three stations were selected for further analyses and are summarized in Table 3-2. The correlation plots, shown in Figure 3-34, present a remarkable difference: the collocated stations (566 and 584 MHz) are very strongly-correlated, while those with a slight geographic offset (566 to 524 MHz) exhibit no strong trend. Figure 3-35 shows measurements selected periods of instability for these stations. Note, however, that *uncorrelated* does not imply *independent*; these processes are not stationary and the periods of instability do appear correlated: solving $\mathrm{corr}\left(\mathrm{var}(P_x(t)), \mathrm{var}\left(P_y(t)\right)\right)$ yields 0.9 between the well-correlated stations, and varies between about 0.2 and 0.6, depending on the timescale, for the uncorrelated pairs (e.g., 524 MHz with 566 MHz).

Table 3-2: Table of Stations Selected for More-Detailed Profile Analysis.

Frequency (MHz)	Station	Distance (km)	Azimuth (°)	ITM Predicted Flux (dBuvm-1)	Avg. Power (dB-Norm)
524	WUCF-TV	65.4	184	97	29.6497
566	WEFS	64.4	181	94.7	32.0238
584	WDSC-TV	64.4	181	94.9	31.4185

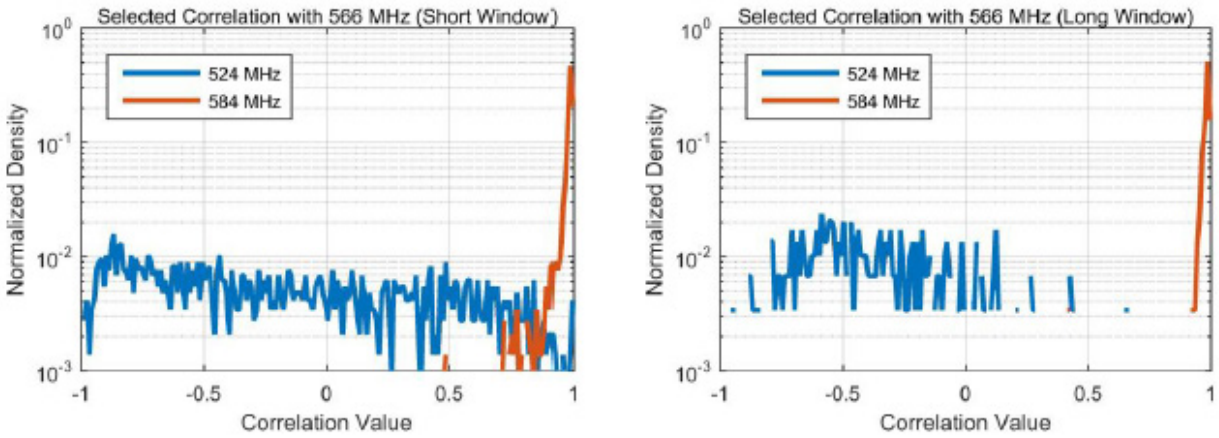

Figure 3-34: Correlation Histograms for Selected Stations with the 566 MHz Station, Showing that 524 MHz has a Slight Preponderance of Negative Correlation, and 584 MHz Correlates Very Strongly Over Both Timescales.

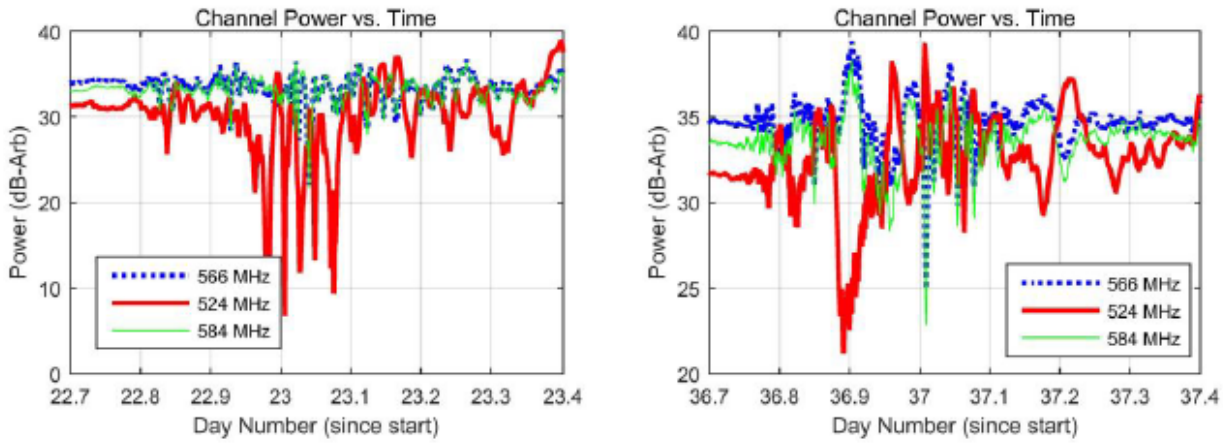

Figure 3-35: Power Profiles for Selected Intervals for the Three Labelled Stations, Showing Strong Correlation Among the Collocated Stations (566 MHz and 584 MHz) but No Clear Correlation to the Slightly-Offset Station (524 MHz).

These results suggest much weaker correlation among the illuminator variability than was observed in the Ohio dataset. At present, it is not known whether this represents differences in the geography or the measurement technique. This discrepancy should be investigated in future work.

3.3.3 Modeling and Analysis of Armasuisse Data

A third area of propagation work was aimed at validating propagation models and techniques against ground-truth data. The analysis focused on a 2015 dataset provided by Armasuisse (described elsewhere in the SET-207 report), and attempts were made to reproduce the measured values in simulation. This dataset was captured by a mobile receiver (mounted on an automobile), which measured the power of FM broadcast stations as it traversed several driving paths. The recorded power series were provided to ERAU for analysis.

Recorded data included the receiver's position as well as the calibrated flux density of three stations (94.6 MHz, 98.3 MHz, and 99.2 MHz). Although three journeys exist in this dataset[3], the bulk of the analysis was allocated to the Dub-Eff data. These data were provided with a link to the Swiss public transmitter records, which allowed the analysis to test:

a) Generating transmitter database information from the public records in an untested region; and

b) Testing transmitter discovery against the database.

The goal of the analysis was to reproduce the measured powers, and the success metric was the degree of agreement.

The most significant lessons learned from this experiment were that:

- Coarse terrain and data gridding are insufficient toward producing satisfying results; it was necessary to use very fine grids to obtain patterns resembling the measured data;
- The propagation tools do a poor job of simulating fluxes near ground level, as they do not account for clutter, especially where the clutter might dominate large-scale shadowing; and
- It is worthwhile to remember that the approaches to frequency planning are very different depending on the nation in which one is operating; here, the low power of one transmitter (500 W) led to it being automatically discarded at some stages of early processing.

The analysis used several stages configured as follows:

- **Step 1:** Utilize a grid of 0.2 km in range and 0.5° in azimuth to simulate candidate regional illuminators. This invokes Prelude using the SRTM2 terrain sets, a sea-level standard atmospheric model, and using a region gridding of $0.1'$ (about 185 m in latitude). This process examines receiver heights of 3, 10, and 15 m AGL.
- **Step 2:** Interpolate the driving path into the lateral grid to estimate the received power at each path location. Modify the power by the ITU P.1546 [5] receiving height expressions (Annex 5, Section 9), which correct for a receiver below the representative clutter. This correction is most sensitive to R_2, the notional height of the ground cover; this work used a value of 15 m as similar to local building heights on Google Earth, which resulted in corrections of about 12 dB.
- **Step 3:** Identify the likely transmitter as the strongest one in the data set; if several stations are similar, examine the models to determine whether they represent distinct transmitters or duplicate station entries. For duplicate entries, retain the data thought to be most-accurate.

Note that the disambiguation in Step 3 is required because the Prelude transmitter database merged data from three separate tables provided by OFCOM. These tables were of differing quality, geographic range, and partially overlapped.

- **Step 4:** Utilize a much denser gridding of 30 m in range and 1.5° in azimuth to simulate the likely candidates; at 70 km range this azimuth step corresponds to 30 m. Manually invoke the propagators

[3] These journeys are hereafter referred to by the major cities involved, as per the authors of the work, as Dübendorf-Effretikon (Dub-Eff), Effretikon-Wallisellen (Eff-Wal), and Zürich-Thun (Zrh-Thun)

outside of Prelude so that only azimuth slices covering the trajectory are simulated. Project the pattern into a lateral grid 0.9′ in latitude and longitude (about 28 m in latitude); this is the limit of the terrain that was available for this work.

- **Step 5:** Repeat the interpolation work of Step 2. Examine both the directly-simulated ground-level data and the 15 m data scaled by the ITU height corrections to account for the likely influence of clutter. Compare the predicted paths to the measured paths.

Figure 3-36 contains lateral maps that are helpful to the interpretation of the intermediate data, selected for the Uetliberg (UTLI) transmitter. The red curve in each plot is the Dub-Eff driving path. The left panel shows the terrain between the UTLI transmitter and the path; the right panel shows the surface flux predicted by TEMPER. The hill at about 47.37° N 8.6° E is thought to dominate the large-scale shadowing of this transmitter.

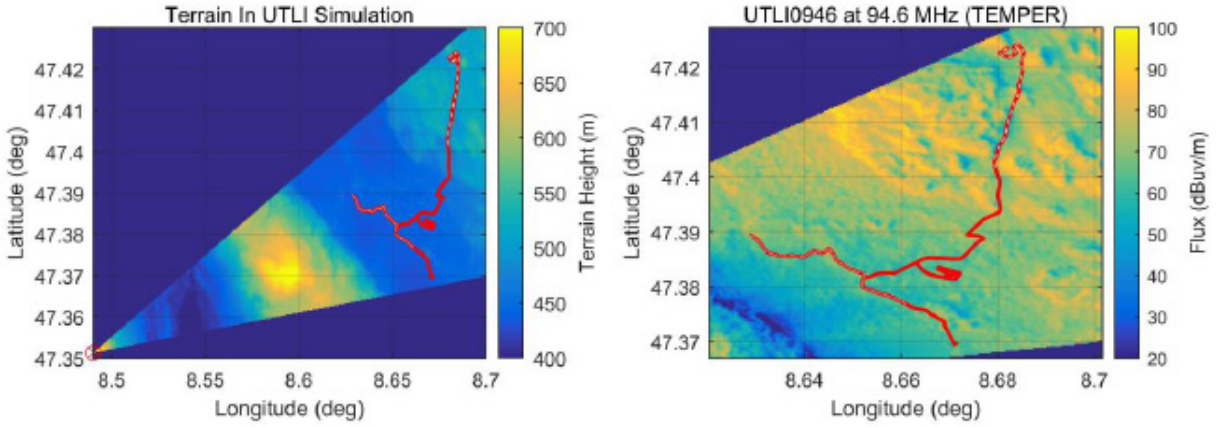

Figure 3-36: Lateral Elevation Map (Left) Showing the Terrain and Driving Path, and Flux Map (Right) for the UTLI Transmitter, Focusing on the Region of the Driving Path. The simulation is limited to a small azimuthal range from the receiver because of the very dense sampling of points in both azimuth and range, producing the 30 m grid, as discussed in the text.

Various experiments were performed during this analysis in an effort to align the models with the measured data. Given the time required for each simulation, only limited quantitative work was done with each. Qualitatively, however, some observations include the following:

- TEMPER and PETOOL provide similar results when configured for PEC terrain and using the ITU clutter correction based on the 15 m propagation level.
- Manual configurations of TEMPER to use different dielectric surfaces[4] did not provide striking differences in the output profiles. Nevertheless, this should be examined further.
- Verification of Prelude's transmitter patterns against those provided by Armasuisse showed only small (< 2 dB) variations, explainable by the different versions of the public data used[5].
- The current implementation of PETOOL's interface does not provide stable results at low altitudes, suggesting the use of the 10 m or 15 m data with ITU corrections. TEMPER's results are more stable and the 3 m data appear directly usable.

[4] This feature is supported by TEMPER but not yet by the interfaces with Prelude.

[5] Prelude used the latest OFCOM data available at the time of import, while the data provided by Armasuisse was valid at the time of the experiment. There are only minor differences in the patterns between these.

- The OFCOM site location altitude does not always match the terrain height at the location. Experiments with the UTLI transmitter varied the altitude by up to 40 m (much more than the database discrepancy) and resulted in changes of up to 3 dB in the receiver flux.
- The SRTM terrain altitude describes ground-level and does not capture the height of clutter. An experiment with the UTLI transmitter to modify the terrain height of the hill in Figure 3-36 to account for tree heights[6], provided reductions of about 5 – 10 dB.

Figure 3-37 contains final plots for all three stations, as well as the terrain-corrected UTLI result. Initial observations include:

a) The agreement in the 98.3 MHz data is satisfying, although the large fade at index 4500 is unexplained;

b) The agreement in the UTLI data is not yet satisfying, but several promising areas for further work have been identified; and

c) The disagreement in the 99.2 MHz data, in particular near the beginning of the dataset, is unexplained.

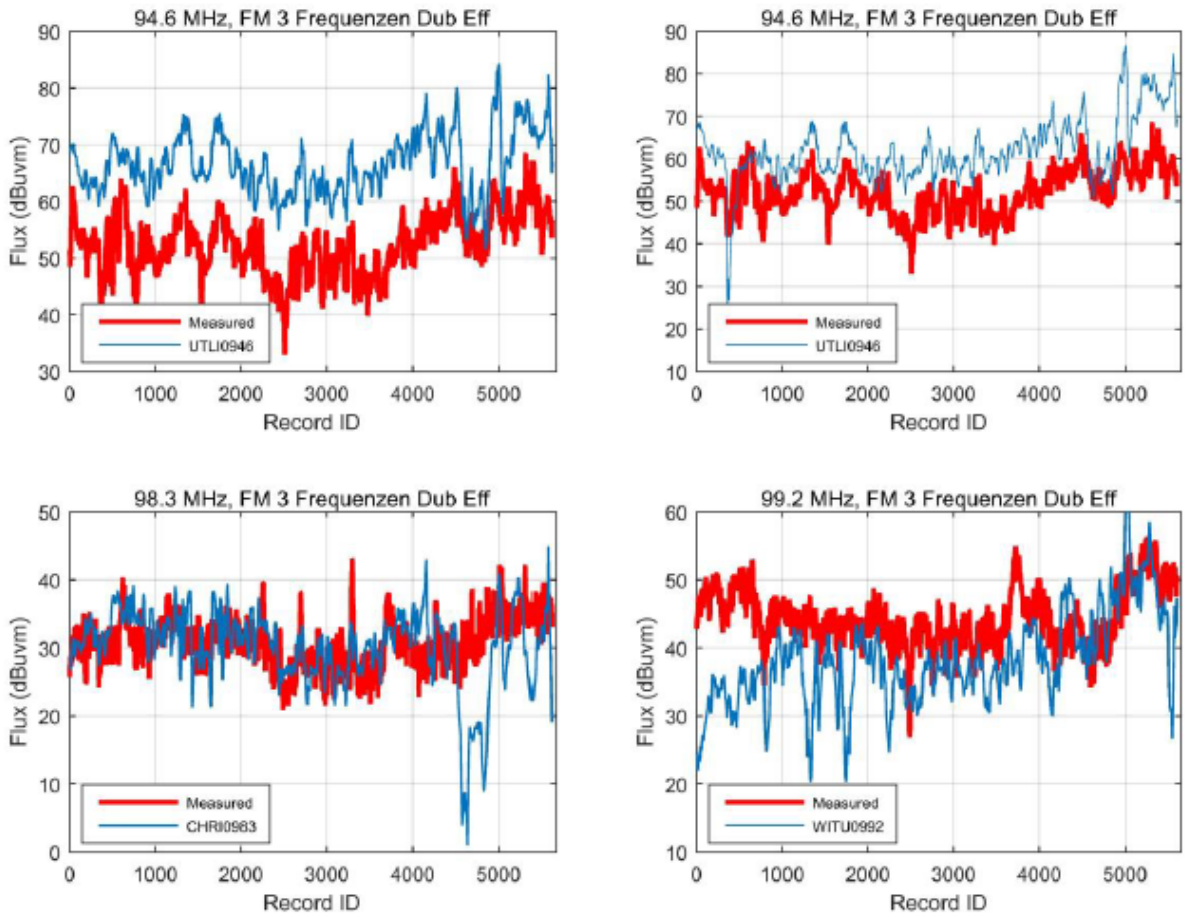

Figure 3-37: Predicted and Measured Flux at Various Points Along the Path for the Three Most-Likely Stations. The top two figures are for UTLI with normal (left) and a +40 m adjusted hill (right), as discussed in the text. The bottom two figures are for CHRI and WITU, and are presented without any adjustments.

[6] Google Earth data suggested that trees are up to 120 feet in this region, and that the SRTM data represent the forest floor.

The analysis process was applied to the Eff-Wal dataset subsequent to the development of the technique on the Dub-Eff dataset. In this way, the first dataset can be viewed as a training set, and the second as an experimental set. Results are contained in Figure 3-38; here, the 98.3 MHz and 99.2 MHz plots each include two stations because of difficulty assigning the received power to a single transmitter. The final dataset (Zrh-Thun) was not considered in this work.

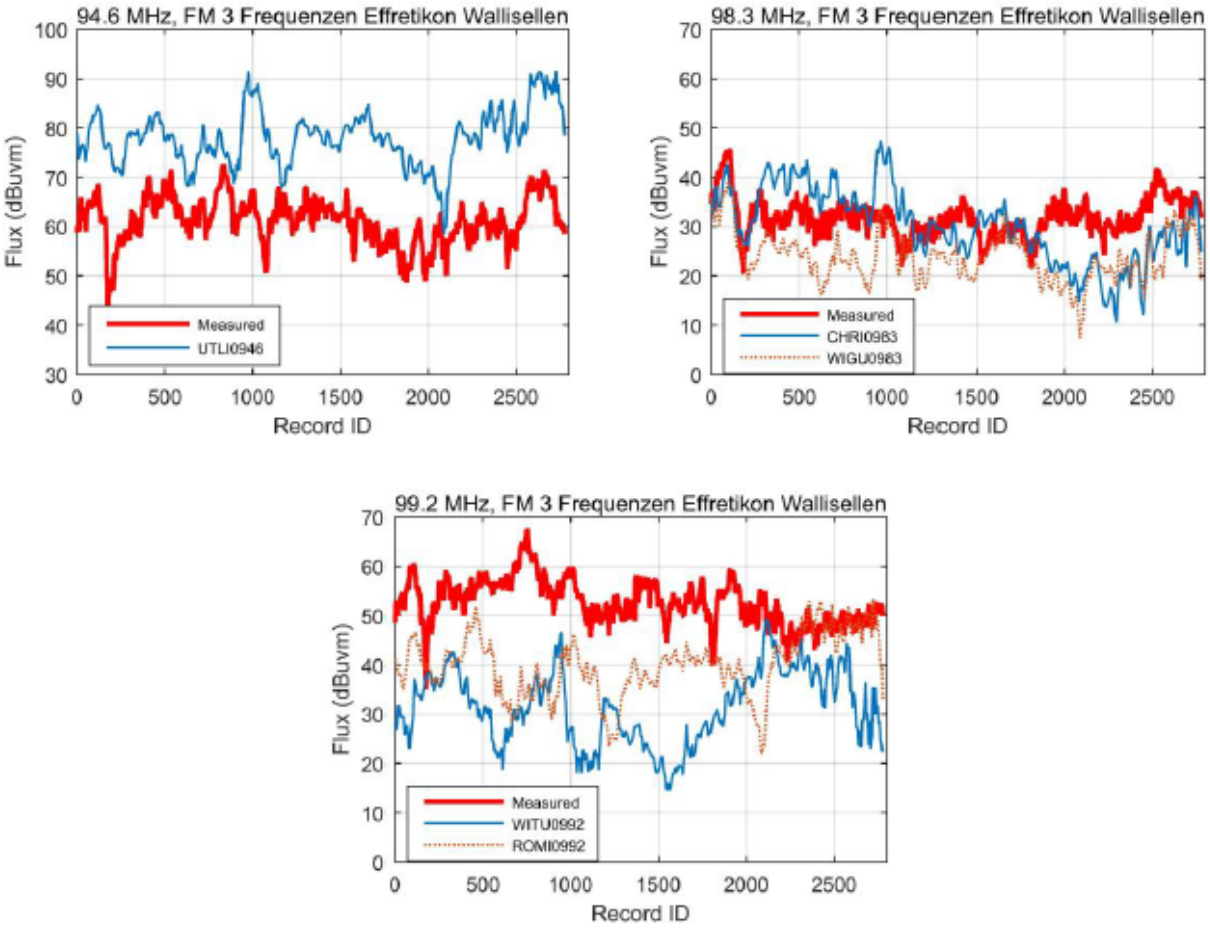

Figure 3-38: Predicted and Measured Flux Profiles for the Second Path of the Dataset, for the Three Different Frequencies. At 98.3 MHz and 99.2 MHz, additional curves (dotted red) have been included for secondary transmitters that present similar powers to the ones expected to be dominant in these data.

Scores for each prediction were obtained by comparing the simulated and measured power curves; results are shown in Table 3-3. Statistics used in the score included:

a) The fraction of data within 6 dB of the measurement;

b) The average error, computed as $\frac{1}{N}\sum(P_{\text{meas}} - P_{\text{sim}})$;

c) The error variation, computed as $[\text{var}(P_{\text{meas}} - P_{\text{sim}})]^{1/2}$; and

d) The correlation coefficient, computed as $\text{corr}(P_{\text{meas}}, P_{\text{sim}})$.

Table 3-3: Table of Errors Between the Predicted and Measured Flux Densities in this Analysis, for Different Configurations.

Dübendorf-Effretikon					
Propagator: ITM at 15 m with -12 dB correction					
Station	Frequency	%< 6 dB	Mean Error	Error Std.Dev.	Correlation Coefficient
UTLI	94.6 MHz	11.5	11.25	4.19	0.63
CHRI	98.3 MHz	53.6	-4.16	8.03	-0.1
WITU	99.2 MHz	26.8	8.08	4.59	0.25
Propagator: PETOOL with PEC at 15 m with -12 dB correction					
Station	Frequency	%< 6 dB	Mean Error	Error Std.Dev.	Correlation Coefficient
UTLI	94.6 MHz	33.9	8.52	5.81	0.46
CHRI	98.3 MHz	80.3	0.46	4.98	0.06
WITU	99.2 MHz	53.4	-5.11	6.05	0.28
Propagator: TEMPER with PEC at 3 m					
Station	Frequency	%< 6 dB	Mean Error	Error Std.Dev.	Correlation Coefficient
UTLI	94.6 MHz	6.4	13.99	4.79	0.60
CHRI	98.3 MHz	78.8	-1.11	6.35	0.19
WITU	99.2 MHz	45.5	-6.71	7.16	0.26
Propagator: TEMPER with Dielectric at 3 m					
Station	Frequency	%< 6 dB	Mean Error	Error Std.Dev.	Correlation Coefficient
UTLI	94.6 MHz	6.2	14.00	4.67	0.61
CHRI	98.3 MHz	79.3	-0.87	6.20	0.19
WITU	99.2 MHz	47.2	-6.37	7.01	0.27
UTLI+40m	94.6 MHz	20.6	9.49	5.89	0.61
UTLI+60m	94.6 MHz	38.7	7.05	7.05	0.55
Effretikon-Wallisellen					
Propagator: TEMPER with TEMPER Dielectric at 3 m					
Station	Frequency	%< 6 dB	Mean Error	Error Std.Dev.	Correlation Coefficient
UTLI	94.6 MHz	4.1	16.77	5.60	0.42
CHRI	98.3 MHz	50.7	-1.73	7.93	0.13
WITU	99.2 MHz	5.4	-21.31	9.40	-0.20
ROMI	99.2 MHz	23.1	-12.86	8.46	-0.24

One source of disagreement between the models and the measured data, not explored in the analysis, is that of polarization mismatch between the broadcast and the measurement. Whereas the experiment used a single vertically-polarized antenna, some sources indicate that at least one transmitter (UTLI) might be horizontally-polarized. No attempt was made to account for the mismatch or depolarization of scattered signals. Future work should examine this problem further and investigate dual-polarized receivers.

In general, these results highlight the difficulty of reproducing ground-level measurements using existing models, and the necessity for further developments in this area. While obvious for GMTI or surface-SAR applications, this need might also be relevant to airborne applications, which could be influenced by low-grazing angles or by clutter illumination for low-speed targets. Future work should also develop techniques for performing similar analyses for airborne targets at various altitudes and for various atmospheric conditions.

3.4 CONCLUSION AND FUTURE DIRECTIONS

The characteristics of tropospheric radio propagation are important to passive radar. Errors in its prediction will ultimately affect the anticipated detection statistics of the radar, which could have consequences on network planning and overall performance. Similarly, variations in the link losses will cause SINR variations, through the influence on the direct path, interferer, echo, and clutter signals. This work has explored methods of both modelling and measuring these effects.

It is recommended that future work should focus on the experimental and model-based analysis of several aspects of tropospheric propagation, including:

- Developing models to predict performance in a non-laterally-homogeneous atmosphere; these models should describe the dynamic and spatially-dependent atmospheric refractivity using realistic atmospheric data;
- Exploring the empirical decorrelation of the power fluctuations in more detail, given the disagreement between spatial correlation in the Springfield and Daytona measurements;
- Obtaining data to support evaluation of the impact of variations to targets at altitude, including both fixed observations as well as the collection of very large datasets of known targets; and
- Creating useful statistical models that describe the anticipated variations and covariances of each radio link in the PR problem, in a manner consistent with the measured results.

Focusing work in these areas will improve capabilities in passive radar performance prediction by enabling both situation-specific and long-term assessments of the radar's performance.

3.5 REFERENCES

[1] R.A. Rowden, L.F. Tagholm, and J.W. Stark, "A survey of tropospheric wave propagation measurements by the B.B.C., 1946-1957," in *Proc. IEE - Part B*, vol. 105, no. 8, pp. 84-90, 1958.

[2] H.V. Hitney, J.H. Richter, R.A. Pappert, K.D. Anderson, and G.B. Baumgartner, Jr., "Tropospheric radio propagation assessment," *Proc. IEEE*, vol. 73, no. 2, pp. 265-283, February 1985.

[3] R. Rudd, "Statistics of anomalous tropospheric propagation at UHF frequencies," in *Proc. 3rd European Conf. on Antennas Propag. (EuCAP)*, pp. 3862-3864, 23-27 March 2009.

[4] A path-specific propagation prediction method for point-to-area terrestrial services in the VHF and UHF bands, ITU Recommendation P.1812.2, 2012.

[5] Method for point-to-area predictions for terrestrial services in the frequency range 30 MHz to 3000 MHz, ITU Recommendation P.1546.4, 2012.

[6] A.G. Longley and P.L. Rice, *Prediction of Tropospheric Radio Transmission Loss Over Irregular Terrain A Computer Method*, ESSA Technical Report ERL 79-ITS 67, Tropospheric Telecommunications Laboratory, Boulder, CO, July 1968.

[7] G. Hufford (Undated), *The ITS Irregular Terrain Model, version 1.2.2, The Algorithm*, National Telecommunications and Information Administration, Institute for Telecommunications Sciences, [Online]. Available: http://flattop.its.bldrdoc.gov/itm.html, retrieved July 2012.

[8] *OET Bulletin No. 69, Longley-Rice Methodology for Evaluating TV Coverage and Interference*, Federal Communications Commission, 6 February 2004.

[9] S.E. Shumate, "Longley-Rice and ITU-P.1546 combined: A new international terrain-specific propagation model," in *Proc. 72nd IEEE Veh. Technol. Conf. (VTC)*, pp. 1-5, 6-9 September 2010.

[10] H.G. Booker, "Elements of radio meteorology: how weather and climate cause unorthodox radar vision beyond the geometrical horizon," in *J. IEE, - Part I: General*, vol. 93, no. 70, pp. 460-462, October 1946.

[11] I.M. Brooks, A.K. Goroch, and D.P. Rogers, "Observations of strong surface radar ducts over the Persian Gulf," *J. Appl. Meteor.*, vol. 38, pp. 1293-1310, 1999.

[12] W.E. Devereux and J. Van Egmond, "Effects of ducting on radar operation in the Persian Gulf," in *Proc. IEEE National Radar Conference*, Dallas, TX, pp. 174-181, 1989.

[13] C. Yardim, P. Gerstoft, and W.S. Hodgkiss, "Sensitivity analysis and performance estimation of refractivity from clutter techniques," *Radio Sci.*, 44, RS1008, 2009.

[14] W.L. Patterson, "Advanced Refractive Effects Prediction System (AREPS)," in *Proc. 2007 IEEE Radar Conf.*, Boston, pp. 891-895, 2007.

[15] G.D. Dockery, et al., "An overview of recent advances for the TEMPER radar propagation model," in *Proc. 2007 IEEE Radar Conf.*, Boston, pp. 896-905, 2007.

[16] O. Ozgun, G. Apaydin, M. Kuzuoglu, and L. Sevgi, "PETOOL: MATLAB-based one-way and two-way split-step parabolic equation tool for radiowave propagation over variable terrain," Computer Physics Communications, vol. 182, no. 12, pp. 2638-2654, December 2011.

[17] C.M. Hoyuela, A.J. Terzuoli, Jr., and R.P. Wasky, "Determining possible receiver locations for passive radar," *IEE Proc. Radar, Sonar and Navig.*, vol. 152, no. 3, pp. 206-214, 3 June 2005.

[18] M. Inggs, G. Lange, and Y. Paichard, "A quantitative method for mono- and multistatic radar coverage area prediction," in *Proc. 2010 IEEE Radar Conf.*, pp. 707-711, 10-14 May 2010.

[19] G.A. Hufford, A.G. Longley, and W.A. Kissick, "A guide to the use of the ITS Irregular Terrain Model in the area prediction mode," NTIA Report 82-100, US Department of Commerce, April 1982.

[20] U.S. Department of Commerce NTIA/ITS, Institute for Telecommunication Sciences, "Irregular Terrain Model (ITM) (Longley-Rice)," Computer source code as *ITMDLL.cpp* [Online]. Available: http://flattop.its.bldrdoc.gov/itm.html, retrieved July 2012.

[21] Y. Song and A. Akoglu, "Parallel implementation of the Irregular Terrain Model (ITM) for radio transmission loss prediction using GPU and Cell BE processors," *IEEE Trans. Parallel Distrib. Syst.*, vol. 22, no. 8, pp. 1276-1283, August 2011.

[22] A.E. Barrios, W.L. Patterson, and R.A. Sprague, "Advanced Propagation Model (APM) Version 2.1.04 Computer Software Configuration Item (CSCI) Documents," Technical Document 3214, Space and Naval Warfare Systems Center, San Diego, CA, February 2007.

[23] E. Brookner, P.R. Cornely, and Y.F. Lok, "AREPS and TEMPER - Getting familiar with these powerful propagation software tools," in Proc. 2007 IEEE Radar Conf., Boston, MA, pp. 1034-1043, 2007.

[24] K. Kulpa, M. Malanowski, and P. Samczynski, "Multipath illumination effects in passive radars," in *Proc. 2011 Intl. Radar Symp. (IRS)*, pp. 321-326, 7-9 September 2011.

[25] J.L. Garry and G.E. Smith, "Distributed multipath effects with passive radar," in *Proc. 2016 IEEE Radar Conf.*, pp. 1-6, 2016.

[26] J.R. Kuttler and G.D. Dockery, "Theoretical description of the parabolic approximation/Fourier split-step method of representing electromagnetic propagation in the troposphere," in *Radio Science*, vol. 26, no. 2, pp. 381-393, March-April 1991.

[27] NOAA National Centers for Environmental Information, *Integrated Global Radiosonde Archive.* Available Online: https://www.ncdc.noaa.gov/data-access/weather-balloon/integrated-global-radiosonde-archive. Retrieved June, 2017.

[28] R.A. Paulus, "VOCAR: an experiment in variability of coastal atmospheric refractivity," in *Proc. International Geoscience and Remote Sensing Symposium, 1994. IGARSS '94*, Pasadena, CA, pp. 386-388, vol. 1, 1994.

[29] D.W. Blood, S. McKinley, C.R. Philbrick, R. Paulus, and T. Rogers, "Lidar measured refractive effects in a coastal environment," in *Proc. 1994 Intl. Geosci. and Remote Sens. Symp. (IGARSS)*, vol. 1, pp. 394-396, 8-12 August 1994.

[30] K.M. Scott, T.R. Dabrowski, W.C. Barott, and B. Himed, "Site planning and illuminator variability for DTV-based passive radar," *in Proc. 2016 IEEE Radar Conference (RadarConf)*, Philadelphia, PA, pp. 1-5, 2016.

[31] F. Colone, D. Pastina, P. Falcone, and P. Lombardo, "WiFi-Based Passive ISAR for High-Resolution Cross-Range Profiling of Moving Targets," *IEEE Transactions on Geoscience and Remote Sensing,* vol. 52, pp. 3486-3501, 2013.

REPORT DOCUMENTATION PAGE

1. Recipient's Reference	2. Originator's References	3. Further Reference	4. Security Classification of Document
	STO-TR-SET-207 AC/323(SET-207)TP/863	ISBN 978-92-837-2187-1	PUBLIC RELEASE

5. Originator

Science and Technology Organization
North Atlantic Treaty Organization
BP 25, F-92201 Neuilly-sur-Seine Cedex, France

6. Title

Advanced Situation-Specific Modeling, Sensing and Vulnerability Mitigation Using Passive Radar Technology

7. Presented at/Sponsored by

Final Report of NATO SET-207.

8. Author(s)/Editor(s)	9. Date
Multiple	March 2019
10. Author's/Editor's Address	**11. Pages**
Multiple	98

12. Distribution Statement

There are no restrictions on the distribution of this document. Information about the availability of this and other STO unclassified publications is given on the back cover.

13. Keywords/Descriptors

Border Surveillance
Data Handling
Foliage Penetration
Knowledge-aided Adaption
Passive Radar
Situational Awareness
Symmetric and Asymmetric Threat Mitigation

14. Abstract

The objective of SET-207 was to extend the valuable lessons learned from SET-164 by developing and validating a robust and inclusive model for passive radar.

In particular, SET-207 undertook three propagation measurement campaigns. One trial was performed in Florida, USA, the second in Switzerland and the third in South Africa. The three trial regions were significantly different in topology and climate and the analysis and associated models contribute greater insight into passive radar performance. The individual studies focus on propagation effects in VHF and UHF as a function of multipath and climatic conditions.

Several conclusions can be drawn from the measurements and models that appear in this report:

- FM based Passive Radar receivers that are positioned close to the ground (elevated less than 10 meters) and reasonably far from the reference transmitter (baseline longer than 20 km) will most likely be within the first multipath null and will suffer from multipath losses.
- The depth of the multipath null depends (amongst other factors) on the electromagnetic properties of the reflecting surface. Changes in conductivity and permittivity due to changing soil conditions can have significant effects on the reflection coefficient.

NORTH ATLANTIC TREATY ORGANIZATION

BP 25
F-92201 NEUILLY-SUR-SEINE CEDEX • FRANCE
Télécopie 0(1)55.61.22.99 • E-mail mailbox@cso.nato.int

SCIENCE AND TECHNOLOGY ORGANIZATION

DIFFUSION DES PUBLICATIONS
STO NON CLASSIFIEES

Les publications de l'AGARD, de la RTO et de la STO peuvent parfois être obtenues auprès des centres nationaux de distribution indiqués ci-dessous. Si vous souhaitez recevoir toutes les publications de la STO, ou simplement celles qui concernent certains Panels, vous pouvez demander d'être inclus soit à titre personnel, soit au nom de votre organisation, sur la liste d'envoi.

Les publications de la STO, de la RTO et de l'AGARD sont également en vente auprès des agences de vente indiquées ci-dessous.

Les demandes de documents STO, RTO ou AGARD doivent comporter la dénomination « STO », « RTO » ou « AGARD » selon le cas, suivi du numéro de série. Des informations analogues, telles que le titre est la date de publication sont souhaitables.

Si vous souhaitez recevoir une notification électronique de la disponibilité des rapports de la STO au fur et à mesure de leur publication, vous pouvez consulter notre site Web (http://www.sto.nato.int/) et vous abonner à ce service.

CENTRES DE DIFFUSION NATIONAUX

ALLEMAGNE
Streitkräfteamt / Abteilung III
Fachinformationszentrum der Bundeswehr (FIZBw)
Gorch-Fock-Straße 7, D-53229 Bonn

BELGIQUE
Royal High Institute for Defence – KHID/IRSD/RHID
Management of Scientific & Technological Research
for Defence, National STO Coordinator
Royal Military Academy – Campus Renaissance
Renaissancelaan 30, 1000 Bruxelles

BULGARIE
Ministry of Defence
Defence Institute "Prof. Tsvetan Lazarov"
"Tsvetan Lazarov" bul no.2
1592 Sofia

CANADA
DGSIST 2
Recherche et développement pour la défense Canada
60 Moodie Drive (7N-1-F20)
Ottawa, Ontario K1A 0K2

DANEMARK
Danish Acquisition and Logistics Organization
(DALO)
Lautrupbjerg 1-5
2750 Ballerup

ESPAGNE
Área de Cooperación Internacional en I+D
SDGPLATIN (DGAM)
C/ Arturo Soria 289
28033 Madrid

ESTONIE
Estonian National Defence College
Centre for Applied Research
Riia str 12
Tartu 51013

ETATS-UNIS
Defense Technical Information Center
8725 John J. Kingman Road
Fort Belvoir, VA 22060-6218

FRANCE
O.N.E.R.A. (ISP)
29, Avenue de la Division Leclerc
BP 72
92322 Châtillon Cedex

GRECE (Correspondant)
Defence Industry & Research General
Directorate, Research Directorate
Fakinos Base Camp, S.T.G. 1020
Holargos, Athens

HONGRIE
Hungarian Ministry of Defence
Development and Logistics Agency
P.O.B. 25
H-1885 Budapest

ITALIE
Ten Col Renato NARO
Capo servizio Gestione della Conoscenza
F. Baracca Military Airport "Comparto A"
Via di Centocelle, 301
00175, Rome

LUXEMBOURG
Voir Belgique

NORVEGE
Norwegian Defence Research
Establishment
Attn: Biblioteket
P.O. Box 25
NO-2007 Kjeller

PAYS-BAS
Royal Netherlands Military
Academy Library
P.O. Box 90.002
4800 PA Breda

POLOGNE
Centralna Biblioteka Wojskowa
ul. Ostrobramska 109
04-041 Warszawa

PORTUGAL
Estado Maior da Força Aérea
SDFA – Centro de Documentação
Alfragide
P-2720 Amadora

REPUBLIQUE TCHEQUE
Vojenský technický ústav s.p.
CZ Distribution Information Centre
Mladoboleslavská 944
PO Box 18
197 06 Praha 9

ROUMANIE
Romanian National Distribution
Centre
Armaments Department
9-11, Drumul Taberei Street
Sector 6
061353 Bucharest

ROYAUME-UNI
Dstl Records Centre
Rm G02, ISAT F, Building 5
Dstl Porton Down
Salisbury SP4 0JQ

SLOVAQUIE
Akadémia ozbrojených síl gen.
M.R. Štefánika, Distribučné a
informačné stredisko STO
Demänová 393
031 06 Liptovský Mikuláš 6

SLOVENIE
Ministry of Defence
Central Registry for EU & NATO
Vojkova 55
1000 Ljubljana

TURQUIE
Milli Savunma Bakanlığı (MSB)
ARGE ve Teknoloji Dairesi
Başkanlığı
06650 Bakanliklar – Ankara

AGENCES DE VENTE

The British Library Document
Supply Centre
Boston Spa, Wetherby
West Yorkshire LS23 7BQ
ROYAUME-UNI

Canada Institute for Scientific and
Technical Information (CISTI)
National Research Council Acquisitions
Montreal Road, Building M-55
Ottawa, Ontario K1A 0S2
CANADA

Les demandes de documents STO, RTO ou AGARD doivent comporter la dénomination « STO », « RTO » ou « AGARD » selon le cas, suivie du numéro de série (par exemple AGARD-AG-315). Des informations analogues, telles que le titre et la date de publication sont souhaitables. Des références bibliographiques complètes ainsi que des résumés des publications STO, RTO et AGARD figurent dans le « NTIS Publications Database » (http://www.ntis.gov).

NORTH ATLANTIC TREATY ORGANIZATION

BP 25
F-92201 NEUILLY-SUR-SEINE CEDEX • FRANCE
Télécopie 0(1)55.61.22.99 • E-mail mailbox@cso.nato.int

SCIENCE AND TECHNOLOGY ORGANIZATION

DISTRIBUTION OF UNCLASSIFIED STO PUBLICATIONS

AGARD, RTO & STO publications are sometimes available from the National Distribution Centres listed below. If you wish to receive all STO reports, or just those relating to one or more specific STO Panels, they may be willing to include you (or your Organisation) in their distribution.

STO, RTO and AGARD reports may also be purchased from the Sales Agencies listed below.

Requests for STO, RTO or AGARD documents should include the word 'STO', 'RTO' or 'AGARD', as appropriate, followed by the serial number. Collateral information such as title and publication date is desirable.

If you wish to receive electronic notification of STO reports as they are published, please visit our website (http://www.sto.nato.int/) from where you can register for this service.

NATIONAL DISTRIBUTION CENTRES

BELGIUM
Royal High Institute for Defence – KHID/IRSD/RHID
Management of Scientific & Technological Research for Defence, National STO Coordinator
Royal Military Academy – Campus Renaissance
Renaissancelaan 30
1000 Brussels

BULGARIA
Ministry of Defence
Defence Institute "Prof. Tsvetan Lazarov"
"Tsvetan Lazarov" bul no.2
1592 Sofia

CANADA
DSTKIM 2
Defence Research and Development Canada
60 Moodie Drive (7N-1-F20)
Ottawa, Ontario K1A 0K2

CZECH REPUBLIC
Vojenský technický ústav s.p.
CZ Distribution Information Centre
Mladoboleslavská 944
PO Box 18
197 06 Praha 9

DENMARK
Danish Acquisition and Logistics Organization (DALO)
Lautrupbjerg 1-5
2750 Ballerup

ESTONIA
Estonian National Defence College
Centre for Applied Research
Riia str 12
Tartu 51013

FRANCE
O.N.E.R.A. (ISP)
29, Avenue de la Division Leclerc – BP 72
92322 Châtillon Cedex

GERMANY
Streitkräfteamt / Abteilung III
Fachinformationszentrum der Bundeswehr (FIZBw)
Gorch-Fock-Straße 7
D-53229 Bonn

GREECE (Point of Contact)
Defence Industry & Research General Directorate, Research Directorate
Fakinos Base Camp, S.T.G. 1020
Holargos, Athens

HUNGARY
Hungarian Ministry of Defence
Development and Logistics Agency
P.O.B. 25
H-1885 Budapest

ITALY
Ten Col Renato NARO
Capo servizio Gestione della Conoscenza
F. Baracca Military Airport "Comparto A"
Via di Centocelle, 301
00175, Rome

LUXEMBOURG
See Belgium

NETHERLANDS
Royal Netherlands Military Academy Library
P.O. Box 90.002
4800 PA Breda

NORWAY
Norwegian Defence Research Establishment, Attn: Biblioteket
P.O. Box 25
NO-2007 Kjeller

POLAND
Centralna Biblioteka Wojskowa
ul. Ostrobramska 109
04-041 Warszawa

PORTUGAL
Estado Maior da Força Aérea
SDFA – Centro de Documentação
Alfragide
P-2720 Amadora

ROMANIA
Romanian National Distribution Centre
Armaments Department
9-11, Drumul Taberei Street
Sector 6
061353 Bucharest

SLOVAKIA
Akadémia ozbrojených síl gen M.R. Štefánika, Distribučné a informačné stredisko STO
Demänová 393
031 06 Liptovský Mikuláš 6

SLOVENIA
Ministry of Defence
Central Registry for EU & NATO
Vojkova 55
1000 Ljubljana

SPAIN
Área de Cooperación Internacional en I+D
SDGPLATIN (DGAM)
C/ Arturo Soria 289
28033 Madrid

TURKEY
Milli Savunma Bakanlığı (MSB)
ARGE ve Teknoloji Dairesi Başkanlığı
06650 Bakanliklar – Ankara

UNITED KINGDOM
Dstl Records Centre
Rm G02, ISAT F, Building 5
Dstl Porton Down, Salisbury SP4 0JQ

UNITED STATES
Defense Technical Information Center
8725 John J. Kingman Road
Fort Belvoir, VA 22060-6218

SALES AGENCIES

The British Library Document Supply Centre
Boston Spa, Wetherby
West Yorkshire LS23 7BQ
UNITED KINGDOM

Canada Institute for Scientific and Technical Information (CISTI)
National Research Council Acquisitions
Montreal Road, Building M-55
Ottawa, Ontario K1A 0S2
CANADA

Requests for STO, RTO or AGARD documents should include the word 'STO', 'RTO' or 'AGARD', as appropriate, followed by the serial number (for example AGARD-AG-315). Collateral information such as title and publication date is desirable. Full bibliographical references and abstracts of STO, RTO and AGARD publications are given in "NTIS Publications Database" (http://www.ntis.gov).

ISBN 978-92-837-2187-1